

MEASUREMENT OF SINGLE-TOP T-CHANNEL PRODUCTION USING ATLAS  
DATA

By

Jenny Lyn Holzbauer

A DISSERTATION

Submitted to  
Michigan State University  
in partial fulfillment of the requirements  
for the degree of

DOCTOR OF PHILOSOPHY

Physics

2012

## ABSTRACT

# MEASUREMENT OF SINGLE-TOP T-CHANNEL PRODUCTION USING ATLAS DATA

By

Jenny Lyn Holzbauer

This document reports the measurement of the single-top t-channel cross-section using data from the ATLAS detector, located at the Large Hadron Collider on the border of France and Switzerland. The data used were collected during the first half of 2011, from proton-proton collisions with a 7 TeV center-of-mass collision energy. Single-top is electroweak top-quark production and t-channel is one of the standard model production modes. To isolate this production, selections are applied to find events with a similar final state. A cut-based analysis is used to further isolate the signal using a series of selections in several orthogonal kinematic regions. Finally, a statistical analysis is performed to determine the measured cross-section and the CKM matrix element  $|V_{tb}|$ . The cross-section for top and anti-top production is considered separately and the resulting cross-sections are  $\sigma_{t+} = 59^{+18}_{-16}$  pb for the plus charge channel and  $\sigma_{t-} = 33^{+13}_{-12}$  pb for the minus charge channel. The total measured single-top t-channel cross-section using all kinematic channels in this analysis is  $92^{+29}_{-26}$  pb with an expected cross-section of  $\sigma_t = 65^{+22}_{-20}$  pb.

Copyright by  
JENNY LYN HOLZBAUER  
2012

## TABLE OF CONTENTS

<b>1</b>	<b>Introduction</b>	<b>1</b>
<b>2</b>	<b>Single-top Production and the Standard Model</b>	<b>3</b>
2.1	The Standard Model Particles . . . . .	4
2.1.1	Leptons . . . . .	4
2.1.2	Quarks . . . . .	6
2.1.3	Force Carriers . . . . .	7
2.2	Particle Properties and $ V_{tb} $ . . . . .	7
2.3	Overview of Physics Processes . . . . .	10
2.3.1	Single-top and Other Processes . . . . .	11
2.3.2	Cross-section . . . . .	14
2.4	New Physics Possibilities . . . . .	18
<b>3</b>	<b>ATLAS and the LHC</b>	<b>20</b>
3.1	The Large Hadron Collider, a Short Overview . . . . .	20
3.2	The ATLAS Detector . . . . .	24
3.2.1	Detector Variables and Geometry . . . . .	25
3.2.2	The Inner Detector . . . . .	27
3.2.3	The EM Calorimeter . . . . .	28
3.2.4	The Hadronic and Forward Calorimeters . . . . .	29
3.2.5	The Muon Spectrometer . . . . .	30
3.2.6	Magnets . . . . .	32
3.2.7	The Trigger and Data Collection . . . . .	33
3.2.8	Data Quality . . . . .	34
<b>4</b>	<b>Particle Reconstruction</b>	<b>36</b>
4.1	Electrons . . . . .	37
4.2	Muons . . . . .	39
4.3	Quarks . . . . .	40
4.3.1	b-tagging . . . . .	42
4.3.1.1	How b-quarks are Identified . . . . .	42
4.3.1.2	Impact of Different Operation Points on the Analysis . . . . .	46
4.4	Taus . . . . .	46
4.5	Neutrinos and Missing Energy . . . . .	48

<b>5 Monte Carlo Simulation and Corrections</b>	<b>51</b>
5.1 MC Generator and Showering . . . . .	52
5.2 Monte Carlo Weighting and Corrections . . . . .	53
5.2.1 Theoretical cross-section and luminosity weight . . . . .	53
5.2.2 Pile-up weight . . . . .	54
5.2.3 Lepton scale factor . . . . .	55
5.2.4 Mis-tagging and b-tagging scale factor . . . . .	55
5.2.5 Energy corrections in the analysis . . . . .	55
<b>6 Preselection</b>	<b>58</b>
<b>7 Modeling the Signal and the Backgrounds</b>	<b>62</b>
7.1 Multijet Estimation . . . . .	62
7.2 W+jets Estimation . . . . .	64
<b>8 Event Yields and Discriminating Variables</b>	<b>69</b>
8.1 Event Yields . . . . .	69
8.2 Discriminating Variables . . . . .	70
<b>9 The Cut-Based Analysis</b>	<b>76</b>
9.1 Analysis Channels . . . . .	76
9.2 Analysis Method . . . . .	77
9.2.1 Selection Optimization . . . . .	77
9.2.2 B-tagging Threshold and Cut-Based Selections . . . . .	80
9.3 Selection Choices . . . . .	81
<b>10 The Measurements</b>	<b>88</b>
10.1 Systematic Uncertainties . . . . .	88
10.1.1 Effect of Pileup . . . . .	95
10.2 Results . . . . .	95
10.2.1 Cross-section Calculation and Measurements . . . . .	100
10.2.1.1 Two and Three jet Single Top Quark t-channel Production .	103
10.2.1.2 Positively and Negatively Charged Single Top Quark t-channel Production .	103
10.2.1.3 Combined t-channel Production Cross-section Result . . . . .	104
10.2.2 Estimate of $ V_L $ . . . . .	107
10.2.3 Comment on Significance . . . . .	108
<b>11 Conclusions and Implications for Future Work</b>	<b>111</b>
<b>Bibliography</b> . . . . .	<b>115</b>

<b>Appendices</b>	<b>123</b>
<b>A Data Based Cross-check of <math>t\bar{t}</math> Background</b>	<b>123</b>
<b>B Multivariate Analysis</b>	<b>129</b>
B.1 Boosted Decision Tree Overview . . . . .	129
B.1.1 Classifier Formation and Parameter Optimization . . . . .	131
B.1.2 Cut-based Analysis Variables . . . . .	134
B.1.3 Additional Variables . . . . .	137
<b>C Alternative Analysis Channels</b>	<b>151</b>

# <sup>1</sup> Chapter 1

## <sup>2</sup> Introduction

<sup>3</sup> A rock smashes against another rock and shatters into pieces. Some are shiny, some are  
<sup>4</sup> differently colored. However, if you were to take one of these rock pieces and zoom in, divide  
<sup>5</sup> it into pieces until you can't divide further, you would see that it is composed of the same  
<sup>6</sup> bits of matter as any other rock. In such ways, people have searched for the fundamental  
<sup>7</sup> building blocks of matter, the elementary particles.

<sup>8</sup> In the modern era, we have found these blocks are very small indeed and require a lot  
<sup>9</sup> of human ingenuity to study. It has taken the work of many men and women over the  
<sup>10</sup> years to reach the point where we can do the experiments we now perform. We have found  
<sup>11</sup> that colliding very small bits of matter composed of smaller particles (protons) at very high  
<sup>12</sup> speeds causes the creation of a flurry of new, fundamental particles. These particles may  
<sup>13</sup> have unintuitive properties, such as masses larger than the two protons originally collided  
<sup>14</sup> (made possible by the large amount of energy used to collide them). In this dissertation we

<sub>15</sub> will study one such fundamental particle.

<sub>16</sub> Thousands of scientists are now working at the Large Hadron Collider (LHC) on four  
<sub>17</sub> experiments located at different points around the collider ring. Two are general purpose  
<sub>18</sub> machines, ATLAS and CMS. These machines are designed to try to find not only particles  
<sub>19</sub> and processes we know exist but also new ones. These machines smash bits of atoms that  
<sub>20</sub> are already quite small (protons) together at incredibly high speeds, producing new particles  
<sub>21</sub> which decay or smash into others and eventually some particles hit the detectors. Scien-  
<sub>22</sub> tists use large computing clusters to take this information and attempt to reconstruct what  
<sub>23</sub> happened when the original bits collided, and to sort out the collisions with particles and  
<sub>24</sub> processes they don't want from the ones they do.

<sub>25</sub> Clearly this is a challenging thing, cutting-edge work only possible in the modern era.  
<sub>26</sub> But the questions we look to answer are fundamental. What is the world really made of  
<sub>27</sub> at the smallest level? What are the properties of those things? How do they interact with  
<sub>28</sub> other things at this scale and what do those interactions produce?

<sub>29</sub> In this dissertation, we will discuss specifically the search for the t-channel single-top  
<sub>30</sub> quark production. The top quark is the most massive small particle yet observed and the  
<sub>31</sub> t-channel production mode refers to a particular way it is created. We will overview the  
<sub>32</sub> particles known to exist and the current theory related to these. Then we will examine  
<sub>33</sub> the collider and detector used in this study (the ATLAS detector). Finally we will discuss  
<sub>34</sub> the procedure to isolate this process from so many others, as well as the measurement and  
<sub>35</sub> kinematics of this process.

<sup>36</sup> **Chapter 2**

<sup>37</sup> **Single-top Production and the**

<sup>38</sup> **Standard Model**

<sup>39</sup> High energy physics deals with the very fundamental parts of our universe, the fundamental particles and forces. Our present understanding is that there are four forces: gravity, electromagnetism, strong and weak. As energies increase, it is predicted that these forces can be united into one force, starting with the electromagnetic and weak forces, which form the electroweak force. Each force has a mediating particle, a force carrier, which governs interactions of various particles. These particles are discussed in the next section.

<sup>45</sup> Single-top production is the process where a top quark is created in an electroweak interaction. As stated previously, the top quark is the most massive of the elementary particles. Only one top quark is produced in an electroweak interaction. There is another version of top quark production using the strong force and involving a top and anti-top ( $t\bar{t}$ ). This was the process detected in 1995 to claim discovery [1, 2], meaning a likelihood of less than 0.0000006 of background events imitating the signal. Single-top itself was only recently

51 discovered [3, 4, 5] and the particular channel (t-channel) discussed in this document was  
52 separately observed in 2011 [6] by the D0 collaboration at the Tevatron. Shortly afterwards,  
53 measurements of t-channel single-top production were reported by the CMS experiment [7]  
54 and the ATLAS experiment [8, 9] at the LHC (see the next chapter for more details on the  
55 LHC and ATLAS).

56 This single-top t-channel process is still very new and, as such, has not been fully studied.  
57 It is possible that deviations could be found in its various fundamental properties, which  
58 could indicate new particles or anomalous parts of the standard model. In this document, we  
59 will measure the cross-section of this process and consider its kinematics. But first, before  
60 performing a new measurement, we must understand what is already known.

## 61 **2.1 The Standard Model Particles**

62 The standard model is the basic theory of particle physics [10, 11, 12, 13] and was formulated  
63 in the 1960's and 1970's. It describes and predicts various particles and their properties based  
64 on symmetry relations. The model divides the fundamental particles into several categories  
65 and subcategories, pictured in Figure 2.1. There are three major particle categories: leptons,  
66 quarks and bosons (force carriers). There are also three generations of the quarks and leptons,  
67 where each generation is designated by a different shade in the figure.

### 68 **2.1.1 Leptons**

69 One category of particles are the leptons. Leptons typically include electrons, muons, taus,  
70 and their corresponding neutrinos. However, we will use this term in this document to  
71 generally refer to electrons, muons and/or taus, while neutrinos are considered as a separate

# *Particles*

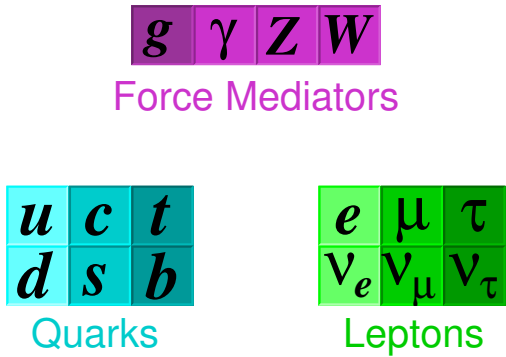


Figure 2.1: The known standard model particles. Different generations of quarks and leptons are indicated by different shades.

72 set of particles. The electron is a stable lepton. The leptons do not interact via the strong  
73 force and so are not involved in hadronic bound states like the proton. Electrons are involved  
74 in the structure of the atom. Muons and taus are heavier than the electron and decay to  
75 other particles. This is particularly true for the tau. Unlike the tau, the muon survives long  
76 enough to escape our detector which is important for particle identification, but has a short  
77 decay time relative to the electron. For each lepton there is a corresponding anti-lepton with  
78 opposite charge.

79 There is also a corresponding neutrino flavor for each lepton flavor, or type (electron  
80 neutrino, muon neutrino, and tau neutrino). Each lepton and its corresponding neutrino form  
81 a set of particles where each lepton type is considered a separate generation (there are three  
82 generations). Neutrinos are the lightest of the known particles and have no charge. There are  
83 no known right handed neutrinos or left handed anti-neutrinos, where right handed indicates  
84 spin and momenta are in the same direction and left handed indicates the opposite. This

85 difference, rather than a difference in charge, distinguishes the neutrino and anti-neutrino.

86 Because neutrinos are nearly massless and neutral, they are very difficult to detect. Neu-  
87 trinos usually pass right through detectors without interacting. This makes neutrino astro-  
88 physics possible, because neutrinos from distant sources will travel from the source without  
89 interacting and scattering off clouds of matter between the source and Earth. However, this  
90 is problematic for collider physics. Particles from collisions need to interact with matter and  
91 deposit their energy into the detector to be detected. While this may not always happen, it  
92 should happen nearly 100% of the time to prevent uncertainties on the measurements from  
93 getting large. To handle neutrinos, we don't build a dedicated neutrino detector but instead  
94 make use of event kinematics to account for the neutrino via missing energy in the event.  
95 This will be discussed further in Section 4.5.

### 96 2.1.2 Quarks

97 Quarks are arranged like the leptons into generations, as seen in Figure 2.1. They are  
98 different from the leptons because they can interact via the strong force and form bound  
99 states, like the proton. There are three generations and each contains two particles, making  
100 six different flavors in total (u, d, s, c, t, b). The first generation contains lighter quarks,  
101 up (u) and down (d), the only stable quarks. The second generation contains strange (s)  
102 and charm (c) quarks, and the third contains the heaviest quarks, bottom (b) and top (t),  
103 which are sometimes also called beauty and truth. The first three (u, d, s) are typically  
104 called light quarks, and the charm quark is sometimes included in this category as well,  
105 but for the purposes of this document will either be considered separately or considered  
106 to be a heavy quark. The bottom quark is considered heavy, but the top quark though

<sup>107</sup> is by far the heaviest and this is a distinguishing characteristic of this quark. It is also  
<sup>108</sup> special because it will decay to other particles before it hadronizes (unlike the other quarks)  
<sup>109</sup> preserving “bare quark” information in its decay products. This is because its decay time is  
<sup>110</sup>  $0.5 \times 10^{-24} \text{ s}$  [11], which is shorter than the hadronization time scale. This scale,  $\Lambda_{QCD}^{-1}$ ,  
<sup>111</sup> corresponds roughly to  $10^{-23} \text{ s}$  [14]. Other quarks survive longer than this scale and will  
<sup>112</sup> hadronize instead of decay, which means they produce a bound state of mesons or baryons.  
<sup>113</sup> Mesons are combinations of quarks and anti-quarks, while baryons are combinations of three  
<sup>114</sup> quarks.

### <sup>115</sup> **2.1.3 Force Carriers**

<sup>116</sup> The other major particle category contains the force carriers, or gauge bosons. One of these is  
<sup>117</sup> the gluon ( $g$ ), particularly involved in strong interactions and can also self-interact. Photons  
<sup>118</sup> ( $\gamma$ ) are the force carriers of the electromagnetic interaction, but are not usually involved  
<sup>119</sup> in the single-top interactions. The other mediators are bosons associated with electroweak  
<sup>120</sup> interactions, the Z and W. Both are relatively heavy (80 to 90 GeV) compared to the other  
<sup>121</sup> particles at this scale, and are about half as heavy as the top quark. Additionally, it has been  
<sup>122</sup> postulated that there is a Higgs boson and a Higgs field which gives mass to the particles in  
<sup>123</sup> the standard model. However, at the time of publication this has not been observed, so we  
<sup>124</sup> will not go into detail about it here.

## <sup>125</sup> **2.2 Particle Properties and $|V_{tb}|$**

<sup>126</sup> The standard model particles have very different characteristics, including a variety of charges  
<sup>127</sup> and masses. Anti-particles are designated with a bar over the top of their symbol and have

128 the negative of the normal particle's charge. A particle's charge is given as a fraction of the  
 129 elementary charge,  $e = 1.6 \times 10^{-19}$  Coulomb. The down, strange and bottom quark all have  
 130 -1/3 charge while the up, charm and top quarks have +2/3 charge. The electrons, muons,  
 131 and taus have -1 charge while the neutrinos, photon, and Z boson have 0 charge. The W  
 132 boson has  $\pm 1$  charge. Additionally, particles also have a flavor, as discussed previously, and  
 133 quarks have a color charge. The color charge is much like the electric charge but related to  
 134 the strong interaction (hence its relation to quarks). The allowed meson and baryon bound  
 135 states are determined by the color charge.

136 The particle masses vary over several orders of magnitude. The range of quark and lepton  
 137 masses (neutrinos are not pictured), are displayed in Figure 2.2. Notice that there are three  
 138 quarks with masses of 1 GeV or larger, the c, b, and t quarks. The mass of the top quark is  
 139 of particular interest in this document and we use the value 172.5 GeV, which is consistent  
 140 with the current Particle Data Group value [11].

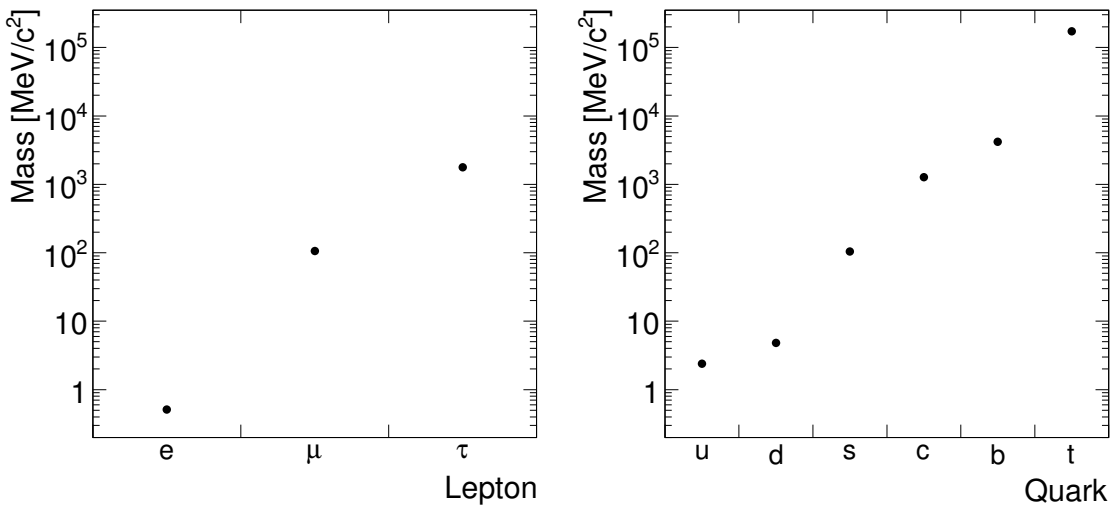


Figure 2.2: The standard model leptons (left) and quarks (right), by mass.

141 The gluon and W boson have the special properties that they can effectively change the

<sup>142</sup> color and flavor of a quark, respectively. A gluon for instance may form a vertex with top  
<sup>143</sup> and anti-top but not two tops. Gluons are special as well because they may self-interact and  
<sup>144</sup> form more gluons. The t-channel single-top process involves the W boson and thus flavor  
<sup>145</sup> exchange. For example, a vertex involving a  $W^+$  may include a top and anti-bottom quark,  
<sup>146</sup> but not two top quarks. The probability that a W vertex could involve a top and a down  
<sup>147</sup> or strange quark is nearly zero according to the standard model, while the probability of  
<sup>148</sup> top and bottom is nearly one. This is displayed in the Cabibbo-Kobayashi-Maskawa (CKM)  
<sup>149</sup> matrix [15, 16], which is nearly, but not quite, a unit matrix.

<sup>150</sup> The CKM matrix describes how likely it is for a quark to change to a quark of another  
<sup>151</sup> flavor. Specifically, the probability is the relevant matrix entry squared. These are tradition-  
<sup>152</sup> ally called  $V_{qq'}$ , where q is a quark and q' is the quark in another flavor. More information  
<sup>153</sup> about the values may be found in the PDG [11]. The matrix element we will be particularly  
<sup>154</sup> interested in,  $V_{tb}$ , may be indirectly measured with  $t\bar{t}$  production, but directly observed with  
<sup>155</sup> single-top production. The standard model value is 1.

<sup>156</sup> The single-top cross-section, related to the number of single-top events produced in the  
<sup>157</sup> collider, is derived from the square of the matrix element, M. The matrix element varies as  
<sup>158</sup> follows in the standard model, where  $P_L$  is  $1/2(1 - \gamma^5)$ :

$$M \propto \bar{b}\gamma^\mu V_{tb} P_L t \quad (2.1)$$

<sup>159</sup> Thus, the cross-section is proportional to  $|V_{tb}|^2$  in the standard model. If we allow anomalous  
<sup>160</sup> couplings in this term above some new physics scale, the term  $V_{tb}$  may be rewritten as  $V_L$ ,  
<sup>161</sup> where  $V_L$  is just  $V_{tb}$  plus a factor that depends on the new physics scale.

<sup>162</sup> The Lagrangian, allowing anomalous coupling terms, may be written as follows [17, 18].

<sub>163</sub> Here  $P_R$  is  $1/2(1 + \gamma^5)$ ,  $M_W$  is the W boson mass, the  $\gamma$  and  $\sigma$  terms are constant (Dirac  
<sub>164</sub> or Pauli) matrices,  $g$  is a coupling constant,  $q_\nu$  is the W boson momentum four-vector, and  
<sub>165</sub>  $\bar{b}$ ,  $t$ , and  $W_\mu^-$  are field terms for the bottom quark, top quark, and W boson respectively:

$$L_{Wtb} = \frac{g}{\sqrt{2}} \bar{b} \gamma^\mu (V_L P_L + V_R P_R) t W_\mu^- - \frac{g}{\sqrt{2}} \bar{b} \frac{i \sigma^{\mu\nu} q_\nu}{M_W} (g_L P_L + g_R P_R) t W_\mu^- + \dots \quad (2.2)$$

<sub>166</sub> We will assume the anomalous couplings  $V_R$ ,  $g_L$  and  $g_R$  are 0 in this document and will  
<sub>167</sub> measure the value  $|V_L|$  to see if it deviates from the standard model expectation.

<sub>168</sub> Because the matrix element squared is proportional to the cross-section, by using both  
<sub>169</sub> expected and observed cross-section and  $|V_L|$  values, one may write:

$$|V_{L,obs}|^2 = \frac{\sigma_{t,obs}}{\sigma_{t,sm}} |V_{L,sm}|^2 \quad (2.3)$$

<sub>170</sub> where  $\sigma$  is the cross-section, obs refers to the observed value and sm refers to the standard  
<sub>171</sub> model. In this way, one may directly find the  $|V_L|$  value from a single-top observation. The  
<sub>172</sub> standard model expectation for  $V_{L,sm} = V_{tb}$  is 1, so a value greater than 1 for  $|V_L|$  would  
<sub>173</sub> indicate non-standard model couplings.

## <sub>174</sub> 2.3 Overview of Physics Processes

<sub>175</sub> Unfortunately, the LHC collisions do not just produce single-top events, nor are single-top  
<sub>176</sub> events extremely distinct or more common than the many other processes that are produced.  
<sub>177</sub> In this section we overview the single-top processes, other physics processes, and some of the  
<sub>178</sub> characteristics that will be considered in order to distinguish them.

<sup>179</sup> **2.3.1 Single-top and Other Processes**

<sup>180</sup> Feynman diagrams are a common way to visualize particle physics interactions and also  
<sup>181</sup> the equations that describe them. In these diagrams, time flows from left to right. The  
<sup>182</sup> leftmost particles are the initial particles (initial state) and the rightmost particles are the  
<sup>183</sup> final particles (final state). Figure 2.3 shows the Feynman diagrams for single-top processes.  
<sup>184</sup> There are three different production modes: *t*-channel,  $Wt$ , and *s*-channel.  $Wt$  is also  
<sup>185</sup> known as associated production and  $Wt$ -channel. The *t*-channel production is a scattering  
<sup>186</sup> interaction while the *s*-channel production is an annihilation interaction. These are standard  
<sup>187</sup> high energy physics terms. In this dissertation, the signal channel is the *t*-channel mode and  
<sup>188</sup> the other two are considered to be backgrounds.

<sup>189</sup> Notice in each case there is exactly one top quark, the characteristic of single-top produc-  
<sup>190</sup> tion. The top quark comes from an interaction mediated by a W boson except in the case  
<sup>191</sup> of  $Wt$  production, where it is produced along with a W boson. The *t*-channel in particular  
<sup>192</sup> has two quarks in the initial state, a b-quark (or a gluon producing a b-quark, as is shown)  
<sup>193</sup> and generic q-quark. This q-quark is usually a valence quark, while the b-quark may come  
<sup>194</sup> from the sea of quarks in the proton or from a gluon. The final state involves the lone top  
<sup>195</sup> quark and another generic quark in the opposite flavor of the initial q-quark, which is often  
<sup>196</sup> energetic and forward (close to the beam line). It is also possible to have an extra jet in the  
<sup>197</sup> final state from a gluon in the initial state. Incidentally, in the previous section we noticed  
<sup>198</sup> the mass of the W boson is smaller than the top quark, but it is still possible for a W to  
<sup>199</sup> produce a top quark if it is a virtual W, in the *s*-channel diagram for example.

<sup>200</sup> Although it is not shown in these diagrams, the top quark decays to a W and b-quark.  
<sup>201</sup> The W further decays to either a lepton and neutrino or two quarks. For this analysis, we

202 will focus on the lepton decay case.

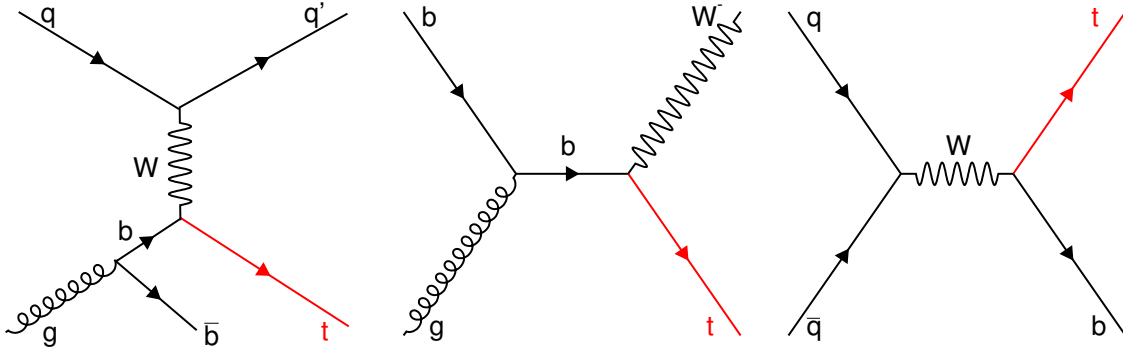


Figure 2.3: Feynman diagrams for single-top production. The signal is the diagram on the left,  $t$ -channel single-top production. It is also possible to have a version of this diagram without the incoming gluon and outgoing  $\bar{b}$ . The central diagram is  $Wt$  production and the diagram on the right is  $s$ -channel single-top production.

203 Figure 2.4 shows the diagrams for the other backgrounds for our single-top  $t$ -channel  
204 signal. These include multijets (also called QCD),  $W+jets$ ,  $Z+jets$ ,  $t\bar{t}$ , and diboson (includes  
205  $WW$ ,  $WZ$ , and  $ZZ$ ), where jets are streams of particle decays and interactions stemming from  
206 quarks that have hadronized. Of these, only  $t\bar{t}$  contains top quarks and it contains two of  
207 them, rather than the one top quark that single-top  $t$ -channel contains. Nevertheless, it is  
208 difficult to distinguish single-top  $t$ -channel from its backgrounds. This is partly because the  
209 final states can appear to be quite similar, especially given that the detector is not perfect  
210 at particle identification, and partly because of the smaller number of expected signal events  
211 relative to background events.

212 Although the diagrams in Figures 2.4 and 2.3 are basic, straight-forward diagrams, it is  
213 possible in more complex diagrams with extra gluons in the initial or final state, or loops of  
214 particle production (such as a gluon making two gluons which in turn recombine into one  
215 gluon). These extra possibilities can be described in separate diagrams, and it is possible to  
216 have diagrams from two different processes which give the same final state. In this case, the

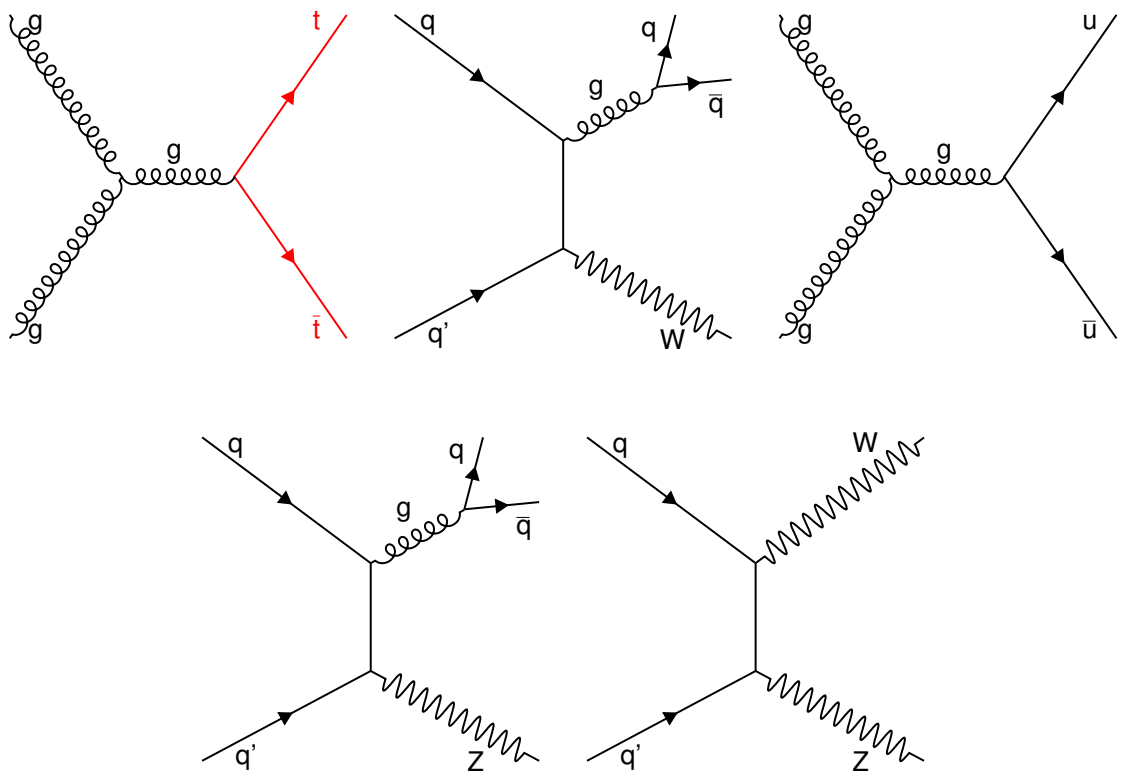


Figure 2.4: Feynman diagrams for backgrounds to single-top production. The  $t\bar{t}$  is the diagram on the top left,  $W+\text{jets}$  is the top central diagram and multijet production is the top right diagram. The final two diagrams are the smallest backgrounds,  $Z+\text{jets}$  on the bottom left and diboson on the bottom right.

217 diagrams are said to interfere and it is important to consider such things when generating  
218 Monte Carlo (MC). For the signals and backgrounds considered in this analysis, there are two  
219 cases of interference in particular. The first is single-top Wt production and  $t\bar{t}$  production.  
220 Wt is already very similar to  $t\bar{t}$  except for a b-quark (a top quark decays to a W and a  
221 b-quark). If a gluon in the Wt initial state produces the incoming b, it will also produce  
222 an outgoing  $\bar{b}$ , making the final state look like  $t\bar{t}$ . This does not have a large contribution  
223 to the analysis however, as this  $\bar{b}$  is generally low in  $p_T$ . The  $p_T$  requirement for jets (see  
224 Section 4.3) generally removes this from consideration. However, the scenario is considered  
225 when MC is generated.

226 Another possibility involves the t-channel single-top signal. If the incoming quark is from  
227 a gluon instead of a valence quark, the gluon produces the incoming quark plus an extra  
228 quark for the final state. The new final state contains two light quarks, t, and a possible  
229 b. This is the same final state discussed in the last paragraph, if the W decays to two light  
230 quarks instead of a lepton and neutrino in the case of Wt and for one of the top quarks in  
231 the case of  $t\bar{t}$ . However, this sort of initial state is very uncommon. Also, the extra particles  
232 from the gluons often having low  $p_T$  (thus not satisfying the jet definition), so this scenario  
233 does not impact the analysis.

### 234 2.3.2 Cross-section

235 The cross-section for a process reflects how often we expect a collision to produce that  
236 particular process. It is often useful to think of it in terms of the number of events produced:

$$N = \sigma L \quad (2.4)$$

237 where  $N$  is the number of events,  $\sigma$  is the process cross-section and  $L$  is the integrated  
238 luminosity (explained in Section 3.1), which represents the number of collisions.

239 The cross-section may include additional factors like k-factors or branching ratios. The  
240 k-factors are corrective fractions which change a cross-section from a leading order to next-to-  
241 leading order value, for example. A leading order (LO) cross-section is a theory calculation  
242 involving just basic diagrams without loops or extra vertices. Next-to-leading order (NLO)  
243 includes an additional level of complexity of loops and vertices, making it a longer, more  
244 difficult calculation. With each step up in completeness, the calculation becomes more  
245 technically difficult, so we do not have exact theoretical cross-sections for our processes.

246 Branching ratios (BR) are just fractions to change the total cross-section for a complete  
247 process to a partial cross-section. For instance, in the  $t$ -channel diagram, the final state  
248 involves a top quark, which decays to a b quark and a W. This W may decay either to two  
249 more quarks, like up and down quarks, or to a lepton and neutrino. For reasons discussed  
250 in Section 6, we require exactly one lepton in our selection and only generate Monte Carlo  
251 for final states including a lepton. Thus, the cross-section we actually normalize the MC  
252 to is the fraction of the total cross-section that involves a single lepton in the final state.  
253 The probability for the W to decay to a lepton and neutrino is a branching ratio that is  
254 multiplied with the cross-section.

255 The cross-sections used in this analysis for the signals and backgrounds are listed in  
256 Table 2.2 for 7 TeV collisions, including k-factors (if applicable) and branching ratios. They  
257 are given in the standard units of picobarns ( $pb$ ), where a barn is  $10^{-28} m^2$ . The W+jets is  
258 divided here by flavor in some cases. A special procedure is applied to separate the W+jets  
259 into light and heavy flavors later in the analysis based on the truth-level hadron type, in a

way that avoids double-counting events. Truth level refers to monte carlo information about  
 the particle generated before applying detector effects (see Chapter 4). The division is into  
 light ( $u,d,s$ ),  $c$ , and heavy ( $c\bar{c}$  and  $b\bar{b}$ ) for the jets (the processes may also have additional  
 light jets). The k-factors used here are 1.20 for  $W+jets$  in general (except  $W+cjets$ , which  
 uses 1.52), 1.25 for  $Z+jets$  and 1.12 for  $t\bar{t}$ .

Measuring  $t$ -channel single-top production is the focus of this analysis but we would  
 like to compare the measurement with an expected cross-section value. For this we use the  
 cross-sections given in Table 2.1 [19, 20, 21], and the branching ratios from the PDG, with  
 values of 10.75% for  $W \rightarrow e\nu_e$ , 10.57% for  $W \rightarrow \mu\nu_\mu$ , and 11.25% for  $W \rightarrow \tau\nu_\tau$  [11]. The  
 cross-sections contain both top and anti-top contributions, and we expect these particle and  
 anti-particle contributions to be different for processes that have valence quarks in the initial  
 state. The LHC collides two protons, each of which contains two up and one down quarks,  
 leading to an excess of positively charged quarks. For the  $t$ -channel, which usually has a  
 valence quark in the initial state, the standard model cross-section contains 41.9 pb due to  
 events containing  $t$  quarks and 22.7 pb from events containing  $\bar{t}$  quarks.

Process	Cross-section [pb]
$t$ -channel	$64.57 + 2.71 - 2.01$ pb
$Wt$	$15.74 + 1.06 - 1.08$ pb
$s$ channel	$4.63 + 0.19 - 0.17$ pb

Table 2.1: (N)NLO cross-sections for single-top processes [19, 20, 21]

It is also interesting to note that the difference between the signal cross-section and  
 background cross-sections are different by many orders of magnitude, as seen in Table 2.2.  
 This means that many, many events have to be identified correctly and rejected in order to  
 try to pick out our needle in this immense haystack.

Process	Cross-section [pb]
$t\text{-channel} \rightarrow e\nu_e$	6.9
$t\text{-channel} \rightarrow \mu\nu_\mu$	6.8
$t\text{-channel} \rightarrow \tau\nu_\tau$	7.3
$t\bar{t}$ (non-hadronic)	90
$Wt$	16
$s\text{-channel} \rightarrow e\nu_e$	0.50
$s\text{-channel} \rightarrow \mu\nu_\mu$	0.49
$s\text{-channel} \rightarrow \tau\nu_\tau$	0.52
$Z + 0$ jet	835
$Z + 1$ jets	168
$Z + 2$ jets	51
$Z + 3$ jets	14
$Z + 4$ jets	4
$Z + 5$ jets	1
$W + 0$ jet	8,300
$W + 1$ jets	1,600
$W + 2$ jets	460
$W + 3$ jets	120
$W + 4$ jets	31
$W + 5$ jets	8
$W + b\bar{b} + 0$ jet	57
$W + b\bar{b} + 1$ jets	43
$W + b\bar{b} + 2$ jets	21
$W + b\bar{b} + 3$ jets	8
$W + c\bar{c} + 0$ jet	153
$W + c\bar{c} + 1$ jets	126
$W + c\bar{c} + 2$ jets	62
$W + c\bar{c} + 3$ jets	20
$W + c + 0$ jet	980
$W + c + 1$ jets	312
$W + c + 2$ jets	77
$W + c + 3$ jets	17
$W + c + 4$ jets	4
$WW$	17
$WZ$	6
$ZZ$	1

Table 2.2: Cross-sections, including branching ratios and k-factors. Shown for one lepton decay (ex. electron) in the case of Z+jets and W+jets processes. Single-top  $s$ -channel and  $t$ -channel list different lepton decays for the W separately to show the branching ratios used.

279        Most of these cross-sections listed are fairly well known, partly because they are so  
280        much larger (relatively), and large statistics samples have been available for some time at  
281        long running experiments (like the Tevatron experiments) with relatively low systematic  
282        uncertainties. However, lower cross-section processes such as our signal have only recently  
283        been observed and the cross-sections are not necessarily well measured. The goal of this  
284        analysis is to provide a cross-section measurement of the  $t$ -channel process and to see if it  
285        agrees with the standard model prediction.

## 286        **2.4 New Physics Possibilities**

287        In recent years, there have been several indications that the standard model does not ex-  
288        plain everything. Although the standard model has been very successful, observations in  
289        astronomy have indicated the presence of so called dark matter [22] and dark energy [23]  
290        which are not predicted by the standard model and in proportions larger than the standard  
291        model matter we know of [24]. Several theories have been proposed to account for this , but  
292        none have been shown to exist. It is importation to check the standard model with detailed  
293        experimental measurements, to confirm the standard model and perhaps gain information  
294        about new physics if deviations are discovered.

295        Single-top  $t$ -channel production, a standard model process, is interesting because it is  
296        still new and not fully examined. Although it is now known to exist, we are only now  
297        accumulating enough events to do precision measurements of the cross-section. If this cross-  
298        section is not consistent with the standard model, it may indicate new physics. It is possible  
299        that there could be a flavor changing (like the  $W$ ) neutral current (neutral like the  $Z$ ) in the  
300        process for instance, that would change the  $Wtb$  vertex. It is also possible there could be a

301 fourth generation of quarks, which would again cause the CKM matrix  $V_{tb}$  value to deviate  
302 the standard model value. Detailed measurements of the single-top production allow direct  
303 evidence of these phenomena.

304 In this document, we take the first step, which is to measure the  $t$ -channel single-top cross-  
305 section and compare it to the standard model value. We do this by applying a small number  
306 of kinematic requirements to the events, to provide a straight-forward measurement. This  
307 is the first cut-based analysis with this level of precision on the single-top  $t$ -channel cross-  
308 section. It is also possible to use more sophisticated statistical methods to do a measurement  
309 of this signal, and the usefulness of this approach is explored in Appendix B.

<sub>310</sub> **Chapter 3**

<sub>311</sub> **ATLAS and the LHC**

<sub>312</sub> In order to study the single-top  $t$ -channel cross-section, we must first collect information  
<sub>313</sub> from these rare events. The top quark is very massive and requires a large amount of energy  
<sub>314</sub> to produce events containing it. To do this, we generate high energy particles in beams and  
<sub>315</sub> collide them together in an underground ring. Here, we can collect most of the information  
<sub>316</sub> about the particle tracks and energies and also produce a large number of these collisions.  
<sub>317</sub> This last point is crucial for low cross-section processes like the signal in this analysis.

<sub>318</sub> **3.1 The Large Hadron Collider, a Short Overview**

<sub>319</sub> The Large Hadron Collider [25], or LHC, is the particle collider in question, a proton-proton  
<sub>320</sub> collider located on the border of Switzerland and France, near Geneva, Switzerland. It is  
<sub>321</sub> 26.7 km in circumference, or 5.3 miles in diameter, and the beams collide with a center-of-  
<sub>322</sub> mass energy of 7 TeV during normal data taking. This is half of the design center-of-mass  
<sub>323</sub> energy (14 TeV) and is what is used for the data in this analysis. The first 7 TeV collisions  
<sub>324</sub> occurred in March of 2010, and this document considers data taken in the first half of 2011.

325        The LHC is the main ring, which reuses the former LEP tunnel, and there are several  
326   other rings that boost the beam up to its injection energy of 450 GeV. First, though there  
327   is the proton source, where hydrogen gas is separated into protons and electrons via a  
328   magnetic field. The protons are then sent into the first part of the accelerator complex, a  
329   linear accelerator called the LINAC2. It is also possible to collide lead in the LHC and in this  
330   case a different source is used, but for our purposes we will focus on the standard proton-  
331   proton collisions. After reaching the LINAC2, the protons go through circular accelerators  
332   to boost the beam energy, the Proton Synchrotron Booster (PSB), Proton Synchrotron (PS),  
333   and Super Proton Synchrotron (SPS) systems, before being injected into the LHC.

334        The protons are formed into bunches and trains of bunches before they are collided,  
335   incidentally allowing some spacing for one collision's particles to decay or leave the detector  
336   before the next set of particles collide. Within one bunch there are about 100 billion protons,  
337   not all of which actually collide or collide to produce interesting events. Each bunch is spaced  
338   apart by 50 ns and the number of bunches in the ring has been increasing steadily as data  
339   taking has progressed, up to about 1000.

340        Of course, the reason these bunches are put so close together and contain so many  
341   particles is related to getting enough data to find the single-top t-channel production we are  
342   looking for. The instantaneous luminosity [26], which reflects how many events are produced,  
343   is determined by various accelerator settings:

$$L = \frac{f_r n_1 n_2 n_b \gamma r F(\theta, \sigma)}{4\pi \epsilon_n \beta^*} \quad (3.1)$$

344        Here  $f_r$  is the frequency the protons go around the main LHC ring (approximately the  
345   speed of light,  $c$ , divided by 27 km),  $n_1$  and  $n_2$  are the number of protons per bunch,  $n_b$

346 is the number of bunches in each beam,  $\epsilon_n$  is the normalized emittance (related to the  
 347 deviation of particles from the ideal beam and thus also beam lifetime), and  $\beta^*$  is related  
 348 to the beam focus at the interaction point. The combination  $\epsilon_n \beta^*$  is the overall beam size  
 349 at the collision point. Here, the  $\beta^*$  is 1.5 m and the emittances are on the order of  $\mu\text{m}$ ,  
 350  $4 \times 10^{-6} \text{ m}$  [27]. The  $\gamma_r$  is the relativistic  $\gamma$ , which is just the beam energy (3.5 TeV per  
 351 beam) divided by the proton mass (about  $1 \text{ GeV}/c^2$ ), about  $3.5 \times 10^3$ . Finally, the  $F(\theta, \sigma)$   
 352 is a geometrical luminosity reduction factor related to the beam size and crossing angle, and  
 353 is about 0.84 [28]. The peak instantaneous luminosity varies day by day (it will fall off as a  
 354 data collection run goes on), but is approximately  $1 \times 10^{33} \text{ cm}^{-2} \text{ s}^{-1}$  for the time period in  
 355 question. Following the equation, and putting in approximate values, we can get a similar  
 356 number:

$$L = \frac{10^4 \text{ s}^{-1} \cdot 10^{11} \cdot 10^{11} \cdot 10^3 \cdot 3.5 \times 10^3 \cdot 0.84}{4\pi \cdot 4 \times 10^{-4} \text{ cm} \cdot 1.5 \times 10^2 \text{ cm}} = 4 \times 10^{32} \text{ cm}^{-2} \text{ s}^{-1} \quad (3.2)$$

357 With such tight beam focus and so many particles, it is possible to have more than one  
 358 collision per bunch crossing. On average, for the data we consider here, there are about six  
 359 interactions per crossing. The impact of the change in  $\beta^*$  for the data used for this analysis  
 360 and the following data can be seen in Figure 3.1. The decrease in  $\beta^*$  approximately doubled  
 361 the number of events per crossing in later data sets. The lower number of interactions  
 362 per crossing is an advantage of the data set used in this document. Most of these extra  
 363 interactions are not interesting, but it is possible that the events could mix in a way that  
 364 confuses the event identification. Studies are done to check that the analysis is not biased  
 365 by these “pileup” effects.

366 What is typically quoted is not the instantaneous luminosity but the integrated luminosity

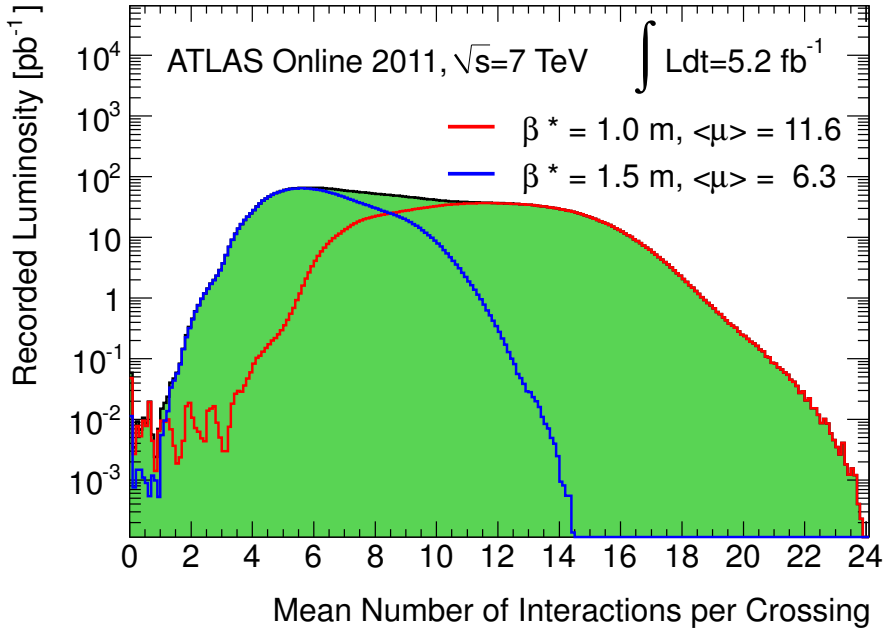


Figure 3.1: Average number of interactions per crossing for the 2011 ATLAS data set for different values of  $\beta^*$  used by the LHC. The  $\beta^* = 1.5 \text{ m}$  data set was used for the analysis in this document [29]. ATLAS Experiment ©2011 CERN.

367 (luminosity for a given period of time). This is usually expressed in units like  $\text{pb}^{-1}$  (a barn  
 368 is  $10^{-28} \text{ m}^2$ ), which means this can be easily multiplied by a cross-section in  $\text{pb}$  to determine  
 369 the number of events expected, as seen in Section 2.3.2. For this analysis, we are considering  
 370  $1035.27 \text{ pb}^{-1}$ , or  $1.04 \text{ fb}^{-1}$ .

371 However, even after all of these events are produced, nothing can be measured without  
 372 a detector to collect the relevant information about the collision. The information provided  
 373 is not a snapshot of the interaction we are interested in like the Feynman diagrams in  
 374 Section 2.3.1, but rather the final, relatively stable particles that come out of it which  
 375 actually reach the detector. There are four different detectors located around the LHC ring  
 376 at different points where the beams cross to produce collisions, and this analysis uses data  
 377 from the ATLAS detector.

## <sup>378</sup> 3.2 The ATLAS Detector

<sup>379</sup> The ATLAS (A Toroidal LHC ApparatuS) detector [30], shown in Figure 3.2 is a multipur-  
<sup>380</sup> pose detector designed to detect many different processes. It is a very large detector, the  
<sup>381</sup> largest constructed by volume, and is about 25 meters (or 82 feet) high. It consists of several  
<sup>382</sup> different detector components designed to detect the various particles that travel through it.  
<sup>383</sup> In general, these include b-quarks, lighter quarks, electrons, and muons (as well as photons,  
<sup>384</sup> but these don't appear in our final state). The quarks hadronize to form "jets" of particles  
which are actually detected in the detector.

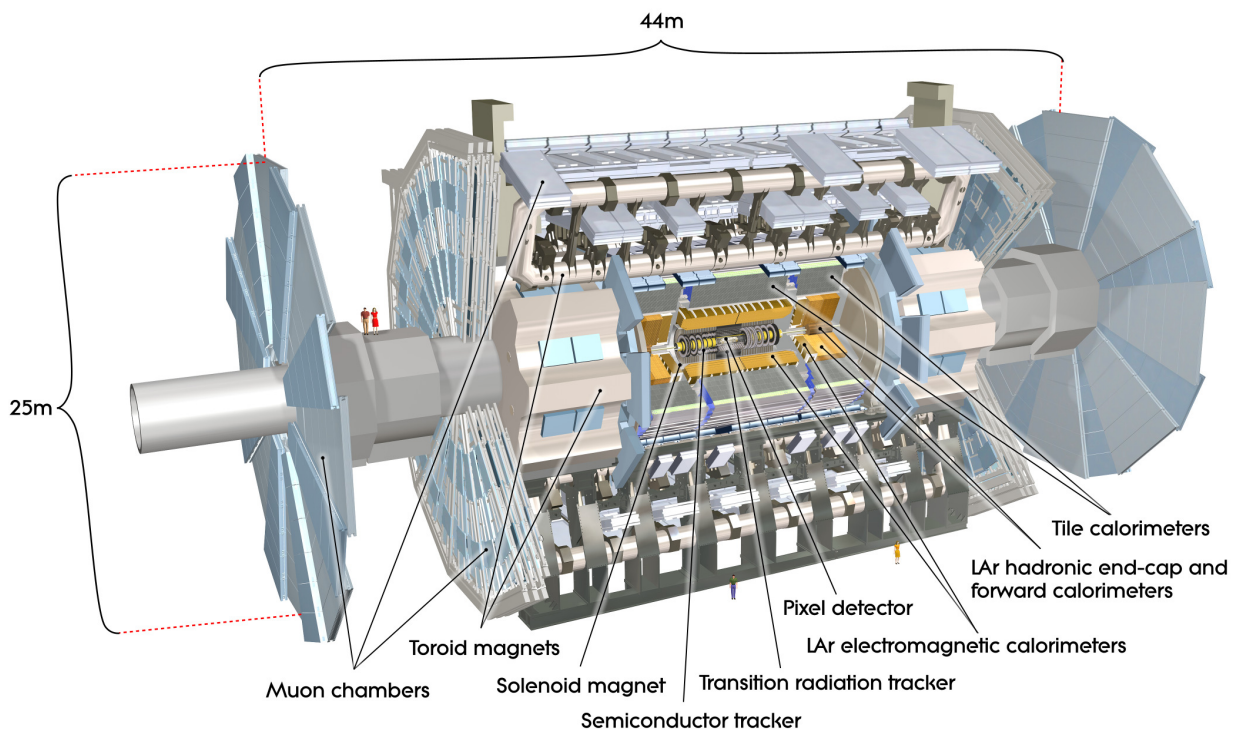


Figure 3.2: Cut away view of the ATLAS detector [30], ATLAS Experiment ©2008 CERN.

### 386 3.2.1 Detector Variables and Geometry

387 There is certain information that is determined in the detector itself: energy, timing and  
388 particle track information. The layout of the detector is with the z-axis along the beamline.  
389 The y-axis points up vertically from the detector and the x-axis is the remaining direction,  
390 pointing towards the center of the LHC ring. The  $\phi$  direction is the angle measured in the x  
391 and y plane, starting from the positive x axis, and the  $\theta$  direction is measured in the y and z  
392 plane, starting from the positive z axis. Figure 3.2.1 shows the orientation of the axes with  
393 respect to the surrounding area.

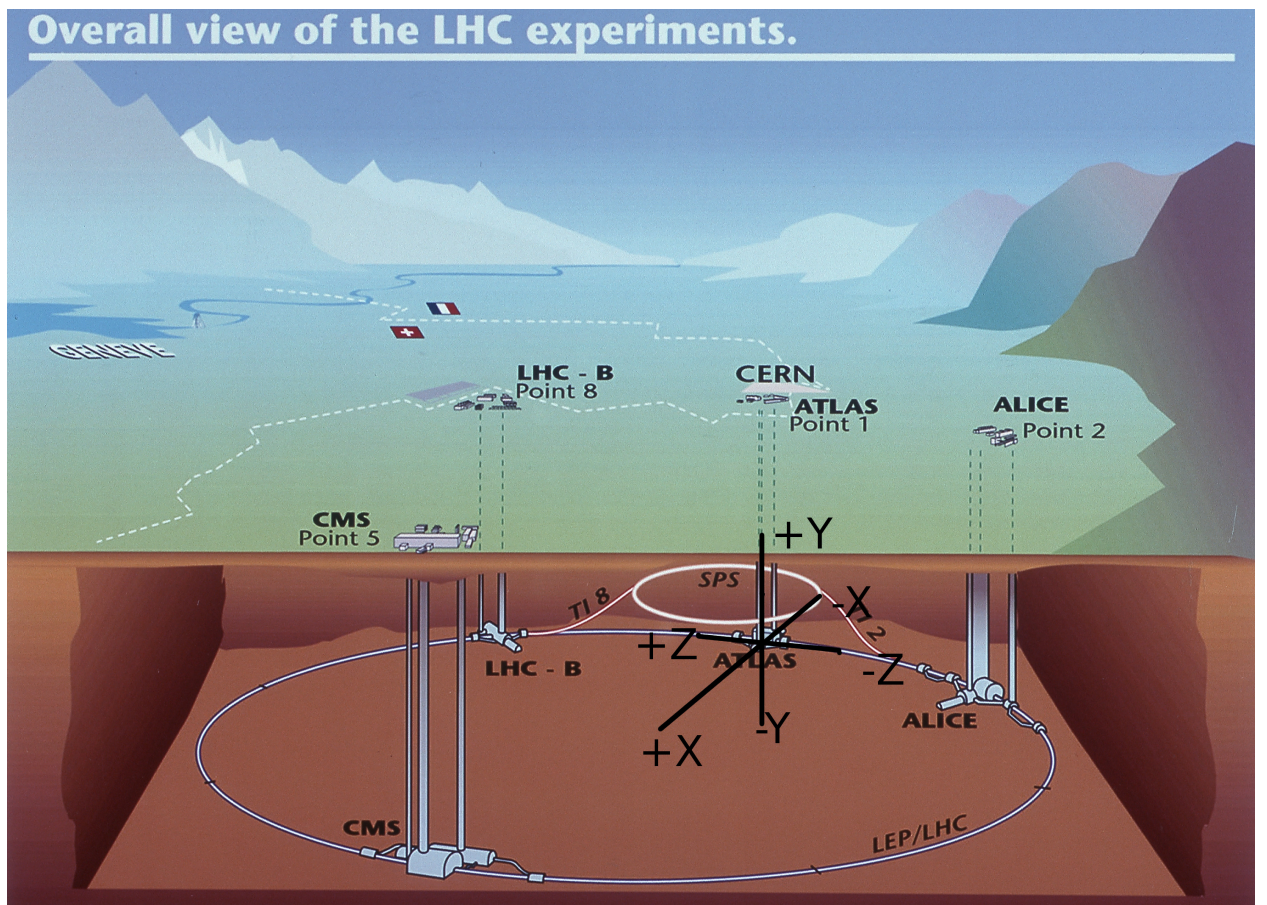


Figure 3.3: View of ATLAS, the LHC and other experiments [31], ATLAS Experiment ©1999 CERN. The black axis lines are added for reference.

394     The  $\theta$  angle is generally not used as such but transformed into a quantity called pseudo-  
395     rapidity ( $\eta$ ):

$$\eta = -\ln(\tan(\theta/2)) \quad (3.3)$$

396     This quantity is 0 if the particle heads out of the interaction perpendicular to the beam  
397     ( $\theta = 90^\circ$ ) and is about 4.5 close to the beamline ( $\theta = 1^\circ$ ), at the limit of the detector.

398     Figure 3.2.1 shows absolute values of  $\eta$  for various values of  $\theta$ .

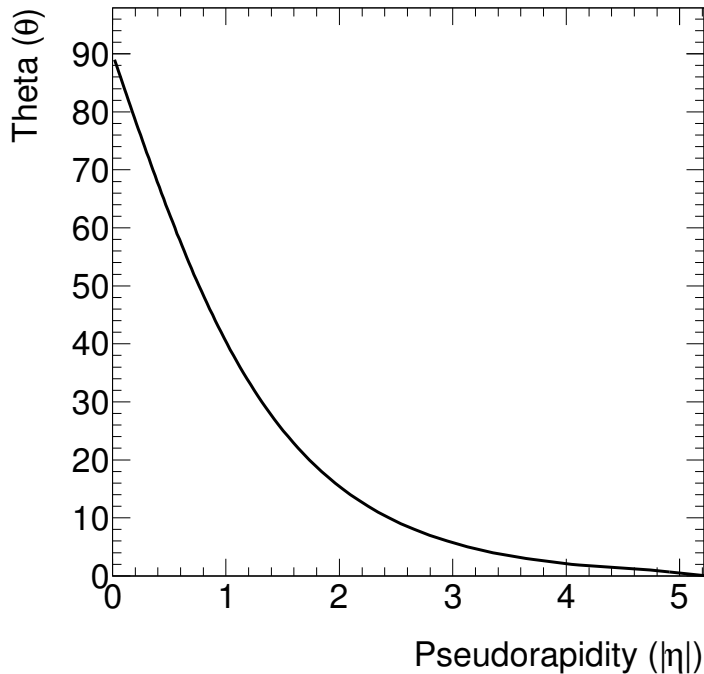


Figure 3.4: Graphic showing absolute values of  $\eta$  for various values of  $\theta$ .

399     It is also common to use the quantity  $\Delta R$  as a measure of separation. We define this as:

$$\Delta R^2 = \Delta\eta^2 + \Delta\phi^2 \quad (3.4)$$

400     Additionally, the term transverse in this document (denoted by a subscript T) means the

401 combination of the X and Y directions, which is perpendicular to the beam direction along  
402 the z axis. For instance,  $p_T$  is the transverse particle momenta,  $\sqrt{p_X^2 + p_Y^2}$ .

### 403 3.2.2 The Inner Detector

404 The inner detector has the finest resolution of the various sub-detectors. The fine resolution  
405 is particularly important for identifying and reconstructing hadronized b-quarks, or b-jets,  
406 which will be discussed in more detail in Section 4.3.1. The primary purpose of the inner  
407 detector is tracking. This is also the closest detector to the beam pipe in the central region  
408 and covers a region of  $|\eta| < 2.5$ .

409 There are three major sections: Pixel, SemiConductor Tracker (SCT), and Transition  
410 Radiation Tracker (TRT). The Pixel is the innermost section and has an initial layer called  
411 the B-layer. The closeness of this layer to the interaction is limited by the beam pipe itself,  
412 which is about 6 cm in diameter. This section of the detector is composed of small squares of  
413 silicon (pixels) and offers very good postitional resolution, 10  $\mu m$  in R- $\phi$  space and 115  $\mu m$   
414 in Z. As charged particles hit the silicon, ionization electrons flow to anodes and a signal is  
415 created. There are three pixel layers circling the barrel region and an additional three layers  
416 on each side. The next section is the SCT. It is very similar to the pixel section but has  
417 microstrips of silicon about 6 cm long rather than pixels. It has four layers of back-to-back  
418 strips giving a possible 8 hits per track. The resolution is still good although not quite as  
419 precise as the pixel region particularly in the Z direction (17  $\mu m$  in R- $\phi$  space and 580  $\mu m$   
420 in Z).

421 Finally there is the TRT which is basically a two part detector. It consists of “straw  
422 tubes” which are tubes filled with Xenon gas and a wire down the middle. Each tube is 4

423 mm in diameter and 37 cm long in the endcap region or 144 cm long in the barrel region.

424 Around these tubes are various materials with different dielectric constants. When particles,

425 especially very high energy, low-mass particles like electrons pass through these different

426 materials, transition radiation is emitted. These photons hit the Xenon-filled tubes and

427 create ions which, because of a potential difference between the tube and the wire in the

428 center, drift towards the wire and cause a signal. This is particularly useful in helping with

429 electron identification, especially for  $|\eta| < 2.0$ . The position resolution in this section isn't as

430 good as the pixel or SCT detectors, but there are still about 300,000 straws over a large area,

431 and particles will have more "hits" in the TRT straws than the previous detector sections,

432 assisting with particle track reconstruction. The TRT only provides R- $\phi$  information and

433 can resolve to 130  $\mu m$  per straw. However, each track has approximately 36 hits in this

434 region, compared to 3 or 8 in the other two inner detector regions.

### 435 3.2.3 The EM Calorimeter

436 The electro-magnetic (EM) calorimeter is particularly intended to pick out the tracks and

437 energy of electrons and photons, which tend to stop in this region. It is composed of layers

438 of lead with steel and liquid argon (LAr), starting with an initial LAr layer called the

439 presampler which gathers information about showers that may have occurred in previous

440 detector material. Through the rest of the calorimeter, the electrons will interact with layers

441 of lead. There are three major layers, and most electrons of high enough energy for physics

442 analyses like this one are deposited in the central layer. This layer has 0.025x0.025 resolution

443 in  $\eta - \phi$  space. The first layer helps with rejection of photons or pions and the last layer helps

444 collect energy from very energetic electrons. More energetic electrons will make showers in

more of the lead layers. The showers themselves are detected via creation of ions in the LAr. Photons are also detected in this region and are distinguished from electrons by the lack of a track in the inner detector. There are two levels of coverage in this detector. The central region,  $|\eta| < 1.5$  contains slightly more layers and better resolution than the two-wheel endcap region,  $1.4 < |\eta| < 3.2$ . The resolution is worst in the forward region of this detector,  $2.5 < |\eta| < 3.2$ , and this analysis will not consider electrons from this region.

It should be noted that there is one particular region of the detector between the barrel and endcap in the EM calorimeter,  $1.37 < |\eta| < 1.52$ , where there is excessive extra material between the inner detector and the EM calorimeter [32]. This makes it difficult to properly reconstruct the energy of electrons that are detected, and of course they may deposit most of their energy in this region and never make it into the rest of the detector at all. This is sometimes referred to as the "crack" region and electrons from this region are not considered in the analysis.

### 3.2.4 The Hadronic and Forward Calorimeters

The hadronic calorimeter is where the hadronic showers from hadronizing quarks tend to reach and eventually stop. Here we complete the track and energy information for jets, the shower of particles from a hadronizing quark. The portion of the jets that hit the calorimeter are actually composed of various light particles, commonly including particles such as pions and kaons (which have masses of about 140 MeV and 500 MeV, respectively). This part of the detector is special because it contains not only a central and barrel region, but also a forward region which is next to the beam pipe (as is the inner detector). Each of the regions have some overlap with each other to avoid lining up too many detector transition regions

467 with each other (where resolution extra material is present and resolution is not as good).  
468 Extra material can cause extra interactions that may not be well modeled and particles could  
469 be missed, so it is important to minimize this.

470 The central region ( $|\eta| < 1.7$ ) contains scintillating tiles and steel, and is known as the tile  
471 calorimeter. The hadrons interact with the layers of steel and the showering particles create  
472 photons when they hit the scintillating tiles. These photons are then collected by photomul-  
473 tipliers, which turn the photons into an electrical signal. The barrel region ( $1.5 < |\eta| < 3.2$ )  
474 contains the hadronic end-cap calorimeters (HEC), which uses LAr and is essentially an  
475 extension of the EM calorimeter but with copper plates. There are three layers in the barrel  
476 and four in the endcap, with a resolution of about  $0.1 \times 0.1$  in  $\eta - \phi$  space for  $|\eta| < 2.5$  and  
477  $0.2 \times 0.2$  otherwise in the endcap region.

478 The forward region ( $3.1 < |\eta| < 4.9$ ) has special forward calorimeters right next to the  
479 beam pipe and thus has a different configuration to handle the larger amounts of radiation.  
480 Here, copper has tube-shaped holes formed in it with each hole containing a tungsten rod  
481 and LAr between the two. The particles shower in the copper and the ions form in the  
482 LAr and travel towards the rod. This region is especially important for the  $t$ -channel single-  
483 top searches as an energetic forward jet is a distinguishing characteristic between it and its  
484 backgrounds.

### 485 3.2.5 The Muon Spectrometer

486 Finally there is the muon system, primarily intended to detect muons, which tend to travel  
487 farther through the detector than other particles (except neutrinos, which interact so weakly  
488 that it is difficult to detect them). This is related to the mass of the muon, which is about

489 106 MeV (much larger than the electron, at 0.5 MeV), and its decay time, which is much  
490 longer than the particles like pions and kaons in jets. The longer decay time allows it to  
491 reach the outer regions of the detector ( $c\tau$  is 659 m) and its larger mass prevents it from  
492 showering too much earlier in the detector. Thus, we can have a special detector for muons,  
493 in the outermost portion of the detector, to determine information about the direction and  
494 momenta of the muons.

495 There are four major components of the muon system. Two components are dedicated  
496 to detecting the muon track and the other two are dedicated to reporting the presence of a  
497 muon (triggering) and giving additional position information. In each case, one component is  
498 in the barrel region and the other in the endcap region. The Monitored Drift Tubes (MDT)  
499 are primarily responsible for track determination over the full  $|\eta| < 2.7$  region, except for  
500 the inner section of the muon detector forward region ( $2.0 < |\eta| < 2.7$ ), where Cathode  
501 Strip Chambers (CSC) are used. The general principle is similar in both cases. There is  
502 a gas filling drift tubes or between plates, and a charged particle creates ions which drift  
503 towards a wire. The resolution of the MDT is about  $35 \mu\text{m}$  in the Z direction, while the  
504 CSC has a resolution of about  $40 \mu\text{m}$  in the plane orthogonal to  $\phi$  and 5 mm in the *phi*  
505 (non-bending) direction. The triggering portions are the Resistive Plate Chambers (RPC)  
506 and Thin Gap Chambers (TGC) in the central ( $|\eta| < 1.05$ ) and endcap ( $1.05 < |\eta| < 2.4$ )  
507 regions, respectively. The first is composed of sets of plates (no wires) that the ionized  
508 particles travel between. The second contains many wires between plates, like the CSC, but  
509 the wires are arranged differently to favor a faster response time. These extra triggering  
510 systems are needed because the response time of the main systems is too long to allow  
511 triggering of a high  $p_T$  muon associated with some events, and also to provide information

512 about the muon track in an additional ( $\phi$ ) direction. The RPC has a resolution of 10 mm  
513 in both the Z and  $\phi$  directions while the TGC has a resolution of 2 to 6 mm in Z and 3 to 7  
514 mm in  $\phi$ .

515 **3.2.6 Magnets**

516 It should be mentioned that one of the primary methods of measuring the momenta of  
517 charged particles is by measuring the curvature of their tracks in a magnetic field. Magentic  
518 fields also help to distinguish charged and neutral particles (whose tracks have no curvature  
519 due to a magnetic field), aiding in particle identification. Magnetic fields are created by  
520 two different sets of magnets in the ATLAS detector. The first set is a 2 Tesla solenoid  
521 magnet system located between the inner detector and the EM calorimeter which provides  
522 a magnetic field for the inner detector. In addition to providing a strong field the magnent  
523 coil and related structure must not be too thick or dense, as the particles are intended to  
524 pass through this magnet layer relatively unimpeded. The second set consists of large toroid  
525 magnets (about 0.5 to 1 T within the muon detector) surrounding the muon system, in  
526 both the barrel and endcap regions. The tendency of a particle to curve in a magnetic field  
527 indicates that it is charged, but the degree of curvature also gives information about the  
528 momentum of the particle. This can be seen from the equating the Lorentz and Centripetal  
529 force equations, giving (assuming non-relativistic conditions for the moment):

$$F = Bqv = mv^2/r \rightarrow mv = p = qBr \rightarrow p \propto r \quad (3.5)$$

530 where B is the magnetic field, q is the particle charge, v is particle velocity, r is the radius of  
531 curvature and p is the momentum. From this we can see that particles with more momentum

532 have a larger radius of curvature, meaning that the tracks will curve less (be straighter) in  
533 the detector. Particles that are not charged will not curve due to the magnetic field. Thus,  
534 these magnets are essential for particle identification and measurements.

### 535 **3.2.7 The Trigger and Data Collection**

536 Finally, there is the trigger and data collection system (DAQ) [33]. Although not strictly  
537 part of the ATLAS detector itself, per se, this system is essential to data analyses. The LHC  
538 produces collisions at such a high rate that it is impossible to store all of the collected data  
539 for analysis. Most of the data, however, are glancing or low energy collisions that are not  
540 the events we are looking for in studies of processes such as single-top. It is possible to reject  
541 many of these events immediately, using hardware triggers. There are then two other trigger  
542 levels which spend increasing amounts of time determining if an event is worth saving or not  
543 before the data are finally recorded for use in analyses.

544 The three different trigger levels are called level 1 (L1), level 2 (L2) and event filter (EF).  
545 At each level, more information is considered to determine if an event should be kept or  
546 rejected. This is important as computer storage space would rapidly run out if all events  
547 were kept. Most events are “common” events involving low energy jets. We want to be sure  
548 that we collect enough of the less common high energy events (like the single-top events we  
549 are looking for) so we reject many of these less interesting events.

550 The L1 trigger is hardware only and rejects events very quickly (less than  $2 \mu\text{s}$  per event)  
551 and in large number, with a maximum rate of 75 kHz [33, 32] although in practice the rate  
552 may be half this value. The other two triggers are software based. The L1 trigger essentially  
553 just looks for high transverse energy objects in the event, but the L2 trigger considers the

554 regions of interest (RoIs) containing these objects and can consider full detector information  
555 in these regions. The rate after the L2 decision is about 3 kHz and it takes about 50 ms per  
556 event to make a decision to keep or reject the event at this level. Finally the EF is the last  
557 level which looks at the whole detector and uses standard analysis reconstruction software to  
558 find the event information and make a decision. After this stage, the event is permanently  
559 stored and disseminated to analysers. The overall event rate at this level is about 200 to  
560 600 Hz, much smaller than before. It takes longer to determine whether to keep events at  
561 this level, about 4 CPU seconds per event by design (as low as 0.4 CPU seconds per event  
562 during data taking), but this is still quite fast.

563 There are many different types of triggers. In this analysis, we use single lepton triggers,  
564 corresponding to the single leptons expected in the t-channel single-top final state. When the  
565 data are processed, a low threshold trigger is initially applied, and higher threshold triggers  
566 are applied later at the analysis level. This application of the low threshold triggers divides  
567 the data into different analysis streams. In this document we use the Muon and Egamma  
568 (electron) streams for the main analysis. There is also another main physics stream, the  
569 JetTauEtMiss stream, which is used in this analysis for the multijet background estimate.

### 570 **3.2.8 Data Quality**

571 In some cases the detector may have a component temporarily fail or go offline, and it may  
572 not be possible to reconstruct certain particles well. In this case, events taken during these  
573 times are rejected due to data quality issues. This rejection is done “offline”, meaning it  
574 is performed after the initial low threshold triggers are applied, and removes data events  
575 from the analysis by applying a “good runs list” (GRL) selection as the first selection on

576 the data sample. This is because some analyses do not use the full detector, so even if some  
577 of the data for a muon analysis for instance are not collected correctly because of technical  
578 problems with the muon spectrometer, an analysis only using the inner detector information  
579 can still use the data. On the other hand, an analysis such as this one, which uses nearly  
580 the full detector range, would not be able to use such data.

581 One exception to this GRL selection is the so-called “LAr hole” issue, which was a  
582 problem with the front end electronics for the LAr calorimeter that created a “hole” in the  
583 detector data collection. This problem persisted for a few months before being fixed and was  
584 present for all but the first  $165 \text{ pb}^{-1}$  of the data set used in this analysis, meaning about  
585 85% of the data has the potential to be affected. In this case an additional event selection  
586 is applied to the data to account for this issue, removing only events where the particle  
587 reconstruction is affected by this hole (rather than removing all of the events, which would  
588 have been the standard GRL selection procedure for an analysis like this one). In the end,  
589 only about 10% of data events are actually removed from the analysis due to this issue.

590 **Chapter 4**

591 **Particle Reconstruction**

592 In order to do any sort of analysis, we must be able to compare the data from the exper-  
593 iment to the theory. The data collected by the ATLAS detector are not particularly easy  
594 to interpret at first glance. The data begin as energy deposits and tracks while the theory  
595 consists of simulated hadronized quarks, leptons and neutrinos (this is referred to as truth  
596 level MC). Truth level MC information is largely unused in this analysis. Instead, the two  
597 sets, data and MC, are processed to reconstruct the event and, in the case of MC, include de-

598 tector information like extra material or overlapping tracks affecting particle reconstruction.

599 Event reconstruction is applied to form particles and reconstruct the event, so at this level

600 there are quantities such as  $E_T^{\text{miss}}$  (missing transverse energy) rather than neutrinos and

601 jets rather than quarks. We will call this stage of processing (the final stage before analysis)

602 the reconstruction or detector level. At this point, the two sets, data and MC, should be

603 equivalent (for instance,  $E_T^{\text{miss}}$  distributions should be the same between the two if the data

604 are perfectly modeled by the MC). In the following sections, we will give the definitions for

605 a muon, electron, neutrino, or jet at the reconstruction level. We will also include criteria

606 that require particles to be separated and well reconstructed.

## 607 4.1 Electrons

608 Electrons appear to be narrow curving cones of energy in the detector. The narrow curving  
609 track, with a shorter trail of energy depositions through the detector than a muon, is its  
610 primary distinguishing feature. There are electrons that can occur in the detector from  
611 sources other than being directly produced in the main collision however, including electrons  
612 inside of jets and electrons from photon interactions. It is also possible to mis-identify narrow  
613 jets as electrons, or photons as electrons (such as from bremsstrahlung radiation, produced  
614 as the electron interacts in the detector material). In this analysis, we apply several criteria  
615 when identifying if a certain energy deposit and associated tracks are really an electron from  
616 the primary collision.

617 In the ATLAS experiment, there are three different initial electron selections which can be  
618 used in different analyses. These are referred to as loose, medium, and tight, where medium  
619 includes loose as well as extra medium requirements, and tight includes both medium and  
620 loose as well as extra tight requirements [32]. The more selections that are applied, the more  
621 confidence one has that the particle identified as an electron is really an electron, although  
622 you will also remove some real electrons which happen to fail these requirements (making  
623 it less efficient). For this analysis, we prefer to be sure that the particle is what we have  
624 identified it as (high purity), so we require the tight selection. Overall, this selection includes  
625 requirements to ensure that the energy deposits are narrow and where we expect them to  
626 be for an electron (the EM calorimeter), to reduce jets in particular being mis-identified as  
627 electrons, and that a track is well matched to this deposit and inner detector deposits, to

628 reduce photon conversions being mis-identified as electrons.

629 The requirements for tight electrons are given elsewhere [32], but we repeat them here  
630 for completeness. The loose selection requires the electron  $|\eta| < 2.47$ , low leakage of energy  
631 depositions into the hadronic calorimeter, and includes a requirement on energy deposits in  
632 the middle of the EM calorimeter, where most electron energy deposits would be expected  
633 to be. The shower width is examined in this layer as well. The medium selection has  
634 additional criteria related to the shower width using the first EM calorimeter layer and the  
635 deviation in the energies of the largest and second largest deposits in this layer. There are  
636 requirements related to the track, that there is at least 1 hit in the pixel portion of the inner  
637 detector, at least 7 hits from both the pixel and SCT, and that the track's transverse impact  
638 parameter,  $|d_0|$ , is less than 5 mm. The final medium requirement is related to track and  
639 cluster matching, requiring the distance in  $|\eta|$  between the cluster in the initial EM layer and  
640 the determined track to be less than 0.01. The final set of selections to make the electron  
641 tight include additional cluster and track matching requirements: that the distance in  $|\phi|$   
642 between the cluster in the middle EM layer and the determined track be less than 0.02,  
643 a requirement on the cluster energy divided by the track momentum, and tightens the  $|\eta|$   
644 distance requirement applied for medium electrons from 0.01 to 0.005. The  $|d_0|$  requirement  
645 is also tightened to be less than 1 mm. The TRT portion of the inner detector is used,  
646 introducing requirements on the total number of TRT hits and considering the ratio of high  
647 threshold hits to total hits in the TRT. Finally, there are requirements to reduce photon  
648 conversions. The number of B-layer hits (the first pixel detector layer) must be at least one  
649 and electron candidates that are matched to reconstructed photon conversions are rejected.

650 We further require electrons to have a transverse momentum ( $p_T$ ) of at least 20 GeV.

651 Electrons must also be isolated, meaning they are not near other particles. The isolation  
652 requirement is specifically optimized for single-top analyses and requires  $\text{etcone30}/\text{Et} < 0.15$   
653 and  $\text{ptcone30}/\text{Et} < 0.10$ .  $\text{Etcone30}$  and  $\text{ptcone30}$  refer to the amount of transverse energy  
654 deposited or track momentum in a cone around the electron track(s) with a  $R$  of 0.3, where  
655  $\Delta R = \sqrt{\Delta\eta^2 + \Delta\phi^2} < 0.3$ . Electrons must also have  $|\eta| < 2.47$ , and exclude the region  
656  $1.37 < |\eta| < 1.52$  due to detector limitations. Additionally, if electrons fall within the LAr  
657 hole, then they are not considered to be electrons.

## 658 4.2 Muons

659 Muons are primarily distinguished by their relatively long lifetimes and long, curved tracks  
660 which reach into the muon calorimeter section of the detector. Muons are required to satisfy  
661 several strict quality requirements. As with electrons, the muons have several categories  
662 for an initial identification definition. In this case, the categories refer to different muon  
663 reconstruction algorithms. The one used here is the “combined muon” [34, 35] algorithm,  
664 which considers both inner detector and muon spectrometer tracks, which are reconstructed  
665 separately. A combined fit is performed on the tracks from the two detectors to form a final  
666 muon track. If a combined track cannot be formed, the particle is not considered to be a  
667 muon. Of the different algorithms, this is the one that has the highest purity.

668 There are a few track quality requirements used to define a muon which are related to  
669 inner detector information, including at least one B-layer hit, at least two pixel hits, and  
670 SCT and TRT hit and quality requirements. These are a bit detailed, and are given here for  
671 completeness. We require the flag `expectBLayerHit` to be false or the number of BLayer hits  
672  $> 0$ , meaning there must be a hit in the B-layer unless the track passes through a dead area

673 of the detector. A muon must have the number of pixel hits plus the number of crossed dead  
674 pixel sensors  $\geq 2$ , the number of SCT hits plus the number of crossed dead SCT sensors  
675  $\geq 6$ , and the number of pixel holes plus the number of SCT holes  $\leq 2$ . Holes are where a  
676 module did not respond as expected, even though modules elsewhere along the track did.  
677 Finally, there is a complex requirement on the number of TRT hits divided by the number  
678 of outliers related to the quality of the track fit, where outliers are hits that deviate from  
679 the track. We require, where  $n$  is the number of TRT hits plus the number of TRT outliers,  
680  $n \geq 6$  and the number of TRT outliers divided by  $n$  to be  $< 0.9$  for  $|\eta| < 1.9$ . Then we also  
681 require the number of TRT outliers divided by  $n$  to be  $< 0.9$  if  $n \geq 6$  for  $|\eta| \geq 1.9$ . In this  
682 last case, if  $n < 6$ , the event will pass, unlike the first case.

683 The isolation requirement is the same as the electron isolation requirement, namely that  
684  $\text{etcone30}/\text{Et} < 0.15$  and  $\text{ptcone30}/\text{Et} < 0.10$ . The muons we select are specifically not  
685 allowed to overlap in position with jets, meaning any muon candidate within  $\Delta R$  of 0.4 of  
686 a jet is not considered. For this purpose, we consider all jets with  $p_T$  above 20 GeV and  
687 include jets that overlap with electrons. Additionally muons must have  $p_T > 20$  GeV and  
688  $|\eta| < 2.5$ .

### 689 4.3 Quarks

690 Perhaps the most complex reconstructed objects in the detector are jets. Jets are hadronized  
691 quarks, showers of many particles that tend to be absorbed in the hadronic calorimeter.  
692 Because they are basically sprays of particles, it is possible for them to overlap and be in  
693 odd shapes. In order to work with these, we need to understand which energy deposits  
694 correspond to which jets.

695       The method used to form jets in this analysis is an algorithm called the anti- $k_t$  algo-  
696       rithm [36]. There are two major jet algorithm types, cone and clustering algorithms, where  
697       anti- $k_t$  is a clustering algorithm that forms jets that happen to have very cone-like shapes.  
698       A clustering algorithm is a bottom-up algorithm that combines individual tracks together  
699       to form a jet, while a cone algorithm is a top-down algorithm which forms a cone for the  
700       jet and considers deposits within that cone part of the jet. For this algorithm, the area in  
701        $\eta - \phi$  space is  $\pi R^2$ . This is the area containing energy deposits associated to one particular  
702       jet, assuming that there are no other high  $p_T$  (hard) objects within a distance  $2R$ . For this  
703       analysis we use a cone size  $R$  of 0.4. If there is another hard jet, the harder jet will have  
704       a cone shape and the lower  $p_T$  (soft) jet will have a crescent shape. The anti- $k_t$  algorithm  
705       is used because not only is it reasonably fast, but the jets are grouped using the highest  
706        $p_T$  energy deposits first and then looking at surrounding objects, meaning that random low  
707       energy deposits will not change the jet shape. This means it is infrared safe because it avoids  
708       potential divergences from an infinite number of very soft, low energy jets. Also, each deposit  
709       and track is assigned to some jet. There is no splitting and merging of overlapping jets, so it  
710       doesn't matter if a jet is split into two parallel (collinear) particles, making it collinear safe.

711       The jet energies are corrected from what is actually measured in the detector to what we  
712       have in the MC simulation. The first correction is to the “EM scale”, the main correction to  
713       the detected energy, based on test beam and cosmic ray studies. The second correction is a  
714       jet energy scale (JES) correction [37, 38], an additional calibration based on the jet  $p_T$  and  
715        $\eta$ . It includes corrections for losses due to dead material or leakage energy from particles  
716       depositing energy outside the hadronic calorimeter. The jets are thus called “EM-JES”  
717       calibrated jets [39]. Specifically, we use jets called AntiKt4TopoEMJets, where Topo refers

718 to topological clusters [37, 40]. This is an algorithm that clusters energy deposits together  
719 for the jet, by starting with an energetic deposit with a signal to noise ratio greater than 4,  
720 and adding neighboring deposits that have a signal to noise ratio greater than 2.

721 We have additional quality requirements. We remove any jets that have been recon-  
722 structed with corrected energy that is negative and thus are not physical (this is a very  
723 small effect). Any jet candidates that overlap with electrons with  $\Delta R < 0.2$  are not consid-  
724 ered. Further, we require jets to have  $p_T > 25$  GeV and  $|\eta| < 4.5$ . Notice that this is a much  
725 more forward requirement than that of the leptons. The calorimeters allow information this  
726 far forward in the detector and it is particularly important information for our analysis.

### 727 4.3.1 b-tagging

728 There are two subsets of jets that are used frequently in this analysis, tagged and untagged.  
729 Jets that are b-tagged (tagged) are required to have a high probability of being a hadronized  
730 b-quark. The rest remaining jets are referred to as untagged. Additionally, jets must have  
731  $|\eta| < 2.5$  to be b-tagged because of the inner detector range. This means all jets with  
732  $|\eta| > 2.5$  are considered untagged.

#### 733 4.3.1.1 How b-quarks are Identified

734 The bottom quark is an unusual particle. It is heavy, as mentioned above, and it also travels  
735 quite a long distance, relatively, from its creation before it forms a jet (b-jet). The lifetime  
736 of the b-quark is about  $\tau = 1 \times 10^{-12}$  seconds. We can determine the distance it should  
737 travel, on average, by assuming an energy of about 40 GeV. Because  $E = \gamma mc^2$  and  $d = \gamma c\tau$ ,  
738 where  $\tau$  is the lifetime,  $m$  is the mass (about 4 GeV/c<sup>2</sup>) and  $E$  is the energy, we can write,

739 where  $c$  is the speed of light  $c = 3 \times 10^3 \text{ m/s}$ ):

$$d = \frac{E}{mc^2} c\tau \approx \frac{40}{4} \cdot 3 \times 10^8 \text{ m/s} \cdot 1 \times 10^{-12} \text{ s} = 0.003 \text{ m} \quad (4.1)$$

740 This means that the b's travel about 3 mm from the main interaction point before forming  
741 a jet.

742 Tracks from the inner detector can be reconstructed and traced back inside the beam pipe  
743 (where there is, of course, no detector). These tracks will then intersect within the beam  
744 pipe, which has a diameter of about 6 cm. Most intersect in a primary vertex, the place the  
745 proton-proton collision occurred. However, some may intersect in other places, secondary  
746 vertices, where a b hadron has formed a jet (see Figure 4.1). Of course, as there are multiple  
747 proton-proton collisions producing pileup events, and just more particles in general, it can  
748 be difficult to really distinguish which tracks go where, and to which vertex. This is why  
749 the inner detector resolution is so very important and also the reconstruction algorithms to  
750 determine these vertices. Because of the importance of the inner detector, b-tagged jets are  
751 only defined within its range,  $|\eta| < 2.5$ .

752 The chosen b-tagger is just a distribution related to the likelihood of a jet coming from  
753 a b, and a jet is b-tagged based on whether the b-tagger value for that jet is above or  
754 below a certain threshold, called an operating point. A jet is considered to be mis-tagged  
755 if the jet was not really from a b-hadron but was still b-tagged. Different operating points  
756 have different levels of performance. There are two major ways to determine performance,  
757 the b-tagging efficiency and the mis-tagging efficiency. These two measures are inversely  
758 proportional, so a high b-tagging efficiency sample will have low mis-tagging efficiency. This  
759 means that if the b-tagging efficiency is high, most of the jets that are really b-hadrons will

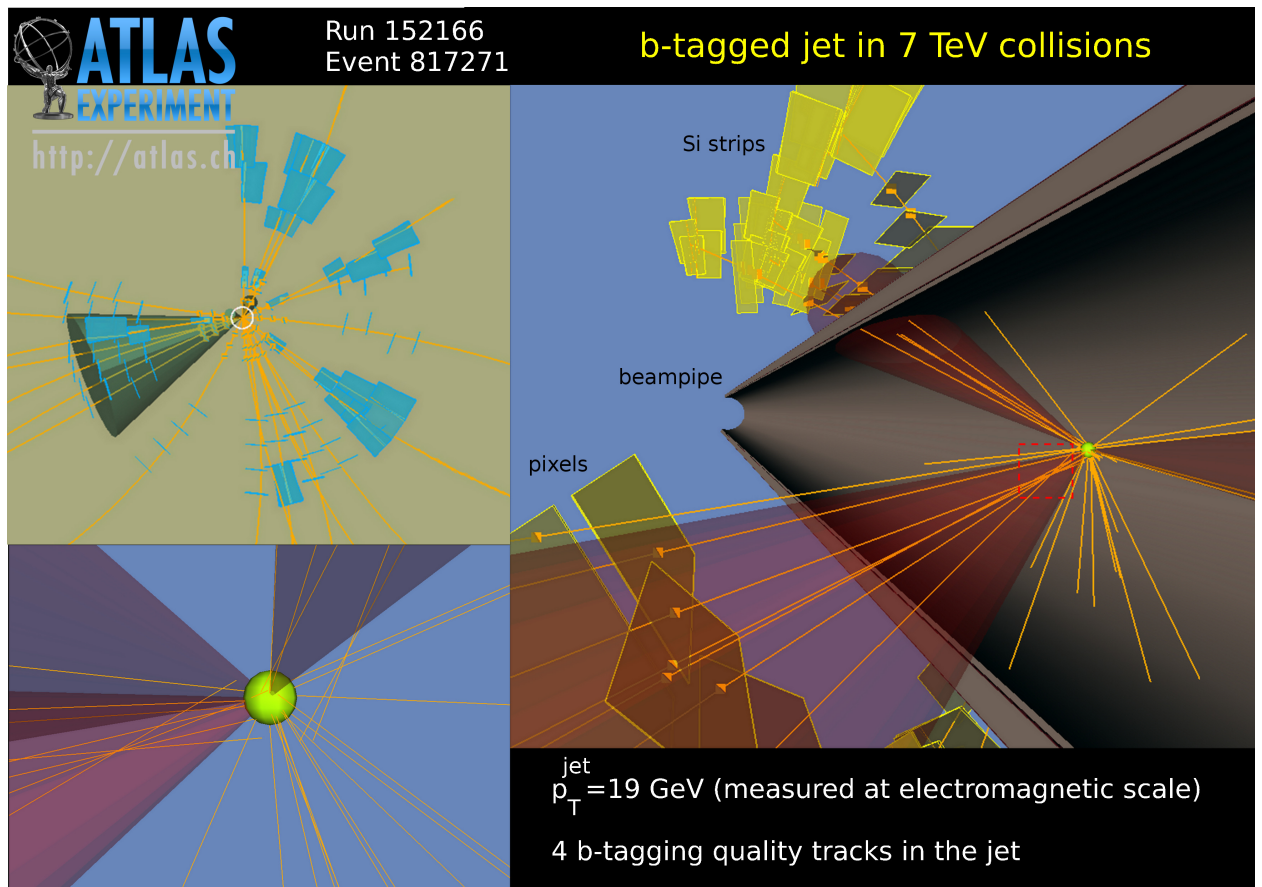


Figure 4.1: Event display for a b-jet, with the secondary vertex shown in the dashed box and primary vertex shown as a round ball [41], ATLAS Experiment ©2011 CERN

760 be b-tagged, but there will also be a relatively high proportion of jets that were not really  
761 b-hadrons that were nevertheless b-tagged as well.

762 In our case, our final state has both a b-jet and a (typically) light quark jet. Our large  
763 backgrounds before b-tagging are backgrounds with many light jets in them. Therefore,  
764 while we remove some of our signal by having a lower b-tagging efficiency, we prefer to  
765 remove proportionally more of our background by choosing an operating point with a high  
766 mis-tagging efficiency. Even though fewer jets are b-tagged, we have more confidence that  
767 the ones we do b-tag are really b-hadrons than if we had chosen a higher b-tagging efficiency.

768 The b-tagger used in this analysis is the JetFitterCombNN b-tagger [42]. This is a  
769 combination of two b-taggers called JetFitter and IP3D. The JetFitter algorithm uses a  
770 Kalman filter [43] to determine the path along which b and c hadrons (from decays inside  
771 the b-jet) and the primary vertex lie, and this determines a track for the b-jet. Additional  
772 discrimination based on the secondary vertex and its uncertainty is done using a likelihood  
773 method. The IP3D b-tagger uses the impact parameter information in all three dimensions  
774 with a likelihood technique to discriminate between the b-jets and lighter jets. An impact  
775 parameter is the shortest distance from the primary vertex (interaction point) to a track.  
776 The transverse impact parameter is a common quantity known as  $d_0$ , and IP3D uses both  
777 transverse and longitudinal ( $z_0$ ) impact parameter information. The JetFitterCombNN ac-  
778 tually uses both JetFitter and IP3D and forms a neural network based using information  
779 from these two algorithms. The output of the neural network forms the JetFitterCombNN  
780 b-tagger. For more information, please see [42].

781 **4.3.1.2 Impact of Different Operation Points on the Analysis**

782 For this analysis, we choose the JetFitterCombNN b-tagger with a threshold of 2.4, so if the  
783 JetFitterCombNN value is  $> 2.4$  the jet is b-tagged. This gives a 57% b-tagging efficiency,  
784 but a very high light quark rejection of about 1000 [42] (or a mis-tagging rate of about  
785 0.1%). This is the lowest b-tagging efficiency (and highest mis-tagging efficiency) operating  
786 point approved for use. In Figure 4.2, the effect on the yields of using different b-tagging  
787 operating points can be seen, where the chosen operating point is shown with a vertical line.  
788 The yields for each process are given for a particular threshold for the JetFitterCombNN  
789 b-tagging variable, as well as scaled versions of the signal divided by the background or the  
790 square root of the background. Both of these are rough indications of signal separation and  
791 analysis performance (but note that they don't include systematic uncertainties). In general  
792 it is clear that while the  $t$ -channel yields go up for a looser operating point, the backgrounds  
793 also increase, at a greater rate. The separation appears to be better for higher thresholds.  
794 Although we lose some of our overall event yield, the background is reduced at a greater rate  
795 than the signal is reduced. For this analysis, we use the highest threshold available, 2.4.

796 **4.4 Taus**

797 Thus far, tau leptons have not really been discussed. This is because we do not specifically  
798 reconstruct or select for taus in this analysis, although of course this is a lepton that could be  
799 involved in the W decay from the top quark. The reason for this is the short tau decay time  
800 and the nature of its decay particles. Unlike the other two leptons, electrons and muons, taus  
801 do not travel very far into the detector before decaying (it has a lifetime of about  $3 \times 10^{-13} s$   
802 and a mass of about 1.8 GeV [11]). Taus may decay into quarks, at which point they look

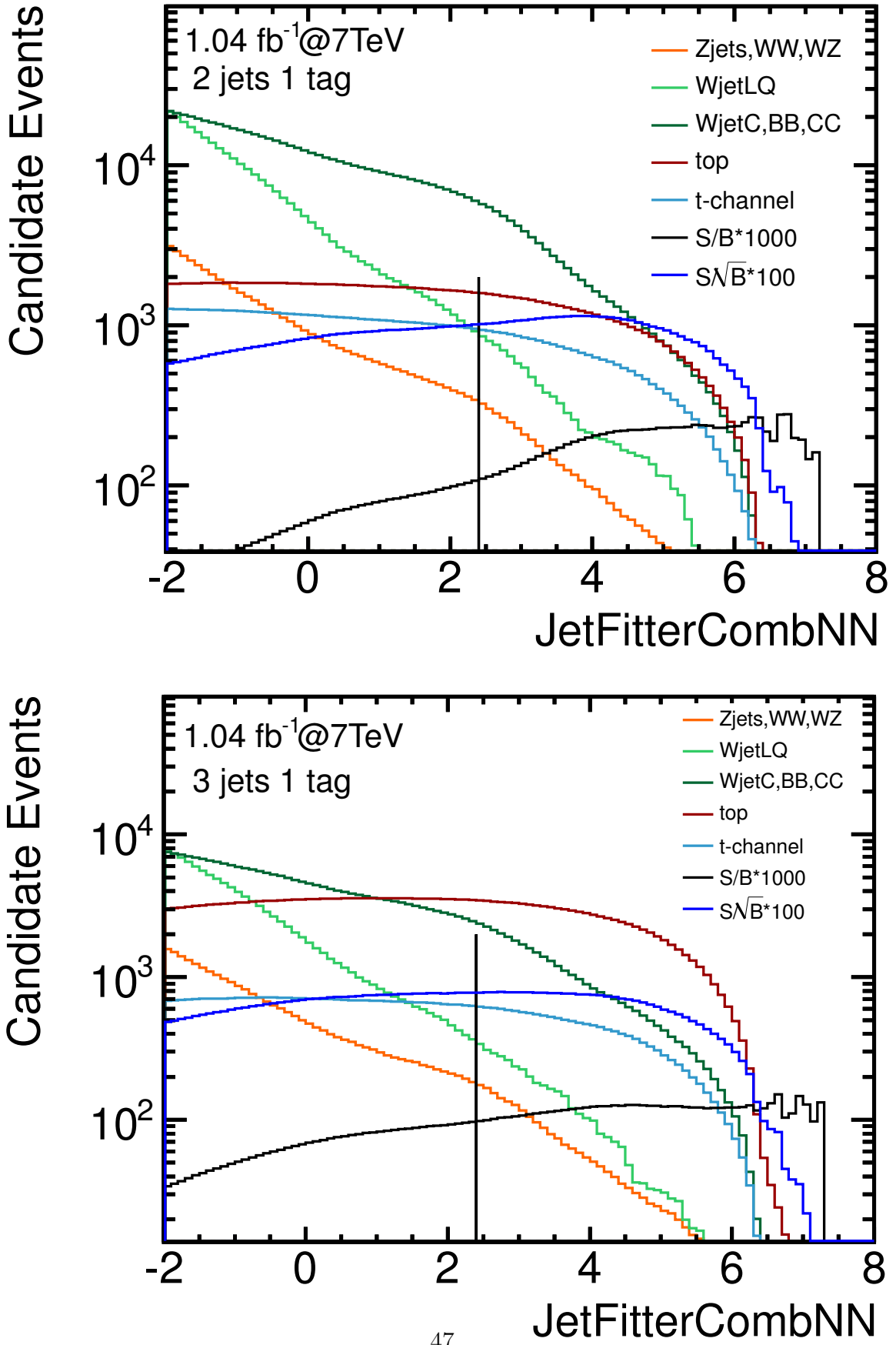


Figure 4.2: Distribution of the yields for the signal (t-channel) and its backgrounds, given a selection on the JetFitterCombNN b-tagging variable at the given x-axis value. Selections at higher x-axis values have lower b-tagging efficiencies but higher mis-tagging efficiencies. The black vertical line shows the threshold used in the analysis.

like a jet (it is theoretically possible to reconstruct a tau like a b-jet, but that is not currently done). It is also possible for the tau to decay to the one of the other two lepton types, plus neutrinos (this happens about 40% of the time). In this case, we incidentally select for these when we select for a muon or electron in our event. However, we don't specifically select or reconstruct a tau. The MC and data both have taus in them and the same selection (and lack of special reconstruction) is applied in both cases, so this is consistent.

## 4.5 Neutrinos and Missing Energy

Although there is a neutrino in the t-channel single-top final state, it has not been heavily discussed. This is because neutrinos interact weakly (and not very often). Thus, we do not try to detect the neutrinos but instead use energy conservation to determine the missing transverse energy, or  $E_T^{\text{miss}}$ , which corresponds to the neutrino's  $p_T$  (or sum of the neutrino  $p_T$  values). If there is more than one neutrino, of course, there is still just one  $E_T^{\text{miss}}$  value. Information about the momentum in the z direction is not preserved as there is no information collected inside of the beam pipe. We can't determine how much energy is missing in that direction from particles that may have traveled only in the z direction and missed the detector. We do have information everywhere else though, so we are able to determine the missing energy in the x and y directions.

The  $E_T^{\text{miss}}$  for ATLAS [44] is calculated from the sum of the calorimeter energy deposits (includes jets, electrons, photons, and |tau decays as well as other deposits) and the energy from reconstructed muons in the x and y directions. The portion of the calorimeter energy deposits in the “other” category are called cell out deposits and jets with  $p_T$  below 20 GeV but above 7 GeV (too low to be considered jets in this analysis) have energy deposits classified

825 as soft jet deposits, rather than standard jet deposits. Cell out deposits are often low energy  
 826 deposits too low to be classified as soft jets or other physics objects. When all of these  
 827 contributions are summed, because the initial collision is in the z direction with no energy in  
 828 the x or y directions, we expect the sum to be 0. The deviation from 0 gives the  $E_T^{\text{miss}}$ .

829 For this analysis, we will want to use the momentum information in the longitudinal or  
 830 z direction, so it is reconstructed from information about the W boson. The single lepton  
 831 and  $E_T^{\text{miss}}$  (which we expect comes from one neutrino in our selected events) correspond  
 832 to a single W boson. The mass of the W is well known, and we take it to be 80.42 GeV,  
 833 consistent with the current Particle Data Group value [11]. From this information, we can  
 834 reconstruct the neutrino momentum in the z direction, using the following equation and  
 835 taking the neutrino and lepton masses to be zero:

$$P^\mu P_\mu = M_W^2 \quad (4.2)$$

836 Here, P is the four-momentum of the lepton and neutrino combination, and  $M_W$  is the W  
 837 mass.

838 After some manipulation, the equation can be rewritten as:

$$l_e^2 \nu_{pT}^2 - (A + B)^2 + (l_e^2 - l_{pz}^2) \nu_{pz}^2 + 2(A + B) l_{pz} \nu_{pz} = 0 \quad (4.3)$$

839 where  $A = \frac{M_W^2}{2}$  and  $B = l_{px} \nu_{px} + l_{py} \nu_{py}$ . Here,  $\nu$  is the neutrino and  $l$  is the lepton  
 840 where  $l_e$  is the lepton energy,  $l_{pz}$  is the lepton longitudinal momentum and  $l_{pT}^2 = l_{px}^2 + l_{py}^2$   
 841 is the lepton transverse momentum. The quantity  $\nu_{pT}$  is just  $E_T^{\text{miss}}$ . This is a quadratic  
 842 equation which can be solved in the usual way for  $\nu_{pz}$ . In the solution, it is possible to have

<sup>843</sup> two results, and in this case we take the smaller of the two values. It is also possible to have  
<sup>844</sup> a negative discriminant ( $1 + (\nu_{pT}^2 l_{pz}^2) < \nu_{pT}^2 l_e^2$ ) and in that case a 0 value is taken. The  
<sup>845</sup>  $E_T^{\text{miss}}$  is primarily used in the analysis until the final cut-based selections are applied, but  
<sup>846</sup> the reconstructed neutrino  $p_z$  is used for quantities such as the reconstructed top mass.

847 **Chapter 5**

848 **Monte Carlo Simulation and**  
849 **Corrections**

850 The Monte Carlo (MC) which simulates events produced by the proton-proton collisions does  
851 not simply appear from equations produced by high energy physics theorists, but instead  
852 must be produced and corrected using computer algorithms. There are two steps to this  
853 process, a generator that produces the general event with quarks, leptons and neutrinos, and  
854 then a showering algorithm that adds extra jets and gluons to these “simple” processes made  
855 by the generator so they resemble more closely what we see in the detector, where higher-  
856 ordered processes are produced. Additionally, after considering the effects of the detector  
857 and producing what is called reconstruction level MC from the truth level MC (which does  
858 not include detector effects), there are still corrections to be made to the particle energies  
859 and the MC events in general to better match the data. In this chapter we discuss the MC  
860 production and these additional MC corrections.

## 861 5.1 MC Generator and Showering

862 The simulation of MC requires a few processing steps. The first is a MC generator which re-  
863 produces the basic Feynman diagrams and the second is a showerer, which adds on additional  
864 particles. In practice it isn't quite so clear-cut. There can be some overlap between what  
865 the showerer and the generator do, and diagram overlap removal procedures are applied in  
866 this case. There may also be some uncovered diagrams depending on the process and choice  
867 of showering algorithm or generator.

868 For this analysis we use PYTHIA [45] for the parton showering for the single-top processes  
869 and HERWIG [46] with JIMMY [47] for the showering for all other processes. The leading  
870 order parton density functions are from CTEQ6L [48]. The generators are more varied.  
871 For our signal we use ACERMC [49], which in our studies uses a procedure to reproduce an  
872 extra, soft b-quark from a incoming gluon more correctly than alternative generators [50].  
873 The  $t\bar{t}$  process is generated using MC@NLO [51] generator, which includes more diagrams  
874 than a standard leading-order generator. The W+jets and Z+jets processes use ALPGEN [52],  
875 as do diboson simulations.

876 Generators and showering algorithms are updated frequently as they are tuned to better  
877 match the data. There is some uncertainty related to our measurement because we know  
878 these probably don't precisely match our data. However, the extensive studies with Tevatron  
879 data have produced generators and showering algorithms that match up well with LHC data,  
880 and the agreement will be discussed in Chapter 8. Additionally, the MC used in this analysis  
881 has the ATLAS tag of "MC10b". It has three simulated bunch trains with 225 ns separation  
882 between the trains. Each train has 36 filled bunches with 50 ns separation between bunches,  
883 the same separation as the data.

884 Finally, it should be noted that the final simulation of the particles going through the  
885 material of the ATLAS detector is done with separate programs [53] based on GEANT4  
886 software [54]. This stage of processing accounts for the specific configuration of the ATLAS  
887 detector, including regions where there may be more or less material. This stage also intro-  
888 duces simulation of the resolution in different portions of the detector. The events are then  
889 reconstructed in the same was as data collected by ATLAS.

## 890 **5.2 Monte Carlo Weighting and Corrections**

891 When the Monte Carlo (MC) is produced, no particular attention is paid to the number of  
892 events generated, other than to be sure there are enough events to allow a sufficient variety  
893 of kinematics (and make the statistical uncertainty low). In order to compare the MC to  
894 the data sample, the MC must be weighted so that the proportions of the different processes  
895 are as we expect and the overall normalization is correct. Here we describe how the event  
896 weighting is done and what weights and corrections are applied.

### 897 **5.2.1 Theoretical cross-section and luminosity weight**

898 The first and perhaps most important weight is the factor that normalizes each process to  
899 its theoretical cross-section and also the whole MC sample to the number of events expected  
900 for the amount of data we have (the integrated luminosity). The factor multiplied onto each  
901 MC event is formed as:

$$\frac{XS \cdot BR \cdot K \cdot L}{N_{MC}} \quad (5.1)$$

where  $XS \cdot BR \cdot K$  is the cross-section times branching ratio times k-factor discussed in Section 2.3.2,  $L$  is the integrated luminosity ( $1035.27\text{ pb}^{-1}$ ) and  $N_{MC}$  is the number of Monte Carlo events. The numerator is simply the number of expected events from Equation 2.4, with the cross-section written out with corrections. The values for  $XS \cdot BR \cdot K$  are given in Table 2.2.

The denominator is the number of MC events, as stated. However, it is important that this include any weights that can affect the overall number of event before analysis selections. These include the pileup weight, discussed next, and negative weights associated with MC generators. Certain MC generators, particularly NLO top-quark process generators like MC@NLO ( $t\bar{t}$ ) or ACERMC (single-top production) give some events negative weights during generation related to interference effects when including NLO processes. This weight is applied when determining the  $N_{MC}$  value, as well as later in the analysis as another event weight.

### 5.2.2 Pile-up weight

The other weight applied to the  $N_{MC}$  value (and all MC events) is the pileup weight, which is related to the number of primary vertices. This is a special weight to adjust the MC to represent the events one expects under certain (data-like) pileup conditions. The pileup conditions may change after a large sample of MC is generated, so this allows more flexibility. The difference between the  $N_{MC}$  in the full MC sample with and without this pileup weight is typically about 1%, so the effect on  $N_{MC}$  is minimal.

The weight itself ranges in value from about 0 to 5, where many events are given weight 0 because they are simulated with pileup conditions exceeding the current data conditions.

924 This of course has an effect on the MC statistical uncertainty, as the MC statistics are  
925 effectively reduced in this case.

### 926 **5.2.3 Lepton scale factor**

927 The lepton scale factor is a factor used to adjust the MC so that the lepton efficiencies  
928 match those found in the data. Scale factors are discrete numbers applied to the MC which  
929 may have some dependency on  $p_T$  or  $\eta$ . There are different scale factors related to the  
930 trigger, reconstruction and identification for each lepton type. These scale factors are all  
931 approximately 1 [32, 34, 55] and have a minimal impact on the analysis.

### 932 **5.2.4 Mis-tagging and b-tagging scale factor**

933 Like the leptons, the b-tagging and mis-tagging efficiencies we see in data are not exactly  
934 the same as MC, so we apply a scale factor to correct the MC. This scale factor is also  
935 typically close to 1 [42, 56]. However, the uncertainties on the b-tagging scale factor are  
936 larger than the others for this analysis, so the b-tagging scale factor has an increased level of  
937 importance. It would be possible to eliminate this scale factor and uncertainty if b-tagging  
938 were not used in the analysis, but the signal separation is not sufficient to do this with the  
939 current data total. For more details on b-tagging and mis-tagging efficiencies in this analysis,  
940 see Section 4.3.1.

### 941 **5.2.5 Energy corrections in the analysis**

942 The energies of different particles are not necessarily quite the same in MC as they are in  
943 data. Although some corrections are applied to the files before they reach analysers, there is

944 some fine-tuning done at the analysis level. We can smear or scale the particle energy, where  
945 smearing involves changing the particle energy using some distribution, like a Gaussian. This  
946 may be done as an uncertainty on the analysis, as is the case with jets, or it may be applied  
947 to the nominal sample, as is the case for leptons.

948 In the case of the leptons, the corrections are chosen to have a better match between  
949 the Z mass peak and width in the data and MC. The electrons have two instances of energy  
950 corrections [32]. The first is a scaling done in the data to correct the energy of the electrons.  
951 This sort of correction is usually done before the analysis level, as for jets, but in this case it  
952 is done afterwards. The second is a smearing, done in MC, to adjust the width of the Z peak  
953 to what we see in data. For the muons, scaling and smearing are both applied to the MC  
954 only. In this case, because tracks are used from the inner detector and muon spectrometer  
955 to form the full muon track, there are separate corrections on the tracks in each region [57].

956 For the jets, the jet energy scale (JES) correction was applied when the jets are formed  
957 and was discussed in Section 4.3. This is a factor that adjusts the jet energy to account for  
958 issues such as dead material or energy leakage. The jet energy resolution (JER) corrections  
959 are done in a separate iteration of the analysis and the difference from the nominal sample  
960 is taken as an uncertainty [39, 58]. The JER adjustment affects the jet energy by adjusting  
961 the value according to a Gaussian distribution, where the Gaussian width depends on the  
962 jet  $p_T$  and  $\eta$  value. There are two major techniques to determine the jet energy resolution,  
963 a di-jet balance method and a bi-sector method. The di-jet balance method uses a two jet  
964 event where the jets are both expected to have a similar  $p_T$  value (back to back jets). The  
965 deviation between the jet  $p_T$  values divided by the sum for each jet can be plotted and fit  
966 with a Gaussian distribution. The bi-sector method is slightly different. It is based on the

967 sum of the  $p_T$  in a 2 jet, back to back event. This  $p_T$  vector is projected into the transverse  
968 plane (transverse to the beam axis) such that the  $\eta$  coordinate in this plane bisects the  
969 difference in the  $\phi$  angles of the two jets. The deviations from nominal (where the sum  
970 of the jet  $p_T$  values is 0) for each transverse plane angle is considered separately and can  
971 be found by fitting gaussian distributions to the  $p_T$  values for each angular component in  
972 different  $p_T$  ranges. The function used to adjust the jet energy in this analysis is based on a  
973 combination of the results of these two techniques.

<sub>974</sub> **Chapter 6**

<sub>975</sub> **Preselection**

<sub>976</sub> In Section 2.3.2 the cross-sections for the signal and background processes were given. It is  
<sub>977</sub> clear that without selections to reduce the background events relative to the signal events,  
<sub>978</sub> single-top  $t$ -channel cannot be distinguished. The haystack is large, and our needles are  
<sub>979</sub> buried and hard to see. The preselection selects events that have single-top  $t$ -channel-like  
<sub>980</sub> kinematic characteristics.

<sub>981</sub> To see how these selections are chosen, we examine the  $t$ -channel final state, shown in  
<sub>982</sub> detail in Figure 6.1. The figure shows that there is at least one b-tagged jet and at least two  
<sub>983</sub> jets (the b-quark from the initial gluon is not always present or detected), with one lepton  
<sub>984</sub> and one neutrino ( $E_T^{\text{miss}}$ ) from the decay of the W. The scenario where a W decays to quarks  
<sub>985</sub> is not selected for, as the final state is then all jets and is very difficult to distinguish from  
<sub>986</sub> the large cross-section multijet background. The multijets cross-section is so large that even  
<sub>987</sub> requiring one lepton, despite the low lepton fake rate in this analysis, still results in a fairly  
<sub>988</sub> large number of multijet events selected.

<sub>989</sub> Requiring a  $t$ -channel final state incidentally helps to reduce the backgrounds, in addition

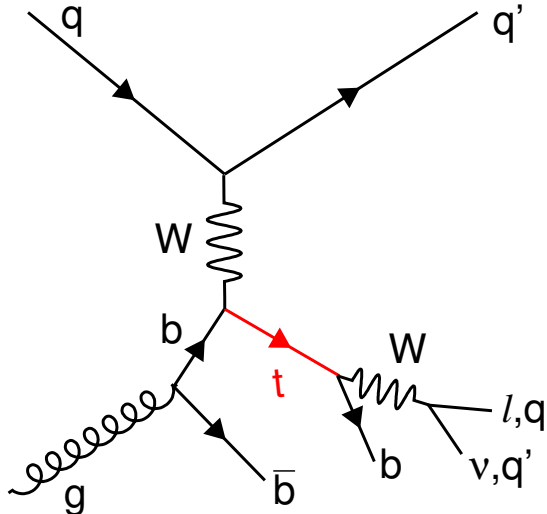


Figure 6.1: Feynman diagram for  $t$ -channel single-top production, showing the final state after the top quark decay.

990 to choosing events that look like our signal. Rejecting events with less than 2 or more than  
 991 3 jets helps to reduce  $W+jets$  and  $t\bar{t}$ , respectively, as these processes tend to have fewer or  
 992 more jets than the signal.

993 The preselection used in this analysis in detail is given below. The selection without the  
 994 b-tagged jet number requirement is called the pretag selection:

- 995 • The event must have a quality primary vertex (has at least 5 tracks)
- 996 • Exactly one, triggered lepton (muon or electron), matched to a reconstructed lepton  
 997 object
- 998 • The leptons must have  $p_T > 25 \text{ GeV}$  and muons must also have  $p_T < 150 \text{ GeV}$
- 999 • There must be  $E_T^{\text{miss}} > 25 \text{ GeV}$
- 1000 • Two or three jets, with a one jet selection used for a sideband region
- 1001 • The jets must not be “bad”

1002      • LAr quality requirements related to the LAr hole must be met

1003      • Data events with LAr bursts (noise) are removed

1004      • Triangular cut of  $E_T^{\text{miss}} + W_T > 60 \text{ GeV}$

1005      • At least one of the jets must be b-tagged

1006      The primary vertex requirement helps to reduce contamination from secondary vertices

1007      or events where an extra pileup interaction (often multijet) vertex might be confused for the

1008      one we are interested in. The lepton requirement helps to reduce multijet events, which do

1009      not have a real lepton. The trigger requirement specifically requires the EF\_mu18 trigger

1010      for the one muon selection and EF\_e20\_medium trigger for the one electron selection. The

1011      trigger matching ensures that the lepton in the analysis matches with a trigger-level object.

1012      This selection has a small effect on the analysis. Due to an issue with the MC, the muon

1013      trigger matching was not applied for the muon channel (although the trigger itself was still

1014      applied). The  $p_T$  requirement for the leptons is 25 GeV partly to be sufficiently away from

1015      the trigger thresholds of 18 and 20 GeV, to reduce the related uncertainty. The upper

1016       $p_T$  threshold is applied due to low statistics when determining the muon scale factors in this

1017      region (the impact on the analysis from this selection is very small). The  $E_T^{\text{miss}}$  selection

1018      has a threshold similar to the lepton to reduce multijet events faking a small amount of

1019       $E_T^{\text{miss}}$ . The lower  $p_T$  thresholds for the particles help to reduce the multijet and W+jets

1020      backgrounds, which often have lower  $p_T$  particles.

1021      The analysis requires 2 or 3 jets. This chooses a final state that looks like the signal, but

1022      also helps to reduce W+jets and  $t\bar{t}$ , respectively, as these processes tend to have fewer or

1023      more jets than the signal. The events must satisfy several selections to remove events which

1024 contain bad jets. These are jets that arise due to cosmic rays, detector problems, or beam  
1025 issues and the whole event is removed if it includes a bad jet. For completeness, the cuts  
1026 are as follows [59, 60]. There is a bad jet if the energy fraction in the HEC is  $> 0.5$  and  
1027 the fraction of energy corresponding to hadronic end-cap calorimeter (HEC) cells with a cell  
1028 Q-factor (related to the energy pulse shape measured versus expected) greater than 4000 is  
1029  $> 0.5$  (corresponds to HEC spikes; hardware issues). The event is rejected if the jet's energy  
1030 fraction in the electromagnetic calorimeter is  $> 0.95$ , the fraction of energy corresponding  
1031 to LAr cells with a cell Q-factor greater than 4000 is  $> 0.8$ , and  $|\eta| < 2.8$  for the jet (EM  
1032 calorimeter noise issues). Finally, the event is rejected if the jet timing is  $> 25\text{ ns}$  (indicates  
1033 out-of-time jets, from a cosmic ray for instance). The timing is the deviation of the event  
1034 time from the time of energy deposition for the detector cells related to the jet, weighted by  
1035 their energy squared.

1036 Of the remaining four selections, there are two selections related to the LAr. The first  
1037 removes events where jet reconstruction is affected by the LAr hole. The second removes  
1038 events with noise bursts related to the LAr. Finally, we apply a triangular cut which reduces  
1039 the multijet background and, last, we require at least one jet to be b-tagged.

<sub>1040</sub> **Chapter 7**

<sub>1041</sub> **Modeling the Signal and the  
1042 Backgrounds**

<sub>1043</sub> In order to study single-top  $t$ -channel production, we need to know what the standard model  
<sub>1044</sub> version of this should look like in our data. This is actually quite a complicated task, to  
<sub>1045</sub> simulate all of the standard model processes and also how these different particles interact  
<sub>1046</sub> with the detector. The Monte Carlo (MC) techniques that were used in this analysis to  
<sub>1047</sub> simulate “data” were discussed in Chapter 5. Here, we discuss the data-based estimates  
<sub>1048</sub> we use for the multijets normalization and kinematic shapes, as well as how the W+jets  
<sub>1049</sub> normalization and heavy flavor fractions are obtained from data.

<sub>1050</sub> **7.1 Multijet Estimation**

<sub>1051</sub> Multijets (sometimes colloquially referred to as QCD) are difficult to simulate in quantities  
<sub>1052</sub> necessary to be useful in analyses. This is a process with a very large cross-section and a  
<sub>1053</sub> very, very small proportion of events left after cuts, relative to the starting yield. It just

1054 isn't feasible to generate MC for this background.

1055 We do, however, have a lot of multijets in our rejected data sample, in our off-signal  
1056 region. We can make use of this to select a relatively pure sample of multijet events which is  
1057 used for both kinematic shapes and to determine the normalization (i.e. how many multijet  
1058 events are actually in the preselection sample). There are several ways to form such a  
1059 region. For instance, one could require the leptons to not be tight or not be isolated, keep  
1060 the other selections and cuts the same, and end up with an orthogonal multijets sample.  
1061 This particular method, however, suffers from too much contamination from W+jets events.

1062 The method chosen for this analysis is the “jet-electron” method. In this method, the  
1063 usual electron trigger is replaced by a jet trigger. Correspondingly the data stream is replaced  
1064 by the JetTauEtmiss stream (the main analysis uses muon and electron streams). The  
1065 triggered jet must also have a high EM fraction, so most of the energy is deposited in the EM  
1066 calorimeter, and at least 4 tracks, to avoid including photon conversions. All other selections  
1067 and cuts are unchanged. This sample is used to determine the kinematic shapes. Because  
1068 of the low statistics due to increasing trigger thresholds as the data taking has progressed,  
1069 the shapes before the b-tagging selection are used for distributions after b-tagging as well.  
1070 Checks have been performed which show that the shapes are indeed similar.

1071 The overall normalization is found by fitting to a kinematic distribution. The  $E_T^{\text{miss}}$  dis-  
1072 tribution is usually used, although the transverse W mass has been used as a cross-check  
1073 and to help determine the uncertainty on our multijets estimate, which is 50%. The yields  
1074 are given in Table 7.1.

Jet bin	Pretag events		Tagged events	
	e channel	$\mu$ channel	e channel	$\mu$ channel
1-jet	$24000 \pm 12000$	$12000 \pm 6000$	$320 \pm 160$	$290 \pm 145$
2-jet	$15000 \pm 7500$	$6800 \pm 3400$	$710 \pm 355$	$440 \pm 220$
3-jet	$6000 \pm 3000$	$1700 \pm 850$	$580 \pm 290$	$270 \pm 135$

Table 7.1: Estimate of multijet yields for the pretag and preselection samples for different number of jet selections, separated by lepton type.

## 1075 7.2 W+jets Estimation

1076 The W+jets process is a large background for this analysis after preselection and is not  
 1077 especially well understood in the MC, particularly the heavy flavor fractions. For this reason,  
 1078 we use the data to determine the overall W+jets normalization as well as the normalization  
 1079 of the separate flavor W+jet productions. These are W+light jets, W+cjets, W+c $\bar{c}$  jets and  
 1080 W+b $\bar{b}$  jets. The last two are combined together for the purposes of this normalization.

1081 The method used here is called the “cut and count” method. This method was first  
 1082 developed during the ATLAS  $t\bar{t}$  rediscovery [61], although not used due to low statistics, and  
 1083 has been used in each data-based single-top note [62, 8, 9]. The general idea is to form a  
 1084 series of equations involving off-signal regions which can then be solved for the scale factors  
 1085 of interest (to scale each W+jets MC sample). The scaling is done based on the number of  
 1086 jets and the W+jets MC flavor, which is based on what type of quark the W+jets event is  
 1087 associated with, light (lq), c, c $\bar{c}$  or b $\bar{b}$ .

1088 First, the overall W+jets normalization is determined as a function of the number of  
 1089 jets in the event using the sample before b-tagging is applied, the pretag sample. The scale  
 1090 factor is determined as:

$$\frac{N_{W+jets,data}}{N_{W+jets,MC}} = \frac{N_{data} - N_{multijets} - N_{Non-W+jets,MC}}{N_{W+jets,MC}} \quad (7.1)$$

1091 The overall normalization scale factors are given in Table 7.2.

W+1jet	W+2jets	W+3jets
$0.966 \pm 0.001$	$0.914 \pm 0.002$	$0.879 \pm 0.004$

Table 7.2: Scale factors for the overall normalization factor used to normalize MC to data for W+jets. The uncertainties are statistical only.

1092 The normalization of the individual flavor scale factors involves additional equations.

1093 We use three different off-signal regions for this: 2 jet pretag, 1 jet 1 b-tag, and 2 jets 1  
1094 b-tag. This last region contains part of the final analysis signal region, so that this portion  
1095 is subtracted off before doing the estimate of the W+jets scale factor. It is also possible to  
1096 use the 1 jet pretag bin and include a different combination of regions, so that this equation  
1097 will also be shown, although it is not used.

1098 We will solve a series of equations for the flavor fractions,  $F_{b\bar{b}2}$ ,  $F_{c2}$ , and  $F_{lq2}$ , where  
1099  $F_{c\bar{c}2}$  and  $F_{b\bar{b}2}$  are assumed to be the same (one scale factor for both processes). These can  
1100 then be converted into different bins using MC assumptions. These flavor fractions we solve  
1101 for are all from the 2 jet pretag selections and will be propagated later on into other regions.  
1102  $F_{c2}$  for example is, where W+jets refers to all W+jets flavors combined:

$$F_{c2} = \frac{N_{c2}^{pretag}}{N_{W+jets2}^{pretag}} \quad (7.2)$$

1103 Here, N is the number of events, 2 indicates two jets, and the letters refer to the different  
1104 flavors (lq is light quarks). W+jets refers to all W+jets MC events.

1105 The set of four equations are written as follows, where in this analysis we make use of the

1106 last three. The equations state that the total data minus background (i.e. non-W+jets) is  
 1107 the same as the sum of the MC W+jet samples separated by flavor. In these equations, the  
 1108 superscripts p and t mean pretag and b-tagged samples. All other quantities use MC pretag  
 1109 values except the b-tagging probabilities P, which use both MC tag and pretag information,  
 1110 and N's are from the data minus the non W+jets MC yields and multijets estimate. Specific  
 1111 definitions of quantities follow these equations:

$$\begin{aligned}
 N_1^p &= N_1^p \cdot (k_{b\bar{b}2to1} \cdot F_{b\bar{b}2} + k_{c\bar{c}tob\bar{b}} \cdot k_{b\bar{b}2to1} \cdot F_{b\bar{b}2} + k_{c2to1} \cdot F_{c2} + k_{lq2to1} \cdot F_{lq2}) \\
 N_2^p &= N_2^p \cdot (F_{b\bar{b}2} + k_{c\bar{c}tob\bar{b}} \cdot F_{b\bar{b}2} + F_{c2} + F_{lq2}) \\
 N_1^t &= N_1^p \cdot (P_{b\bar{b}1} \cdot k_{b\bar{b}2to1} \cdot F_{b\bar{b}2} + k_{c\bar{c}tob\bar{b}} \cdot P_{b\bar{b}1} \cdot k_{b\bar{b}2to1} \cdot F_{b\bar{b}2} \\
 &\quad + P_{c1} \cdot k_{c2to1} \cdot F_{c2} + P_{lq1} \cdot k_{lq2to1} \cdot F_{lq2}) \\
 N_2^t &= N_2^p \cdot (P_{b\bar{b}2} \cdot F_{b\bar{b}2} + k_{c\bar{c}tob\bar{b}} \cdot P_{b\bar{b}2} \cdot F_{b\bar{b}2} + P_{c2} \cdot F_{c2} + P_{lq2} \cdot F_{lq2})
 \end{aligned}$$

1112 In the equations above, the P's are the b-tagging probability where the number of jets  
 1113 and jet flavor are specified by the subscripts. They are used to convert the b-tagged (tag)  
 1114 sample flavor fractions (F) to the pretag versions we are solving for. For instance,

$$P_{b\bar{b},1} = \frac{N_{w\bar{b},1jet,tag}}{N_{w\bar{b},1jet,pretag}} \quad (7.3)$$

1115 which means that

$$N_{c2}^{tag} = N_{c2}^{pretag} \cdot P_{c2} \cdot F_{c2} \quad (7.4)$$

1116 The k's in the equations are the ratio of yields in different number-of-jet bins or, in one

<sub>1117</sub> case( $k_{c\bar{c}tob\bar{b}}$ ), the flavor, and are always determined using the pretag sample. They are  
<sub>1118</sub> conversion factors. For example,

$$k_{b\bar{b}2to1} = \frac{N_{wbb,1jet,pretag}}{N_{wbb,2jet,pretag}} \quad \text{and} \quad k_{b\bar{b}tocc\bar{c}} = \frac{N_{wc\bar{c},1jet,pretag}}{N_{wbb,1jet,pretag}} \quad (7.5)$$

<sub>1119</sub> Finally, the N's in the equation represent the number of data minus background (where  
<sub>1120</sub> background is non-W+jets MC and multijets) events for the given bin and sample specified  
<sub>1121</sub> by p1 for pretag, 1 jet bin; p2 for pretag 2 jet bin; t1 for 1 b-tag (preselection) 1 jet bin; and  
<sub>1122</sub> t2 for 1 b-tag (preselection) 2 jet bin.

<sub>1123</sub> Note that the N's are the only data based quantities in the flavor fraction determination.  
<sub>1124</sub> The P's and k's are taken from the values in Monte Carlo. Thus, there are three (or four)  
<sub>1125</sub> equations and three unknowns, meaning a solution may be found with simple algebra. These  
<sub>1126</sub> F's are then propagated into other number of jet bins. When these values are combined with  
<sub>1127</sub> the overall W+jets normalization factors discussed earlier, the final W+jets scale factors for  
<sub>1128</sub> this analysis are obtained (WSF).

<sub>1129</sub> The equation used to form the scale factors for the two jet bin (which doesn't involve  
<sub>1130</sub> extra propagation) is given below in Equation 7.6. The F/F portion is the flavor fraction  
<sub>1131</sub> scaling and the N/N portion at the end of the equation is the overall W+jets normalization.  
<sub>1132</sub> N's are data minus the non W+jets MC yields and multijets estimate as before, unless  
<sub>1133</sub> specified to be the MC W+jets estimate. All quantities are pretag:

$$WSF_{c,2} = \frac{N_{c,2}}{N_{c,2}^{MC}} = \frac{F_{c,2} \cdot N_{Wjets,2}}{F_{c,2}^{MC} \cdot N_{Wjets,2}^{MC}} \quad (7.6)$$

<sub>1134</sub> To find the scale factors in other bins, the three jet bin in particular, we use the following

<sub>1135</sub> formula (Equation 7.7), shown here for the 3 jet c scale factor, where all quantities are pretag:

$$WSF_{c,3} = \frac{F_{c,2} \cdot N_{Wjets,3}}{F_{c,2}^{MC} \cdot (N_{b\bar{b},3}^{MC} + N_{c\bar{c},3}^{MC} + N_{c,3}^{MC} \cdot WSF_{c,2} + N_{lq,3}^{MC})} \quad (7.7)$$

<sub>1136</sub> The final scale factor (WSF) values are shown in Table 7.3 for the various number of jet  
<sub>1137</sub> bins and W+jets flavor types. These are the values used to adjust the W+jets normalization  
<sub>1138</sub> in the analysis.

Jet Bin	$WSF_{b\bar{b}}$	$WSF_{light}$	$WSF_c$
$W+1jet$	$1.361 \pm 0.090 \pm 1.066$	$0.908 \pm 0.004 \pm 0.270$	$1.273 \pm 0.040 \pm 0.449$
$W+2jet$	$1.252 \pm 0.090 \pm 0.864$	$0.835 \pm 0.004 \pm 0.230$	$1.172 \pm 0.004 \pm 0.302$
$W+3jet$	$1.182 \pm 0.090 \pm 0.854$	$0.788 \pm 0.004 \pm 0.369$	$1.106 \pm 0.004 \pm 0.443$

Table 7.3: Correction factor WSF for each  $W+jets$  flavor for the muon and electron samples combined, with statistical (first) and systematic (second) uncertainties.

<sub>1139</sub> **Chapter 8**

<sub>1140</sub> **Event Yields and Discriminating**

<sub>1141</sub> **Variables**

<sub>1142</sub> In the full data set, it is impossible to distinguish the signal from the immense background.

<sub>1143</sub> To make an accurate measurement of the cross-section, we need to apply more selections that

<sub>1144</sub> will reduce the background and isolate the single-top  $t$ -channel signal. In this chapter we dis-

<sub>1145</sub> cuss the yields after the preselection and the effect of the b-tagging preselection requirement.

<sub>1146</sub> We will also outline the variables considered to achieve additional signal discrimination and

<sub>1147</sub> demonstrate the agreement between data and MC using the preselection with and without

<sub>1148</sub> the b-tagging requirement.

<sub>1149</sub> **8.1 Event Yields**

<sub>1150</sub> After applying the preselection, data-based normalization and models for multijets and

<sub>1151</sub> W+jets, as well as additional event corrections, we obtain the initial analysis yields

<sub>1152</sub> which may be compared to data. The pretag yields by process are as given in Table 8.1

<sub>1153</sub> and the yields after preselection (i.e. including b-tagging) are given in Table 8.2. The signal  
<sub>1154</sub> divided by background (S/B) is only about 0.1 after the preselection, but improved by about  
<sub>1155</sub> a factor of 10 from the pretag yields, showing the importance of the b-tagging selection. The  
<sub>1156</sub> yields are given in the different analysis channels which will be considered in Section 9.1,  
<sub>1157</sub> based on the number of jets and charge of the lepton.

	2 Jets		3 Jets	
	Lepton +	Lepton -	Lepton +	Lepton -
<i>t</i> -channel	1230	678	816	455
<i>t</i> <bar>t, Other top</bar>	1730	1680	3510	3510
<i>W</i> +light jets	103000	64800	26600	16000
<i>W</i> +heavy flavor jets	35400	30800	10800	8920
<i>Z</i> +jets, Diboson	10200	9580	3560	3500
Multijets (e)	6960	7930	3160	2830
Multijets ( $\mu$ )	3300	3500	800	860
TOTAL Exp	162000	119000	49200	36100
S/B	0.01	0.01	0.02	0.01
DATA	162148	117010	46830	34925

Table 8.1: Event yields for the two-jets and three-jets tag positive and negative lepton-charge channels after the preselection, except for the b-tagging selection. The multijets and *W*+jets backgrounds are normalized to the data, all other samples are normalized to theory cross-sections. Lepton types (muon and electron) are combined unless otherwise noted.

## <sub>1158</sub> 8.2 Discriminating Variables

<sub>1159</sub> Because the signal divided by the background is only 0.1 after applying the preselection, we  
<sub>1160</sub> would like to apply more selections that will reduce the background and isolate the single-top  
<sub>1161</sub> *t*-channel signal. There are many variables considered in this analysis, about 80 in total. We  
<sub>1162</sub> consider the  $p_T$  and  $\eta$  of all of the particles, as well as differences in the  $\eta$ ,  $\phi$  and  $R$  quantities.  
<sub>1163</sub> For example, we consider the  $|\Delta\eta(b, j_u)|$ , the  $\Delta R$  between the leading untagged jet and the  
<sub>1164</sub> b-tagged jet. We also consider the angles between various particles, as well as the invariant

	2 Jets		3 Jets	
	Lepton +	Lepton -	Lepton +	Lepton -
$t$ -channel	611	327	399	221
$t\bar{t}$ , Other top	805	781	1720	1730
$W$ +light jets	544	308	183	154
$W$ +heavy flavor jets	3100	2630	1350	1020
$Z$ +jets, Diboson	175	150	92	83
Multijets (e)	365	342	279	295
Multijets ( $\mu$ )	221	215	139	135
TOTAL Exp	5820	4750	4160	3630
S/B	0.12	0.07	0.11	0.06
DATA	5912	4701	4016	3491

Table 8.2: Event yields for the two-jets and three-jets tag positive and negative lepton-charge channels after the preselection. The multijets and  $W$ +jets backgrounds are normalized to the data, all other samples are normalized to theory cross-sections. Lepton types (muon and electron) are combined unless otherwise noted.

mass of several particle combinations, including all of the jets in the event ( $M(\text{AllJets})$ )  
 and the b-quark, lepton and neutrino ( $M_{top}(l\nu b)$ ). This last is the reconstructed top quark  
 mass (note that we use the reconstructed neutrino Z momentum, see Section 4.5). We also  
 consider the transverse mass of the W and the sum of the  $p_T$  of all the particles in the event  
 (using  $E_T^{\text{miss}}$  for the neutrino), called  $H_T$ . Finally, we use the number of jets, the number  
 of b-tagged jets, and the charge of the lepton to define analysis channels. The lepton type,  
 muon or electron, is not used for this purpose, so analysis channels contain a combination  
 of the lepton types.

The variables used in this analysis are shown in the following figures. The first set of  
 figures shows the distributions using the preselection requirements except b-tagging (pretag)  
 for 2 jets (Figure 8.1) and for 3 jets (Figure 8.2). This first set includes a band showing the  
 jet energy scale uncertainty. In these figures and others, “other top” refers to the  $s$ -channel  
 and  $Wt$  single-top contributions. The  $W$ +jets heavy flavor includes  $Wc$ ,  $Wc\bar{c}$ , and  $Wb\bar{b}$  jets

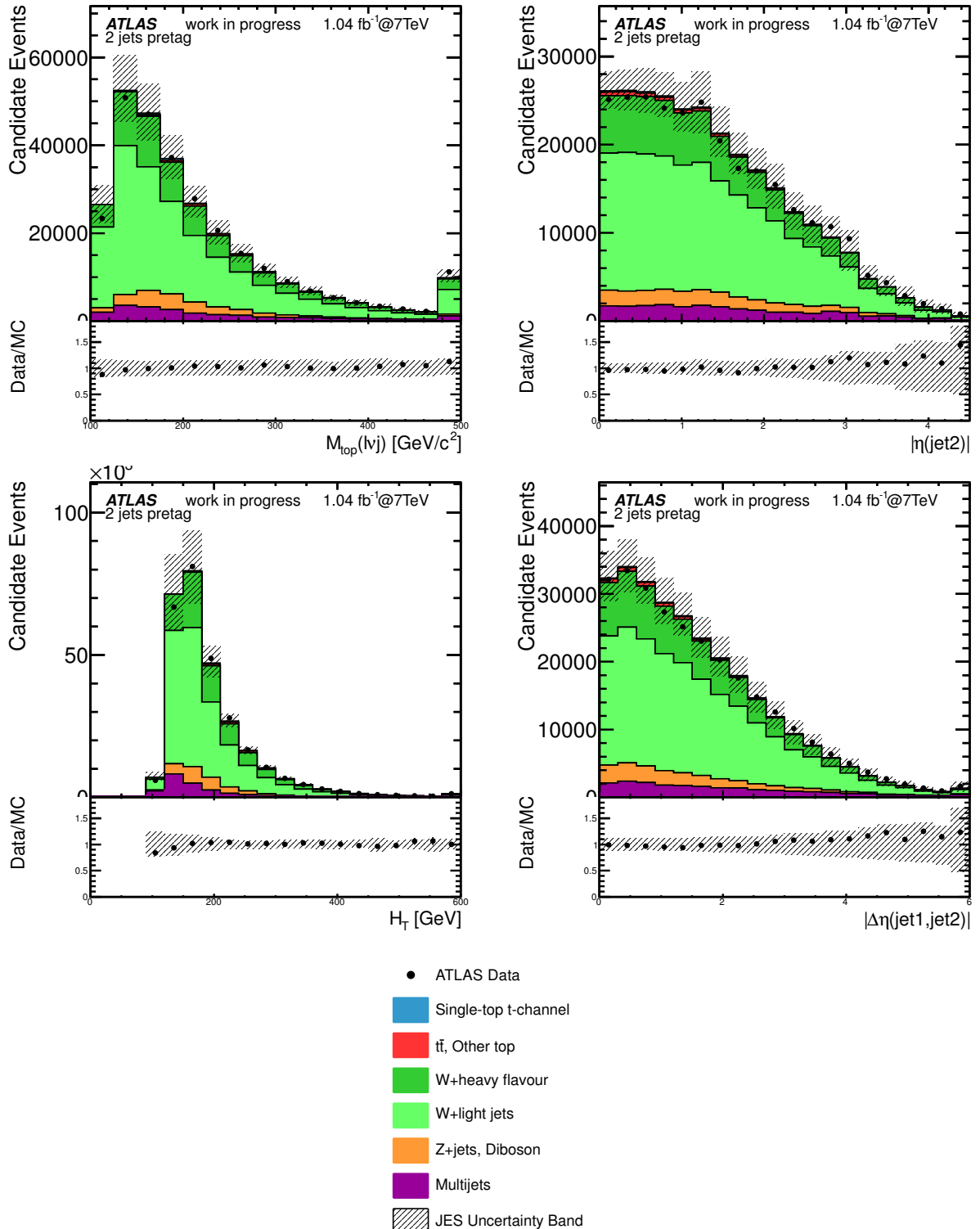


Figure 8.1: Discriminating variables for the pretag sample for two-jets events. Hatched bands show the jet energy scale uncertainty. The last bin contains the sum of the events in that bin or higher. Other top refers to the  $s$ -channel and  $Wt$  single-top contributions.

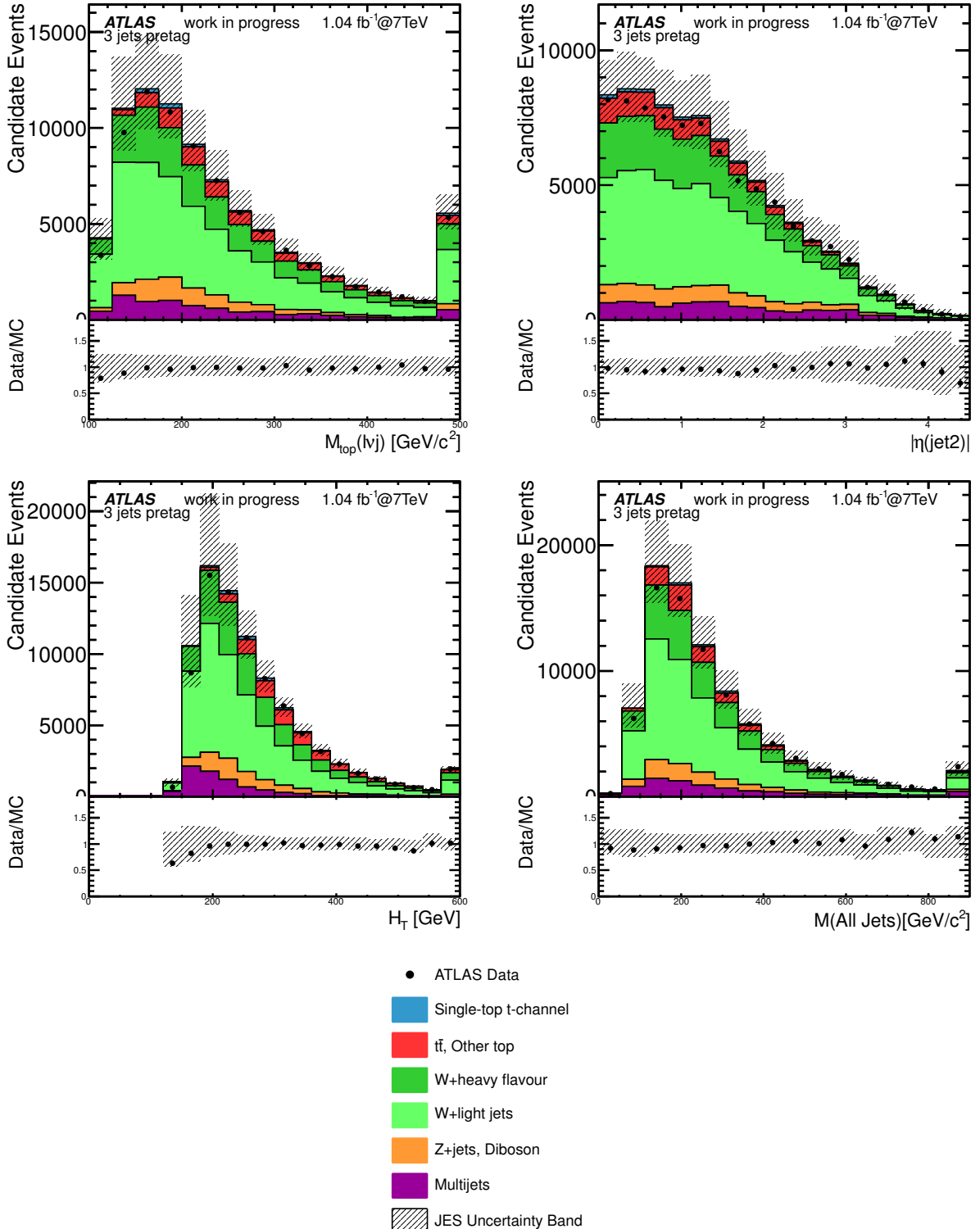


Figure 8.2: Discriminating variables for the pretag sample for three-jets events. Hatched bands show the jet energy scale uncertainty. The last bin contains the sum of the events in that bin or higher. Other top refers to the  $s$ -channel and  $Wt$  single-top contributions.

<sub>1178</sub> Figures 8.3 and 8.4 show the same distributions after the requirement of exactly one  
<sub>1179</sub>  $b$ -tagged jet in the event for 2 or 3 jet samples.

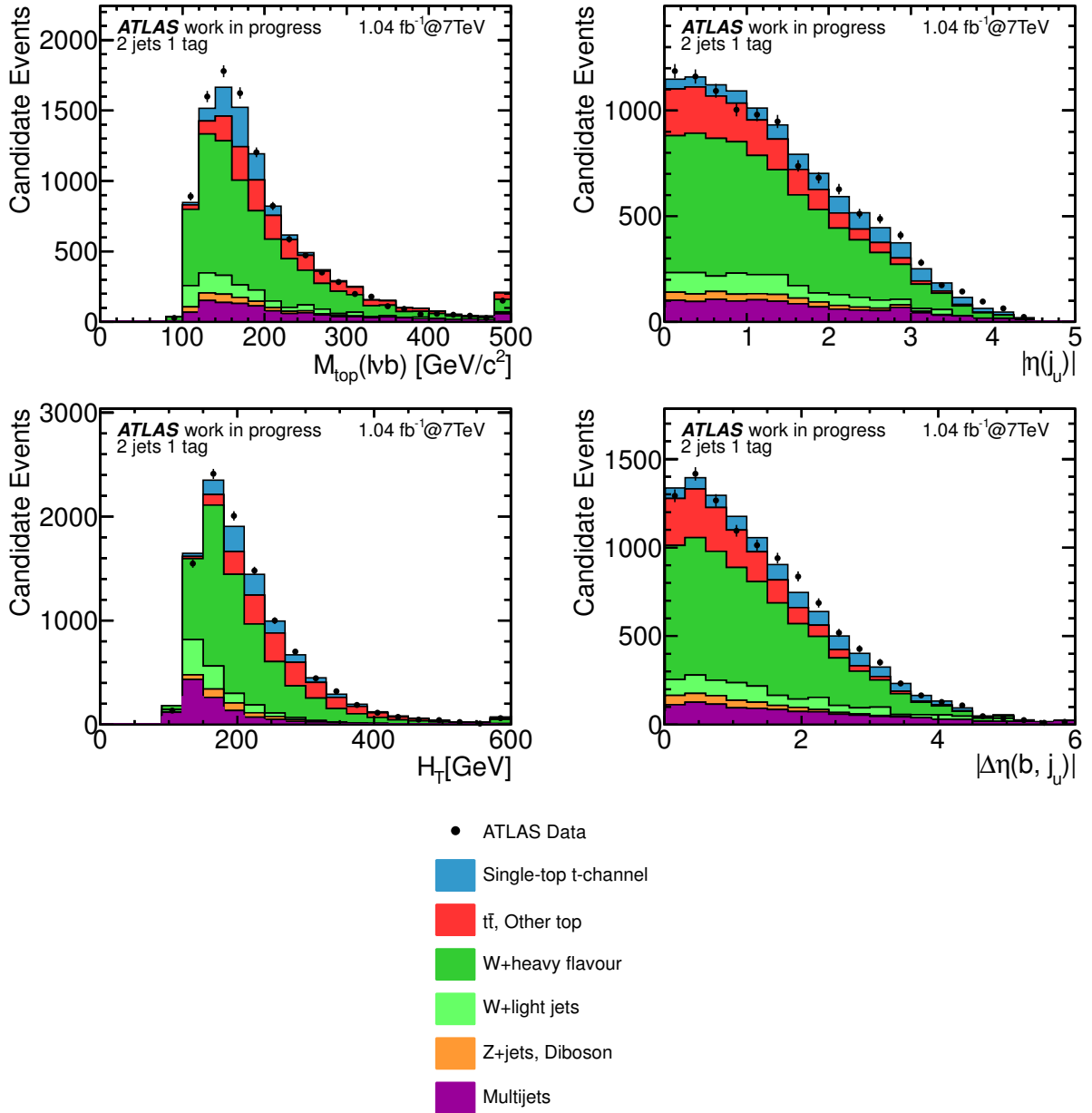


Figure 8.3: Discriminating variables for the preselection sample for two-jets events. The last bin contains the sum of the events in that bin or higher. Other top refers to the  $s$ -channel and  $Wt$  single-top contributions.

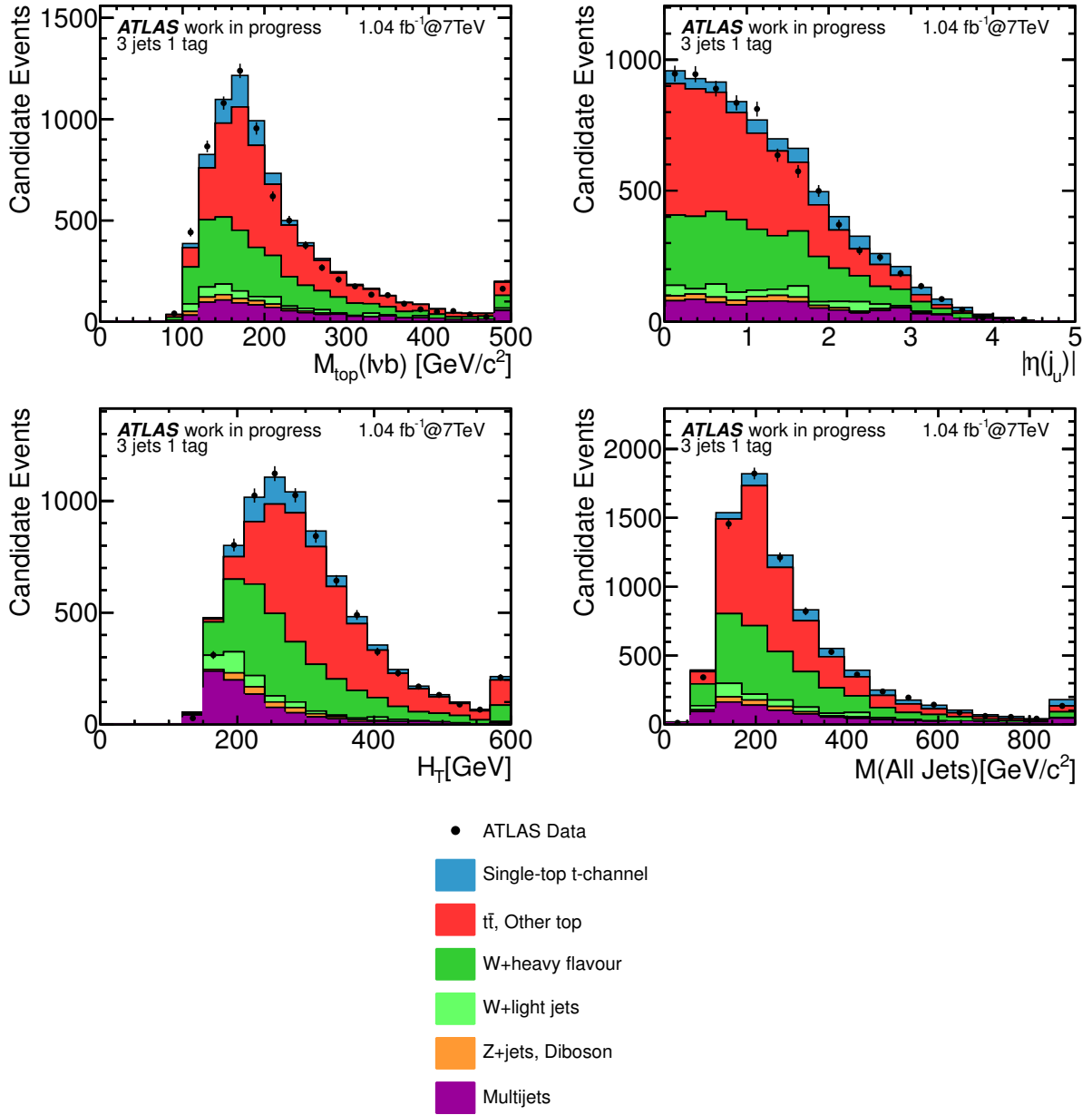


Figure 8.4: Discriminating variables for the preselection sample for three-jets events. The last bin contains the sum of the events in that bin or higher. Other top refers to the  $s$ -channel and  $Wt$  single-top contributions.

<sub>1180</sub> **Chapter 9**

<sub>1181</sub> **The Cut-Based Analysis**

<sub>1182</sub> The separation of the  $t$ -channel single-top signal from its backgrounds has been performed  
<sub>1183</sub> with a cut-based analysis. This analysis type typically requires a limited number of selections  
<sub>1184</sub> using a limited number of variables, so the selections that are made are strongly discrimi-  
<sub>1185</sub> nating. One advantage of a cut-based analysis is that it is relatively easy to interpret. In  
<sub>1186</sub> this chapter, we discuss the kinematic regions (channels) chosen for this analysis as well as  
<sub>1187</sub> the selections and how they were determined.

<sub>1188</sub> **9.1 Analysis Channels**

<sub>1189</sub> The analysis channels are chosen to be orthogonal (non-overlapping) kinematic regions. We  
<sub>1190</sub> choose quantities for this that are discrete, specifically the jet number and lepton charge.  
<sub>1191</sub> The background composition is closely related to the number of jets in the event. The  
<sub>1192</sub>  $W+jets$  and multijet backgrounds tend to have lower numbers of jets in the event while the  
<sub>1193</sub>  $t\bar{t}$  background usually has four jets (although of course can also have less or more based on  
<sub>1194</sub> the  $W$  decay, and jet reconstruction and  $p_T$ ). The "standard"  $t$ -channel single-top diagram

<sub>1195</sub> has 2 or possibly 3 jets, so it is natural to look in these channels.

<sub>1196</sub> We also consider the lepton charge when creating analysis channels. The LHC collides  
<sub>1197</sub> protons with protons and because protons are composed of two up and one down valence  
<sub>1198</sub> quarks, there is an excess of positively charged up valence quarks. This translates into an  
<sub>1199</sub> excess of positively charged leptons in the case of the  $t$ -channel single-top diagram, which  
<sub>1200</sub> usually has a valence quark in the initial state. Processes like  $W+jets$  also have some  
<sub>1201</sub> charge asymmetry, but others like  $t\bar{t}$  form primarily from gluons in the initial state and do  
<sub>1202</sub> not. Thus, this sort of channel separation helps to reduce the background in the positively  
<sub>1203</sub> charged lepton channel in particular and changes the background composition.

## <sub>1204</sub> **9.2 Analysis Method**

<sub>1205</sub> Performing the cut-based analysis includes determining the choice of selections to be applied  
<sub>1206</sub> to each analysis channel. Each channel has its selections optimized separately, although  
<sub>1207</sub> sometimes the final selections are the same for certain channels.

### <sub>1208</sub> **9.2.1 Selection Optimization**

<sub>1209</sub> The optimization to determine the analysis selections for a given channel uses a significance  
<sub>1210</sub> criterion (this has not been used to determine a significance of the result, only to optimize the  
<sub>1211</sub> selections). The analysis itself is a cross-section measurement analysis, so one might expect  
<sub>1212</sub> that a cross-section criterion would be used in the optimization. However, expected cross-  
<sub>1213</sub> sections were calculated for several cut sequences and the ones with the lowest cross-section  
<sub>1214</sub> uncertainties also tended to have the lowest significances.

<sub>1215</sub> The significance used includes the background uncertainties, and the calculation is very

1216 fast, which is important given the number of variables and selection thresholds that are  
 1217 considered. The method is a binomial significance method, also called Zbi, and is documented  
 1218 elsewhere [63]. This method is chosen over other common criteria, such as  $\frac{S}{\sqrt{B}}$ , because it is  
 1219 a real significance and includes systematic uncertainties. The way it is implemented in this  
 1220 analysis is as suggested in the Zbi documentation [63], where  $\sigma_b$  is the background systematic  
 1221 uncertainties,  $N_b$  is the background yield and  $Non$  is the signal plus background yield. These  
 1222 three parameters are the only inputs, so signal yield uncertainties are not included. The value  
 1223  $p_{bi}$  is the probability, written in the form of “the” incomplete beta function [64] ( $B_{incomp}$ ),  
 1224 as used in the analysis. The significance is  $Z_{bi}$  and written in terms of the error functions  
 1225  $Eff$ :

$$\begin{aligned}
 \tau &= \frac{N_b}{\sigma_b^2} \\
 N_{off} &= \tau * N_b \\
 p_{bi} &= B_{incomp}\left(\frac{1}{1+\tau}, Non, N_{off} + 1\right) \\
 Z_{bi} &= \sqrt{2}Eff^{-1}(1 - 2p_{bi})
 \end{aligned}$$

1226 Not all of the background uncertainties are included for the purposes of the optimization,  
 1227 but several important ones are. Included systematic uncertainties, discussed in Section 10.1,  
 1228 are jet energy scale, b-tagging scale factor, mis-tagging scale factor, MC statistical, multijet  
 1229 background normalization,  $W+jets$  background normalization and flavor composition, and  
 1230 theoretical cross-section uncertainties.

1231 The optimization of the selections themselves is done in an iterative way. For a particular

variable, the significance is evaluated for about 300 different possible thresholds over the  
 variable range. For each histogram bin, an integral is taken in both the left and right  
 directions, the equivalent of a selection that is less than or greater than the threshold.  
 The two significance options (less than and greater than) are stored in two corresponding  
 histograms at that bin location. When all bins for a variable have been evaluated, the  
 maximum significance for each case for the variable in question is reported. After all the  
 variables we are interested in are considered, the variable with the largest significance (and  
 its associated threshold) is chosen. This selection is applied to the sample and the process is  
 repeated to choose successive selections. Figure 9.1 shows these histograms for an example  
 variable (the reconstructed top mass). The curve is relatively smooth and the choice of  
 threshold is noted. The threshold peak is relatively broad, so small changes to the MC do  
 not significantly impact the cut selection.

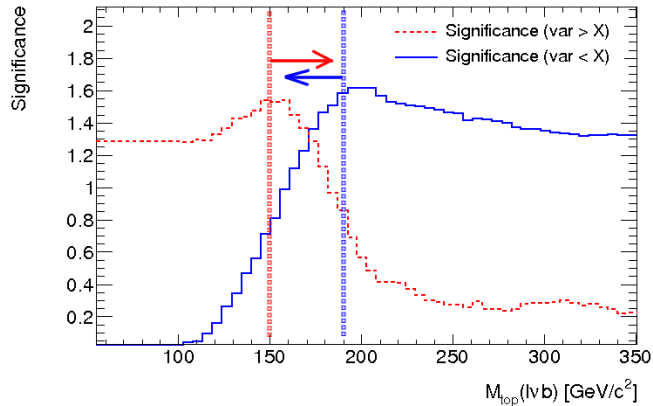


Figure 9.1: Distribution of the significance (y-axis) for the reconstructed top mass, for the 2 jet channel after preselection. The vertical lines show the optimal cut thresholds for the two selections shown (less than and greater than some reconstructed top mass value) and the arrows indicate the region that is kept after the selection is applied.

Additionally, selection sequences are considered that include the second best variable as  
 the first selection, or other high significance variables for this or other selections. This is  
 because it is possible that the best selection and threshold from the first round may be a very

1247 harsh selection. After this selection, the statistics might be too low for further selections  
1248 to improve the significance (considering the impact on the statistical uncertainties). On the  
1249 other hand, a different sequence, starting with a weaker cut but involving two other cuts,  
1250 could, as a sequence, give a better uncertainty than the first sequence (one selection) did.  
1251 Still, it should be noted that even with this variation, not all possible cut sequences are tested  
1252 and the method is biased towards selection sequences that start with strongly discriminating  
1253 variables and cut thresholds.

1254 Because the method includes uncertainties (including MC statistical uncertainty) and  
1255 involves integrals from a given bin to the end of a range, it is relatively insensitive to random  
1256 fluctuations. Additionally, the thresholds are rounded. There is no particular reason that a  
1257 selection on the reconstructed top mass of greater than 192.75 GeV, for example, should be  
1258 much better than a selection at 190 GeV. This then acts as a check on the selections reported  
1259 by the automated method and gives a more realistic view of the detector resolution.

## 1260 **9.2.2 B-tagging Threshold and Cut-Based Selections**

1261 As discussed in Section 4.3.1, the b-tagging threshold choice can have a large impact on the  
1262 analysis. Although the yields were shown in that section, we can also evaluate the impact  
1263 later in the analysis. Here, the selection optimization is repeated for three different b-tagging  
1264 operating points. The best significance (for some associated threshold) for each variable is  
1265 given, where each y-axis entry corresponds to some variable  $i$ . Figure 9.2 shows this for the  
1266 3 jets channel with positively charged leptons, preselection only, and then preselection plus  
1267 one of two strong selections on the reconstructed top mass or untagged jet  $\eta$ . In all three  
1268 cases, the higher operating point is favored. This was not necessarily expected; it could have

1269 been that a looser operating point might have been paired with a tighter threshold for some  
 1270 variable to give a higher significance than a tighter operating point. However, we can see  
 1271 that this is not the case.

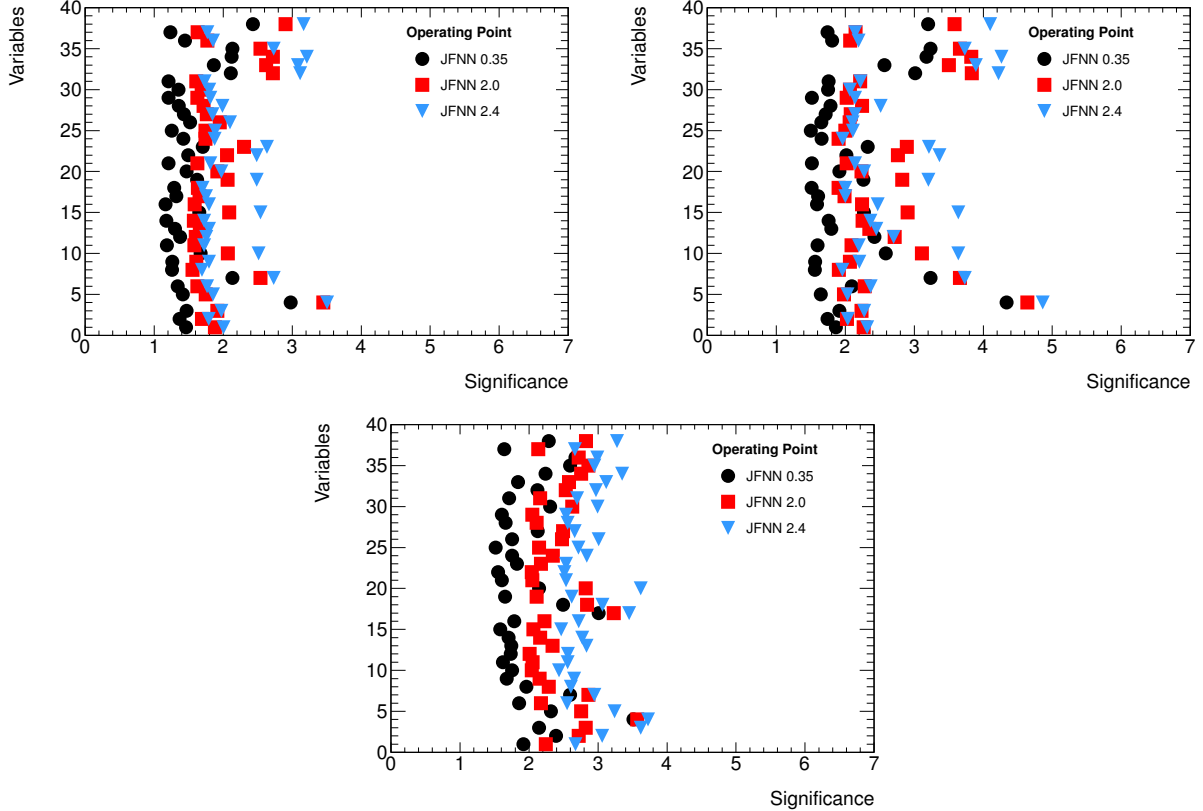


Figure 9.2: Distribution of the significance (x-axis) for various variables (each y-axis entry is a separate variable), given a JetFitterCombNN b-tagging operating point, denoted by different marker shapes. The plots are all for the 3 jets, positively charged lepton channel. The top left plot is preselection only, the top right is preselection plus a requirement that the reconstructed top mass be less than 210 GeV, and the bottom plot is preselection plus a requirement that the  $|\eta|$  of the highest  $p_T$  untagged jet be greater than 2.0. The 2.4 operating point is used in the analysis.

### 1272 9.3 Selection Choices

1273 For this analysis, the optimal variables and selection thresholds consist of four different  
 1274 selections, where the last selection is different between the channels depending on jet number.

1275 This is due to the much larger  $t\bar{t}$  background in the 3 jet bin, which is better rejected by a  
1276 different selection. There is no difference in selection for this analysis based on the lepton  
1277 charge, although it is not unreasonable that some difference in selection could happen based  
1278 on lepton charge in a future analysis, because of the different background composition.

1279 The selections in common for all channels are:  $|\eta(j_u)| > 2.0$ ,  $150 \text{ GeV} < M_{top}(l\nu b) <$   
1280  $190 \text{ GeV}$  and  $H_T > 210 \text{ GeV}$ . The 2 jet selection also requires  $|\Delta\eta(b, j_u)| > 1.0$  and the 3  
1281 jet selection requires  $M(\text{AllJets}) > 450 \text{ GeV}$ . In the case of the three jet bin, the untagged  
1282 light jet is taken to be the highest  $p_T$  untagged jet in the final state.

1283 These selections have some physical justification. The first selection makes use of the  
1284 untagged jet. Because the t-channel initial state usually contains a valence quark, the un-  
1285 tagged jet in the final state is often energetic and close to the beam line, much more often  
1286 than for the background processes. Thus, we require the untagged jet to be forward. The  
1287 second selection simply requires the reconstructed top mass to be close to the measured  
1288 value. The single-top  $t$ -channel process only has one top quark so the decay products are  
1289 the reconstructed W and the b-tagged jet (assuming we have identified this correctly). In  
1290 the case of the backgrounds, there either is no top quark, or there are too many and the  
1291 correct decay products may not be matched together during the top reconstruction. Thus,  
1292 this selection also is a powerful discriminator. The third common selection requires the sum  
1293 of the transverse momenta of the final state particles to be large, which helps to reject lower  
1294 energy  $W+jets$  or multijet events.

1295 The final selection is different for the different jet bins. In the 2 jet bin, we require the  
1296 b-tagged jet (associated with the top) and the untagged jet to be separated in  $|\eta|$ . This  
1297 helps to reject backgrounds where the two jets may have come from a gluon or both from

1298 a top quark decay, and are more likely to be close together. In the 3 jet bin, we require  
 1299 the invariant mass of the three jets to be large. This is a particularly good discriminator  
 1300 against  $t\bar{t}$  events, where these three jets may have come from a top quark, for instance. In  
 1301 the t-channel single-top signal, we expect the untagged jet to be energetic and separated  
 1302 from the b-jet, leading to a potentially large invariant mass.

1303 The individual channel compositions after all cuts are shown in Figure 9.3 and distribu-  
 1304 tions after all selections except the one on the variable pictured are shown in Figure 9.4 for  
 1305 the 2 jet selection and Figure 9.5 for the 3 jet selection. In all three cases, the t-channel  
 1306 cross-section is normalized to the observed result formed using all four channels, discussed  
 1307 in Section 10.2.1.3.

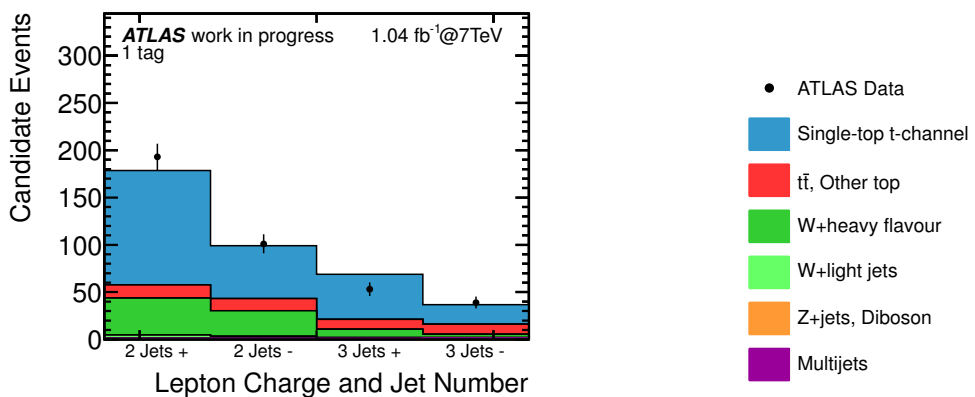


Figure 9.3: Distribution of the lepton charge after the full cut-based selection for two jets and three jets. These are the four primary analysis channels. The  $t$ -channel single-top contribution is normalized to the observed cross-section determined using all four channels. Other top refers to the  $s$ -channel and  $Wt$  single-top contributions.

1308 Table 9.1 shows the number of events after all cut-based analysis selections for the positive  
 1309 and negative lepton charge and number of jet channels. The  $t$ -channel yield is the standard  
 1310 model expectation in this table. All analysis systematic uncertainties are included in the  
 1311 reported yields. The individual uncertainty contributions are discussed in Section 10.1.

1312 Although we do not split the events by the lepton type when making analysis channels

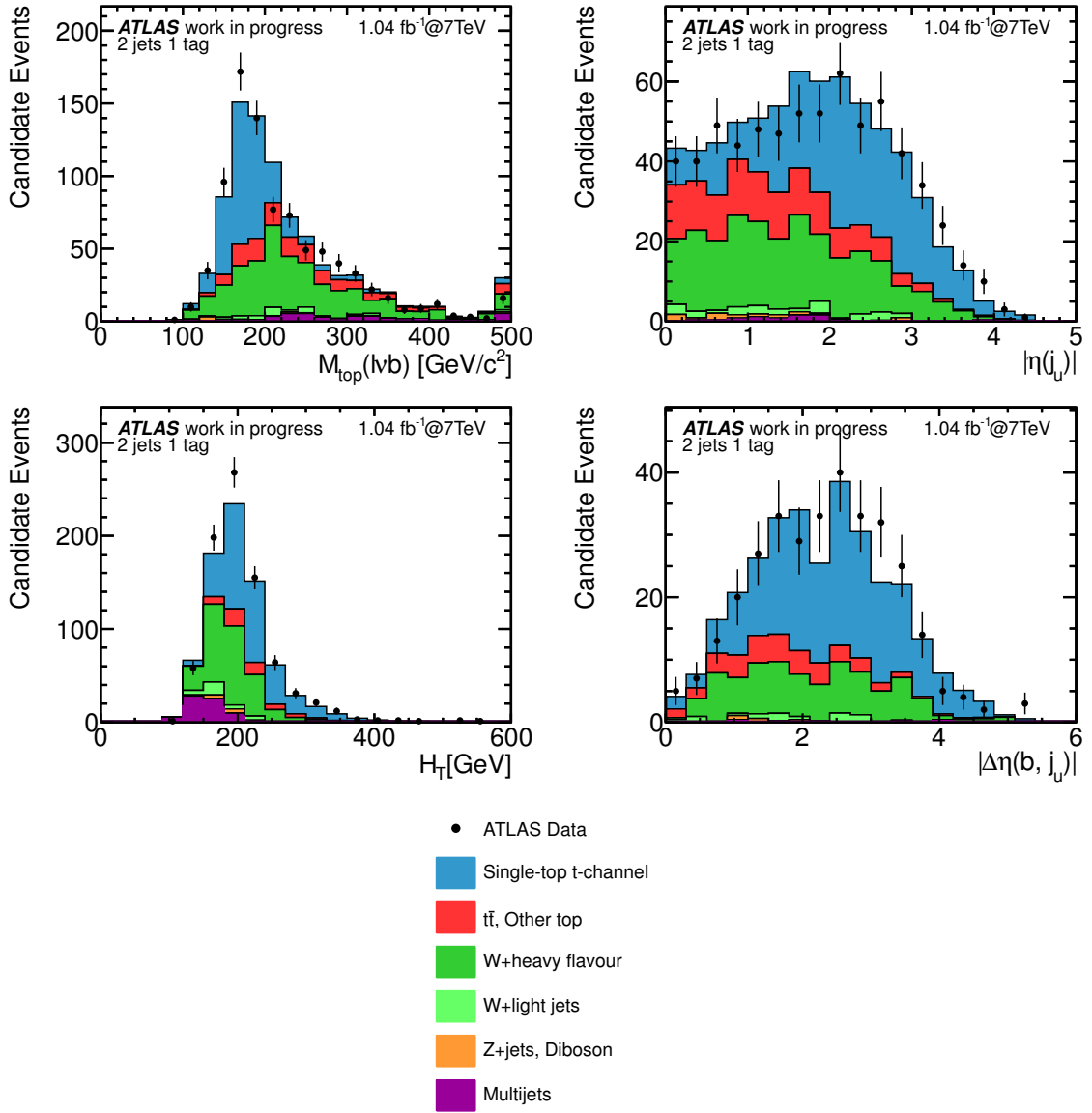


Figure 9.4: Discriminating variables for the tagged sample for two-jets events after applying all cut based cuts except for the cut on the plotted variable. The  $t$ -channel single-top contribution is normalized to the observed cross-section determined using all four channels. Other top refers to the  $s$ -channel and  $Wt$  single-top contributions. The last bin contains the sum of the events in that bin or higher.

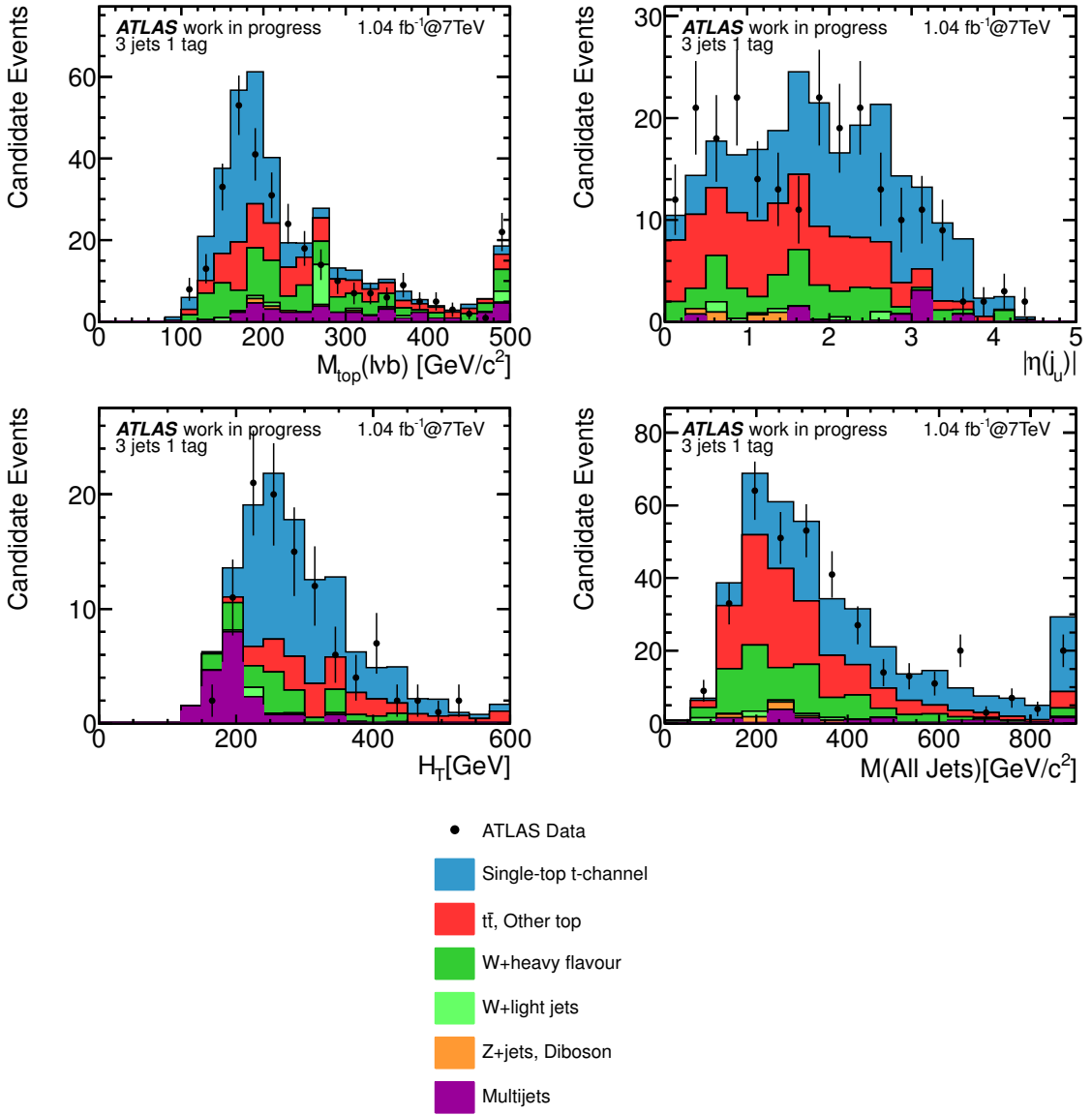


Figure 9.5: Discriminating variables for the tagged sample for three-jets events after applying all cut based cuts except for the cut on the plotted variable. The  $t$ -channel single-top contribution is normalized to the observed cross-section determined using all four channels. Other top refers to the  $s$ -channel and  $Wt$  single-top contributions. The last bin contains the sum of the events in that bin or higher.

1313 and determining the result, it is possible to investigate what the proportion of the different  
1314 leptons is in this analysis. There is no particular dependency on the lepton type inherent this  
1315 analysis and we would expect the number of electrons and muons to be roughly equal. To  
1316 determine these numbers we use all of the analysis channels combined (plus and minus charge,  
1317 two and three jets) after the cut-based selections, the  $t$ -channel single-top contribution is  
1318 normalized to the observed cross-section determined using all four channels, and the multijets  
1319 and W+jets contributions determined using the data-based normalizations. The expected  
1320 number of events with muons is 204 and there are 182 corresponding data events observed.  
1321 For the electron selection, there are 181 events expected and 204 events observed in data.  
1322 These numbers are very similar and demonstrate the roughly one to one ratio of muons and  
1323 electrons in this analysis. The deviation of the electron yield from muon yield is about 10%,  
1324 which is well within the uncertainties for this analysis. The systematic uncertainty on the  
1325 total expected yield by channel is given in Table 9.1 and is about 15 to 20%, while the data  
1326 statistical uncertainty is about 7 to 8%.

	Cut-based 2 Jets		Cut-based 3 Jets	
	Lepton +	Lepton -	Lepton +	Lepton -
<i>t</i> -channel	$85.2 \pm 28.6$	$39.4 \pm 12.8$	$33.6 \pm 7.0$	$14.6 \pm 6.2$
$t\bar{t}$ , Other top	$14.0 \pm 6.4$	$12.8 \pm 4.2$	$10.5 \pm 4.2$	$10.7 \pm 7.9$
$W$ +light jets	$3.3 \pm 1.9$	$2.0 \pm 1.2$	$0.8 \pm 1.3$	$0.3 \pm 0.3$
$W$ +heavy flavour jets	$39.1 \pm 10.6$	$27.1 \pm 7.5$	$8.7 \pm 6.0$	$3.4 \pm 3.1$
$Z$ +jets, Diboson	$1.1 \pm 0.8$	$1.0 \pm 0.8$	$0.3 \pm 0.2$	$0.2 \pm 0.3$
Multijets	$0.2 \pm 0.2$	$0.3 \pm 0.3$	$1.5 \pm 1.1$	$3.1 \pm 2.0$
TOTAL Exp	$142.9 \pm 31.2$	$82.6 \pm 15.5$	$55.5 \pm 10.2$	$32.2 \pm 10.68$
S/B	1.5	0.9	1.6	1.0
DATA	193	101	53	39

Table 9.1: Event yield for the two-jets and three-jets tag positive and negative lepton-charge channels after the cut-based selection. The multijets and  $W$ +jets backgrounds are normalized to the data, all other samples are normalized to theory cross-sections (including single-top  $t$ -channel). Uncertainties shown are systematic uncertainties. Other top refers to the  $s$ -channel and  $Wt$  single-top contributions.

<sub>1327</sub> **Chapter 10**

<sub>1328</sub> **The Measurements**

<sub>1329</sub> The purpose of this dissertation is to measure the single-top t-channel cross-section. In  
<sub>1330</sub> previous chapters we have spent much time reducing the backgrounds, first in an initial  
<sub>1331</sub> preselection and then again using cut-based selections. In this chapter, we evaluate the  
<sub>1332</sub> signal cross-section after applying these selections. We also estimate the value of the CKM  
<sub>1333</sub> matrix element  $|V_{tb}|$ .

<sub>1334</sub> **10.1 Systematic Uncertainties**

<sub>1335</sub> Before we can determine the cross-section, we need to evaluate the uncertainties on the  
<sub>1336</sub> quantities which go into the calculation. The cross-section is related to the number of events  
<sub>1337</sub> that are observed for some given amount of proton-proton interactions, as stated in Sec-  
<sub>1338</sub> tion 2.3.2. If more events are observed than expected, the cross-section is higher than the  
<sub>1339</sub> expected value. Uncertainties on the measurement are important here, as deviations from  
<sub>1340</sub> the expected cross-section may well be due to systematic uncertainties. In this section, we  
<sub>1341</sub> discuss the systematic uncertainties on the measurement.

1342 There are several systematic uncertainties in this analysis and we overview them by  
1343 category and then give some information about their impact on the signal and background  
1344 yields. Most of the uncertainties are related to the MC. For additional information on most  
1345 of the scale factors, corrections, and MC itself, see Chapter 5.

1346 **b-tagging:** There is an uncertainty associated with the b-tagging and mis-tagging scale  
1347 factors, which relate the efficiencies measured in data to that in MC. The b-tagging scale  
1348 factor uncertainty in particular can be large in this analysis. There is also a c-tagging  
1349 efficiency uncertainty, which for this analysis is assumed to be twice that of the b-tagging  
1350 efficiency uncertainty. This is considered fully correlated with the uncertainty in b-tagging  
1351 efficiency and is included in the reported b-tagging efficiency uncertainty (which may also  
1352 be called the heavy flavor b-tagging scale factor uncertainty). This is a large uncertainty for  
1353 this analysis, with variations of around 10% on the signal and background yields.

1354 **Leptons:** There are uncertainties on the lepton scale factors, which relate the trigger,  
1355 ID, and reconstruction scale factors in data to MC, and also uncertainties on the lepton  
1356 energy scale and resolution, which are uncertainties related to smearing the lepton energy,  
1357 described in Section 5.2.5. Also, for this study there was an issue with the MC related to the  
1358 muon trigger matching. This caused us not to apply trigger matching for the muon channel  
1359 (although the trigger itself was still applied). An uncertainty of 1.5% was added to account  
1360 for this. These uncertainties are typically < 5% for the different analysis processes.

1361 **Jets:** There are three uncertainties associated with jets regarding the jet energy scale  
1362 (JES), jet energy resolution (JER) and jet reconstruction (jetreco). The JES uncertainty [37,  
1363 38] is related to the energy calibration. For example, we may not have perfectly simulated the  
1364 dead material or leakage when adjusting the energy and there is some uncertainty related

1365 to this. There may be noise or uncertainties related to the MC as well. JES includes  
1366 a few different components, including a pileup and b-JES contribution. The pileup is a  
1367 special correction to account for pileup conditions during 2011 data taking and the effect  
1368 on jet energies. The b-JES factor is a separate corrections for jets which have a truth b-  
1369 quark assignment. It considers b-quark fragmentation, material and calorimeter response  
1370 separately for these jets. There is also some consideration of flavor composition uncertainty  
1371 (gluon fraction distribution), which has a different distribution for each of the top samples  
1372 and a flat distribution for other processes. The distance to other jets is also considered and  
1373 jets that are close to one another have a different uncertainty. Overall, this JES uncertainty  
1374 (after including W+jets scale factor correlations) is largest for the light quark W+jets events,  
1375 which are removed effectively by analysis cuts. The impact is around 10% for  $t\bar{t}$  and a few  
1376 percent for the signal in the largest signal channel, 2 jets with a positive lepton charge.

1377 The other two jet related uncertainties generally have an impact of a few percent for the  
1378 different processes. The JER uncertainty is related to the jet energy value and is evaluated  
1379 by smearing the jet energy (this is not done in the nominal sample, unlike for leptons, as  
1380 discussed in Section 5.2.5). The jet reconstruction evaluates how sensitive the analysis is to  
1381 a missed jet. This is done by randomly dropping jets from the event based on jet kinematics.

1382 **Theoretical cross-section:** There are several processes for which we do not have data-  
1383 based normalization estimates. In most cases, the contribution of these processes to the  
1384 final yield is small. In the case of  $t\bar{t}$ , we have performed a cross-check (see Appendix A)  
1385 and found the estimated normalization is consistent with the theoretical value, which has a  
1386 smaller uncertainty. We use a 10% uncertainty for the single-top s-channel and Wt processes,  
1387 5% for diboson processes, 60% uncertainty for Z+jets and the cross-section variation is taken

1388 to be  $164.57^{+11.4}_{-15.7} \text{ pb}$  for the  $t\bar{t}$  process. In this analysis we combine certain processes together  
1389 when reporting yields and results. When this is done, uncertainties such as the theoretical  
1390 cross-section uncertainty are based on the proportion of each process in the combined sample  
1391 (rather than taking the largest uncertainty, for instance).

1392 **Multijets:** There is an uncertainty on the multijets normalization, discussed in Sec-  
1393 tion 7.1. This is determined by re-doing the fit, which determines the normalization, using  
1394 a different variable (W transverse mass). We use 50% for this uncertainty.

1395 **W+jets:** There are uncertainties on the  $W+\text{jets}$  scale factors discussed in Section 7.2.  
1396 These include b-tagging scale factor, mis-tagging scale factor, JES, theoretical cross-section,  
1397 and data statistical uncertainties. Many of these uncertainties are correlated with the uncer-  
1398 tainties in the t-channel single-top cross-section measurement. This means that the behavior  
1399 of the JES uncertainty for the  $W+\text{jets}$  scale factor estimate and  $W+\text{jets}$  yield JES uncer-  
1400 tainty are related to each other.

1401 To properly include these correlations, we re-estimate the  $W+\text{jets}$  scale factors for each  
1402 uncertainty scenario and then apply the appropriate scale factor when estimating the  $W+\text{jets}$   
1403 yield uncertainty. We assume that the JES upward shift scenario, for example, is the “real”  
1404 scenario and do all of the estimations such as we would for the nominal sample, using JES  
1405 upwardly shifted numbers instead of nominal numbers. Then, to find the total JES upwardly  
1406 shifted uncertainty, we compare the final yield (with the JES shifted scale factors applied to  
1407 the JES shifted sample) to the nominal sample (with the nominal scale factors applied to  
1408 the nominal sample).

1409 The JES, b-tagging scale factor and mis-tagging scale factor uncertainties quoted in this  
1410 document always include these correlation effects. The theoretical cross-section uncertain-

1411 ties and multijet normalization uncertainties for the  $W+jets$  scale factors are also correlated,  
1412 but because they are not correlated with  $W+jets$  yield uncertainties, they are listed sepa-  
1413 rately when uncertainties are given by processes (and are given in this way to the statistical  
1414 tool). The correlations are included in the final cross-section measurement. Finally, the  
1415 statistical uncertainties are considered separately and are called the  $W+jets$  normalization  
1416 uncertainties. These are  $\leq 5\%$ .

1417 There is another uncertainty associated with the  $W+jets$  normalization, related to the  
1418 propagation of the scale factors from the 2 jet bin to other bins. This is a 25% uncertainty  
1419 for a movement to the 3 jet bin, which is the other primary analysis bin. This is referred to  
1420 as the  $W+3$  jet bin normalization.

1421 One additional uncertainty related to the  $W+jets$  is an uncertainty on the simulated  
1422 shape. To evaluate this, two ALPGEN [52, 65] parameters are varied and the uncertainties  
1423 from these two variations are added in quadrature. These parameters are the minimum  
1424 ALPGEN  $p_T$  to make a parton a hard (high  $p_T$ ) parton ( $ptjmin$ ) and the function which  
1425 gives the factorization scale for the pdf ( $iqopt$ ).

1426 **MC statistical:** There is an uncertainty associated with the number of simulated MC  
1427 events. If not enough events are generated, there may not be a sufficient range of kinematics  
1428 to accurately represent the data. The uncertainty is evaluated as the square root of the sum  
1429 of the squares of the event weights and can range as high as 98% after all cut-based analysis  
1430 selections.

1431 **LAr hole:** There is some uncertainty on the removal of events affected by the LAr hole,  
1432 discussed in Section 3.2.8. The uncertainty is a  $\pm 1$  sigma variation of the hole size and  
1433 typically has a  $< 5\%$  effect on the signal and background yields.

1434        **Missing  $E_T$ :** There are two  $E_T^{\text{miss}}$  related uncertainties. The first is due to pileup  
1435 effects ( $E_T^{\text{miss}}$  pileup uncertainty) and the second is due to energy scale and energy resolution  
1436 effects ( $E_T^{\text{miss}}$  uncertainty), including cell out contribution uncertainties (energy deposits not  
1437 associated with jets, electrons,  $\tau$ 's or photons) and soft jet uncertainties (related to objects  
1438 that have a  $p_T$  too low to be considered a jet). The pileup uncertainty portion is a 10%  
1439 variation. Both uncertainties typically range from 1 – 10%.

1440        **ISR/FSR:** There is some uncertainty on the MC simulation of the initial and final state  
1441 radiation. These are extra particles perhaps formed by gluons producing extra radiation  
1442 (jets) in the initial or final state portion of the Feynman diagram. Extra jets, if the  $p_T$  is  
1443 high enough, could move events from the 2 jet channel to the 3 jet channel and thus affect  
1444 the analysis. This uncertainty is evaluated by changing certain parameters when producing  
1445 the MC, and is evaluated separately for the  $t\bar{t}$  and single-top processes. Special ACERMC  
1446 samples showered with PYTHIA are used for all the top processes. For this analysis, we  
1447 vary the ISR and FSR simultaneously (which produces a larger variation than varying them  
1448 separately for the largest signal channel, 2 jets with positive leptons). This is one of the  
1449 largest uncertainties, with variations of around 10 – 30% depending on the process.

1450        **PDF:** The parton distribution function may also not be well modelled. The uncertainty  
1451 is evaluated by finding the variation from changing the PDF in the preselection sample  
1452 from the one used in this analysis, CTEQ6L, to CTEQ66 [48], NNPDF20 [66, 67], or  
1453 MSTW2008nnlo68cl [68, 69]. This uncertainty ranges from 1% to 8% depending on the  
1454 process.

1455        **Generator and Shower:** The MC generator or showering programs may not exactly  
1456 match the data. To evaluate these uncertainties, an alternative generator or showering

1457 program is used and the deviation determined. This is done for the  $t\bar{t}$  and the single-top  
1458 processes. For the t-channel single-top process, MCFM [70] is used to determine a deviation  
1459 with the preselection sample of 7%. For the other processes, the generator uncertainties are  
1460 determined after cut-based selections as usual, using MC@NLO versus HERWIG for  $t\bar{t}$  and  
1461 AcerMc versus MC@NLO for the s-channel and Wt single-top processes. The shower un-  
1462 certainties for the single-top processes are determined using AcerMc plus PYTHIA versus  
1463 AcerMc plus HERWIG. The  $t\bar{t}$  shower uncertainties are found by comparing yields from  
1464 Powheg [71, 72] plus PYTHIA and Powheg plus HERWIG. These uncertainties are all sym-  
1465 metrized, so the deviation between the nominal and alternate program is divided in half.  
1466 One half is taken as the up shift, and the other is taken as the down shift. These are some  
1467 of the larger uncertainties in the analysis, with variations around 10 – 15% depending on  
1468 the process.

1469         **$\eta$  reweighting:** The shape of the  $\eta$  distribution of the forward jet is not especially  
1470 well-modeled. We renormalize the MC to the data in a pretag sample and then evaluate the  
1471 difference between using this and using the nominal sample after all of the analysis selections.  
1472 This uncertainty is a one-sided uncertainty (there is only a positive shift, no negative shift).  
1473 The uncertainty is about 5 – 10% depending on the process.

1474        **Luminosity:** The luminosity estimate has some uncertainty associated with it. The  
1475 luminosity estimate is done with dedicated luminosity estimate runs. The uncertainty is  
1476 3.7% [26] for the data used in this analysis.

1477        The individual uncertainties that are used to find the total cross-section uncertainties  
1478 are given in Table 10.1, Table 10.2, Table 10.3, and Table 10.4 by process, where each table  
1479 gives the values for a different analysis channel. These are the values which are used in the

1480 statistical tool (see Section 10.2.1) to determine the cross-section. In certain cases, processes  
1481 have very high MC statistical uncertainties after all cut-based selections, especially in the 3  
1482 jet channels. This can cause some large estimates for other uncertainties as well. Although  
1483 the actual uncertainties may not be as high as we estimate, we keep the large values to be  
1484 conservative.

### 1485 10.1.1 Effect of Pileup

1486 For this study, there are on average about 6 interactions per crossing (primary vertices),  
1487 and it is possible that extra events could cause problems at the reconstruction level when  
1488 identifying the primary vertex or reconstructing jets. To determine the impact of pileup on  
1489 this analysis, the MC was divided into two samples based on the number of primary vertices  
1490 in the event, where high pileup is considered to be  $\geq 6$  primary vertices and low pileup  
1491 is considered to be  $< 6$  primary vertices. The sample is divided before any selections and  
1492 then normalized to the expected yields in both cases. The analysis is repeated using each  
1493 sample, and we find that the cross-section shifts by 6% versus nominal when using the high  
1494 pileup sample and 4% versus nominal when using the low pileup sample. This is within the  
1495 statistical uncertainty of the analysis and also within the MC statistical uncertainty, which  
1496 increases when the sample is halved. Based on this study, we consider the analysis to be  
1497 insensitive to pileup effects.

## 1498 10.2 Results

1499 In this section we discuss the technique used to determine the observed cross-section and  
1500 the  $|V_{tb}|$  value. We discuss five different results, involving different combinations of the

Uncertainties(%)	$t$ -channel	$t\bar{t}$ , Wt, s	$W+\text{light}$	$W+\text{heavy}$	$Z,\text{Dib.}$	Multijets
Jet energy scale	-3	-11	-19	-1	33	-
	-1	7	28	-9	-9	-
Jet energy resolution	$\pm 4$	$\pm 1$	-	-	$\pm 4$	-
Jet reconstruction	$< 1$	$< 1$	$\pm 2$	$< 1$	$\pm 1$	-
$b$ tagging scale factor	12	9	7	-3	15	-
	-12	-9	-10	3	-15	-
Mistag scale factor	$< 1$	$< 1$	24	-4	5	-
	$< 1$	$< 1$	-23	4	-5	-
Lepton scale factor	$\pm 3$	$\pm 3$	-	-	$\pm 2$	-
Lepton efficiencies	$\pm 1$	$\pm 1$	-	-	$\pm 4$	-
Generator single-top	$\pm 7$	$\pm 1$	-	-	-	-
Generator $t\bar{t}$	-	$\pm 1$	-	-	-	-
Shower	$\pm 11$	$\pm 12$	-	-	-	-
ISR/FSR	-15	32	-	-	-	-
	27	39	-	-	-	-
PDF	$\pm 3$	$\pm 8$	-	-	$\pm 1$	-
Luminosity	$\pm 4$	$\pm 4$	-	-	$\pm 4$	-
$E_T^{\text{miss}}$	-1	-1	-5	-5	-1	-
	$< 1$	1	-16	$< 1$	$< 1$	-
$E_T^{\text{miss}}$ pileup	-2	-1	-5	-5	-1	-
	$< 1$	1	-16	-2	$< 1$	-
LAr	1	1	$< 1$	$< 1$	$< 1$	-
	-1	-1	$< 1$	-1	$< 1$	-
$\eta$ reweighting	5	2	$< 1$	4	9	-
$W$ shape	-	-	$< 1$	$< 1$	-	-
$Wjj$ norm	-	-	$< 1$	-	-	-
$Wc, cc, bb$ norm	-	-	-	$\pm 5$	-	-
$W$ 3 jet norm	-	-	-	-	-	-
Multijets	-	-	$\pm 3$	$\pm 9$	-	$\pm 50$
$t\bar{t}$ XS	-	$\pm 5$	$\pm 1$	$\pm 5$	-	-
single-top XS	-	$\pm 2$	$\pm 4$	$\pm 17$	-	-
$Z+jets$ XS	-	-	$\pm 6$	$\pm 2$	$\pm 41$	-
Diboson XS	-	-	$< 1$	$< 1$	$\pm 2$	-
MC Statistics	$\pm 4$	$\pm 6$	$\pm 34$	$\pm 12$	$\pm 47$	$\pm 100$

Table 10.1: Percent systematic uncertainties for the 2 jet plus channel. Here, XS means cross-section,  $Z$  means  $Z+jets$ , and Dib. means diboson. Norm refers to normalization, s indicates single-top  $s$ -channel. If two values are given, the top value is the upshift and the bottom value is the downshift.

Uncertainties(%)	$t$ -channel	$t\bar{t}$ , Wt, s	$W$ +light	$W$ +heavy	$Z$ , Dib.	Multijets
Jet energy scale	< 1 -4	-7 9	-22 -19	3 -11	-1 -20	-
Jet energy resolution	$\pm 3$	$\pm 1$	-	-	$\pm 30$	-
Jet reconstruction	< 1	< 1	$\pm 1$	$\pm 2$	$\pm 2$	-
$b$ tagging scale factor	12 -12	9 -9	9 -12	2 -3	4 -4	-
Mistag scale factor	< 1 < 1	< 1 < 1	23 -22	-3 3	21 -21	-
Lepton scale factor	$\pm 3$	$\pm 3$	-	-	$\pm 3$	-
Lepton efficiencies	$\pm 2$	< 1	-	-	$\pm 5$	-
Generator single-top	$\pm 7$	< 1	-	-	-	-
Generator $t\bar{t}$	-	$\pm 9$	-	-	-	-
Shower	$\pm 14$	$\pm 5$	-	-	-	-
ISR/FSR	-14 24	-16 25	-	-	-	-
PDF	$\pm 3$	$\pm 8$	-	-	$\pm 1$	-
Luminosity	$\pm 4$	$\pm 4$	-	-	$\pm 4$	-
$E_T^{\text{miss}}$	-4 < 1	< 1 2	-7 < 1	-13 2	< 1 1	-
$E_T^{\text{miss}}$ pileup	-3 < 1	< 1 2	-7 < 1	-11 2	< 1 < 1	-
LAr	< 1 -1	1 -1	< 1 -1	< 1 -3	< 1 < 1	-
$\eta$ reweighting	4	2	4	4	4	-
$W$ shape	-	-	$\pm 3$	$\pm 2$	-	-
$Wjj$ norm	-	-	< 1	-	-	-
$Wc, cc, bb$ norm	-	-	-	$\pm 4$	-	-
$W$ 3 jet norm	-	-	-	-	-	-
Multijets	-	-	$\pm 3$	$\pm 6$	-	$\pm 50$
$t\bar{t}$ XS	-	$\pm 6$	$\pm 1$	$\pm 1$	-	-
single-top XS	-	$\pm 2$	$\pm 4$	$\pm 5$	-	-
$Z+jets$ XS	-	-	$\pm 6$	$\pm 2$	$\pm 40$	-
Diboson XS	-	-	< 1	< 1	$\pm 2$	-
MC Statistics	$\pm 6$	$\pm 6$	$\pm 45$	$\pm 15$	$\pm 55$	$\pm 100$

Table 10.2: Percent systematic uncertainties by process for the 2 jet minus channel. Here, XS means cross-section,  $Z$  means  $Z+jets$ , and Dib. means diboson. Norm refers to normalization, s indicates single-top  $s$ -channel. If two values are given, the top value is the upshift and the bottom value is the downshift.

Uncertainties(%)	$t$ -channel	$t\bar{t}$ , Wt, s	$W$ +light	$W$ +heavy	$Z$ , Dib.	Multijets
Jet energy scale	4 -10	-8 16	18 -17	37 17	-32 -40	-
Jet energy resolution	< 1	< 1	-	-	$\pm 10$	-
Jet reconstruction	$\pm 1$	< 1	$\pm 2$	$\pm 2$	$\pm 3$	-
$b$ tagging scale factor	9 -9	7 -8	2 -4	-7 9	11 -11	-
Mistag scale factor	< 1 < 1	< 1 < 1	33 -32	-4 3	1 -1	-
Lepton scale factor	$\pm 3$	$\pm 3$	-	-	$\pm 2$	-
Lepton efficiencies	$\pm 1$	$\pm 1$	-	-	$\pm 9$	-
Generator single-top	$\pm 7$	< 1	-	-	-	-
Generator $t\bar{t}$	-	$\pm 22$	-	-	-	-
Shower	$\pm 7$	$\pm 8$	-	-	-	-
ISR/FSR	-5 -1	4 22	-	-	-	-
PDF	$\pm 3$	$\pm 8$	-	-	$\pm 1$	-
Luminosity	$\pm 4$	$\pm 4$	-	-	$\pm 4$	-
$E_T^{\text{miss}}$	-1 3	-1 -2	-98 $< 1$	5 -3	$< 1$ $< 1$	-
$E_T^{\text{miss}}$ pileup	1 1	< 1 -2	-98 $< 1$	5 -5	$< 1$ $< 1$	-
LAr	< 1 -2	2 -1	< 1 -2	< 1 -2	< 1 -1	-
$\eta$ reweighting	6	4	4	7	5	-
$W$ shape	-	-	$\pm 2$	$\pm 1$	-	-
$Wjj$ norm	-	-	$\pm 1$	-	-	-
$Wc, cc, bb$ norm	-	-	-	$\pm 5$	-	-
$W$ 3 jet norm	-	-	$\pm 25$	$\pm 25$	-	-
Multijets	-	-	$\pm 6$	$\pm 15$	-	$\pm 50$
$t\bar{t}$ XS	-	$\pm 7$	$\pm 3$	$\pm 14$	-	-
single-top XS	-	< 1	$\pm 2$	$\pm 38$	-	-
$Z+jets$ XS	-	-	$\pm 7$	$\pm 3$	$\pm 40$	-
Diboson XS	-	-	< 1	< 1	$\pm 2$	-
MC Statistics	$\pm 7$	$\pm 6$	$\pm 70$	$\pm 23$	$\pm 67$	$\pm 48$

Table 10.3: Percent systematic uncertainties by process for the 3 jet plus channel. Here, XS means cross-section,  $Z$  means  $Z+jets$ , and Dib. means diboson. Norm refers to normalization, s indicates single-top  $s$ -channel. If two values are given, the top value is the upshift and the bottom value is the downshift.

Uncertainties(%)	$t$ -channel	$t\bar{t}$ , Wt, s	$W$ +light	$W$ +heavy	$Z$ , Dib.	Multijets
Jet energy scale	7	-6	-39	73	< 1	-
	-21	14	-26	24	55	-
Jet energy resolution	$\pm 1$	$\pm 6$	-	-	$\pm 12$	-
Jet reconstruction	< 1	$\pm 1$	$\pm 2$	$\pm 1$	$\pm 10$	-
$b$ tagging scale factor	9	6	6	-3	18	-
	-9	-8	-7	3	-18	-
Mistag scale factor	< 1	< 1	16	-4	< 1	-
	< 1	< 1	-16	4	< 1	-
Lepton scale factor	$\pm 3$	$\pm 3$	-	-	$\pm 98$	-
Lepton efficiencies	$\pm 3$	$\pm 2$	-	-	$\pm 17$	-
Generator single-top	$\pm 7$	< 1	-	-	-	-
Generator $t\bar{t}$	-	$\pm 30$	-	-	-	-
Shower	$\pm 10$	$\pm 50$	-	-	-	-
ISR/FSR	29	40	-	-	-	-
	30	22	-	-	-	-
PDF	$\pm 3$	$\pm 8$	-	-	< 1	-
Luminosity	$\pm 4$	$\pm 4$	-	-	$\pm 4$	-
$E_T^{\text{miss}}$	-4	< 1	< 1	< 1	< 1	-
	-4	< 1	< 1	< 1	< 1	-
$E_T^{\text{miss}}$ pileup	-4	-1	< 1	-1	< 1	-
	-3	-1	< 1	< 1	< 1	-
LAr	< 1	1	< 1	< 1	< 1	-
	-1	-2	< 1	< 1	< 1	-
$\eta$ reweighting	5	5	6	4	5	-
$W$ shape	-	-	$\pm 3$	$\pm 1$	-	-
$Wjj$ norm	-	-	$\pm 1$	-	-	-
$Wc, cc, bb$ norm	-	-	-	$\pm 5$	-	-
$W$ 3 jet norm	-	-	$\pm 25$	$\pm 25$	-	-
Multijets	-	-	$\pm 6$	$\pm 12$	-	$\pm 50$
$t\bar{t}$ XS	-	$\pm 6$	$\pm 3$	$\pm 10$	-	-
single-top XS	-	< 1	$\pm 2$	$\pm 26$	-	-
Z+jets XS	-	-	$\pm 7$	$\pm 3$	$\pm 60$	-
Diboson XS	-	-	< 1	< 1	< 1	-
MC Statistics	$\pm 11$	$\pm 6$	$\pm 66$	$\pm 35$	$\pm 98$	$\pm 39$

Table 10.4: Percent systematic uncertainties by process for the 3 jet minus channel. In this table, XS means cross-section,  $Z$  means  $Z$ +jets, and Dib. means diboson. Norm refers to normalization, s indicates single-top  $s$ -channel. If two values are given, the top value is the upshift and the bottom value is the downshift.

1501 four channels considered based on the number of jets and lepton charge: 2 jets with a  
1502 positively charged lepton, 2 jets with a negatively charged lepton, 3 jets with a positively  
1503 charged lepton, 3 jets with a negatively charged lepton. These combinations are 2 jets, 3 jets,  
1504 plus (positively charged lepton), minus (negatively charged lepton), and all four channels  
1505 combined. The measurement from the combination of the four channels leads to the primary  
1506 analysis result.

### 1507 10.2.1 Cross-section Calculation and Measurements

1508 As mentioned earlier, the cross-section is related to the number of observed events. How-  
1509 ever, multiple analysis channels and a variety of uncertainties make the calculation more  
1510 complicated than simply subtracting the expected background yield from the data and find-  
1511 ing the deviation of this value from the expected signal yield. The cross-section calculation  
1512 is performed using a statistical tool called BILL (Binned Log Likelihood Fitter) [73], used  
1513 previously for a neural network single-top analysis [9].

1514 The cross-section is determined via a maximum likelihood fit of the MC to the data,  
1515 allowing different yields to float by different amounts within a range related to a Gaussian  
1516 constraint term. Scale factors ( $\beta$ ) are determined for each process, where these scale factors  
1517 are the ones that give the best fit to the data, for all channels considered. The data-based  
1518  $W+jets$  and multijet estimates are not allowed to vary at all, while the other non-signal  
1519 processes may float within their theoretical cross-section uncertainties. The signal yield has  
1520 no restrictions. The fit is based on a product of Poisson likelihoods for each channel which is  
1521 multiplied by the product of the Gaussian constraints for all the backgrounds. The Gaussian  
1522 distributions account for our prior knowledge of the backgrounds, and have a mean of 1 and a

1523 width of the theoretical uncertainty variation ( 0 for data-based backgrounds, the theoretical  
1524 uncertainty for other backgrounds).

1525 Because this analysis is a cut-and-count type of analysis, each channel has a distribution  
1526 which is just one bin, each measurement uses 2 or 4 channels, and the fit itself is very  
1527 straight-forward. The results of the fit are given in Table 10.5, where these values are scale  
1528 factors to be multiplied onto the MC to get the observed yield. These factors are the output  
1529 from the BILL tool. Because the data-based backgrounds have a  $\beta$  value defined to be 1,  
1530 and the other backgrounds have low theoretical uncertainties, the only  $\beta$  values that are not  
1531 approximately 1 are those for the signal. The t-channel factor is multiplied by the expected  
1532 cross-section to obtain the observed cross-section.

Channels	$t$ -channel	$t\bar{t}$ , Other top	$W$ +light	$W$ +heavy	$Z$ +jets, Diboson	Multijets
All Channels	1.41843	0.99361	1.000000	1.000000	1.00834	1.00000
2 Jets	1.55434	0.99848	1.000000	1.000000	0.99740	1.00000
3 Jets	1.05444	1.00790	1.000000	1.000000	1.00147	1.00000
Plus Charge	1.40058	0.99168	1.000000	1.000000	1.00654	1.00000
Minus Charge	1.46533	1.00001	1.000000	1.000000	1.00005	1.00000

Table 10.5: The fit values by process and channel. The 2 or 3 jet channels include both lepton charges, and the lepton charge channels include both 2 and 3 jet events. All channels is the combination of plus and minus lepton charge events, with 2 or 3 jets.

1533 This tool uses a frequentist method to determine the cross-section uncertainties, meaning  
1534 many (100,000) different pseudo-experiments are generated based on the input yield and  
1535 uncertainties. In this way, all the various possibilities within uncertainties are explored and  
1536 a distribution reflecting the probability of all possible outcomes is created, where the RMS  
1537 reflects the overall combined uncertainty of the measurement. The number of events in each  
1538 pseudo-experiment are determined via a Poisson distribution with a mean of the expected  
1539 yield and the uncertainties varied by Gaussian distributed random numbers. There is also

1540 a factor related specifically to the theoretical uncertainties of the backgrounds, as was the  
1541 case for the fit to determine the  $\beta$  values, but again this has a small impact on the result.

1542 The results of all of these repetitions are displayed in a distribution like in Figure 10.1,  
1543 where the total cross-section uncertainty is derived from the mean and the RMS of the  
1544 distribution. For the observed uncertainty, the yields are scaled by the fit values, so  $\beta$  is  
1545 now 1. The deviation of the mean from 1 is the bias (representing the asymmetry of the  
1546 uncertainties), and this added in quadrature with the RMS gives one side of the uncertainty,  
1547 while the RMS alone (0 bias assumption) gives the other uncertainty shift. In other words,  
1548 the uncertainty is the  $\sqrt{RMS^2}$  or  $\sqrt{(1 - mean)^2 + RMS^2}$ . For the example in Figure 10.1,  
1549 which uses observed yields for all four channels and includes all of the uncertainties, the RMS  
1550 is 0.284 and the mean is 1.133, giving uncertainties of +31% and -28%.

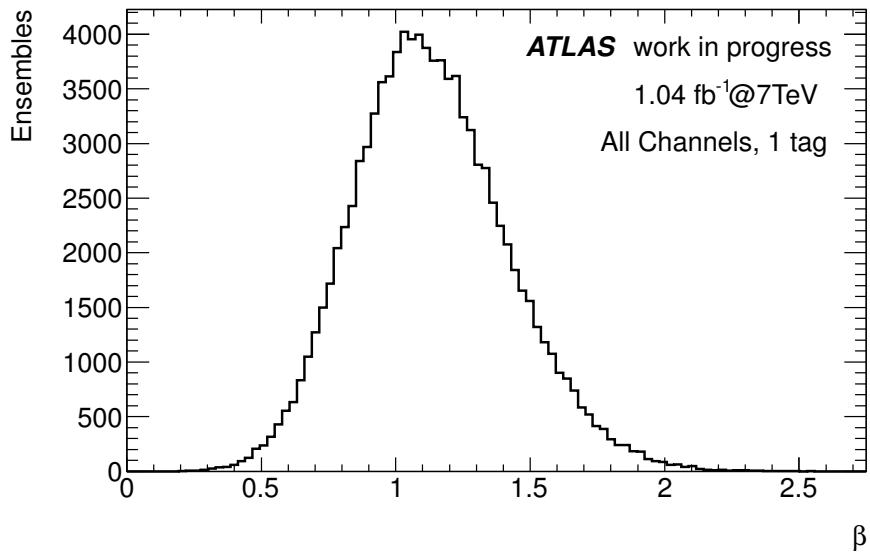


Figure 10.1: Pseudo-experiment distribution used for the final cross-section uncertainty determination. This distribution is for the observed cross-section uncertainty, for all channels combined. The  $\beta$  value is the fit for a given pseudo-experiment with yields scaled by the values in Table 10.5, and the uncertainty is determined from the distribution RMS and deviation of the mean from 1.

1551 **10.2.1.1 Two and Three jet Single Top Quark t-channel Production**

1552 We can combine our four channels into sets of 2 jets and 3 jets (lepton charges are combined).  
1553 When this is done we find a cross-section of  $\sigma_t = 100^{+9}_{-9}(\text{stat})^{+32}_{-31}(\text{syst}) = 100^{+33}_{-32}$  pb for 2  
1554 jets, where the expected cross-section is  $\sigma_t = 65^{+23}_{-23}$  pb, and  $\sigma_t = 68^{+13}_{-13}(\text{stat})^{+28}_{-22}(\text{syst}) =$   
1555  $68^{+30}_{-25}$  pb for 3 jets, where the expected cross-section is  $\sigma_t = 65^{+30}_{-24}$  pb. Both results are  
1556 consistent with the standard model value within two standard deviations and consistent with  
1557 each other within uncertainties.

1558 **10.2.1.2 Positively and Negatively Charged Single Top Quark t-channel Pro-**  
1559 **duction**

1560 One can also combine the four channels into a positive and negative lepton charge sam-  
1561 ple. Because the top quark decays to a W and b (and then the W decays to a lepton  
1562 on neutrino) without hadronizing, the charge information from the top quark is preserved  
1563 in the lepton. Therefore, the positively charged lepton channel measurement corresponds  
1564 to a measurement of the positively charged top quark portion of the t-channel single-top  
1565 cross-section. There is a separate theoretical prediction for the top and anti-top portions  
1566 of the cross-section, given in Section 2.3.2. The results of this measurement are  $\sigma_{t+} =$   
1567  $59^{+6}_{-6}(\text{stat})^{+17}_{-16}(\text{syst}) = 59^{+18}_{-16}$  pb for top (positive lepton charge), where the expected cross-  
1568 section is  $\sigma_{t+} = 42^{+14}_{-13}$  pb. The measurement is  $\sigma_{t-} = 33^{+5}_{-5}(\text{stat})^{+12}_{-11}(\text{syst}) = 33^{+13}_{-12}$  pb  
1569 for anti-top (negative lepton charge), where the expected cross-section is  $\sigma_{t-} = 23^{+10}_{-10}$  pb.

### **1570 10.2.1.3 Combined t-channel Production Cross-section Result**

1571 Finally, all four channels can be combined, and this is the final reported total cross-section re-  
1572 sult for this study. The observed t-channel single-top cross-section is  $\sigma_t = 92^{+7}_{-7}(\text{stat})^{+28}_{-25}(\text{syst}) =$   
1573  $92^{+29}_{-26}$  pb, where  $\sigma_t = 65^{+22}_{-20}$  pb is expected. This is consistent with the standard model  
1574 and within two standard deviations of the theoretical single-top t-channel cross-section.

1575 Table 10.6 shows a breakdown of the systematic uncertainties and their contribution  
1576 to the expected cross-section measurement for the combination of all four channels and  
1577 Table 10.7 shows the same but for the observed data. The data statistical uncertainty is  
1578 much lower than the systematic uncertainties, meaning that this cross-section measurement  
1579 is dominated by systematic uncertainties. The largest uncertainties for this analysis are  
1580 ISR/FSR, shower/generator, and b-tagging uncertainties.

1581 The ISR/FSR uncertainty may decrease in future analyses as this is studied further and  
1582 the level of variation required is better understood. The b-tagging uncertainty will also likely  
1583 improve in future analyses as more data are collected and the b-tagging efficiencies and scale  
1584 factors are better estimated. The shower/generator uncertainty is unlikely to change very  
1585 much until shower/generator programs are updated. On the other hand, the MC statistical  
1586 uncertainty will become more of an issue in future analyses. As the data statistics increase,  
1587 the number of MC events that must be generated increases. This means that the MC  
1588 statistical uncertainty will increase in future analyses unless they are altered to use looser  
1589 selections or faster MC generation methods.

Source	$\Delta\sigma/\sigma (\%)$
Data statistics	+10/-10
MC statistics	+6/-6
$b$ tagging scale factor	+13/-13
Mistag scale factor	+1/-1
Lepton scale factor	+3/-3
Lepton efficiencies	+1/-1
Jet energy scale	+2/-3
Jet energy resolution	+2/-2
Jet reconstruction	+1/-1
$W$ shape	+1/-1
$W_{jj}$ normalization	+1/-1
$W c, cc, bb$ normalization	+2/-2
$W$ 3 jet normalization	+2/-2
$\eta$ reweighting	+8/-5
$E_T^{\text{miss}}$	+1/-2
$E_T^{\text{miss}}$ pileup	+1/-2
LAr	+1/-1
PDF	+5/-5
Generator	+8/-8
Shower	+12/-11
ISR/FSR	+21/-19
Theory cross-section	+7/-7
Multijets	+3/-3
Luminosity	+5/-5
Total Systematics	+33/-29
Total	+34/-31

Table 10.6: Systematic uncertainties for the expected  $t$ -channel cross-section measurement, where the final line includes all systematic uncertainties and the data statistical uncertainty.

Source	$\Delta\sigma/\sigma (\%)$
Data statistics	+8/-8
MC statistics	+4/-4
$b$ tagging scale factor	+12/-12
Mistag scale factor	+1/-1
Lepton scale factor	+3/-3
Lepton efficiencies	+2/-2
Jet energy scale	+2/-3
Jet energy resolution	+2/-2
Jet reconstruction	+1/-1
$W$ shape	+1/-1
$W_{jj}$ normalization	+1/-1
$W c, cc, bb$ normalization	+2/-2
$W$ 3 jet normalization	+2/-2
$\eta$ reweighting	+7/-5
$E_T^{\text{miss}}$	+1/-2
$E_T^{\text{miss}}$ pileup	+1/-1
LAr	+1/-1
PDF	+4/-4
Generator	+7/-7
Shower	+11/-11
ISR/FSR	+19/-18
Theory cross-section	+5/-5
Multijets	+2/-2
Luminosity	+4/-4
Total Systematics	+30/-27
Total	+31/-28

Table 10.7: Systematic uncertainties for the observed  $t$ -channel cross-section measurement, where the final line includes all systematic uncertainties and the data statistical uncertainty.

1590 **10.2.2 Estimate of  $|V_L|$**

1591 As discussed in Section 2.2, the CKM matrix element  $|V_L|$  can be directly estimated from  
1592 t-channel single-top production using the ratio of the observed and standard model cross-  
1593 section. We may write (based on Equation 2.3), where  $\sigma$  is the cross-section, obs refers to  
1594 the observed value and sm refers to the standard model:

$$|V_{L,obs}| = \sqrt{\frac{\sigma_{obs}}{\sigma_{sm}}} |V_{L,sm}| \quad (10.1)$$

1595 or, with  $|V_{L,sm}| = |V_{tb}| = 1$  from the standard model we obtain,

$$|V_{L,obs}| = \sqrt{\frac{\sigma_{obs}}{\sigma_{sm}}} \quad (10.2)$$

1596 Performing the calculation to propagate the uncertainties gives

$$\delta_{V_{L,obs}} = \frac{V_{L,obs}}{2} \sqrt{\left(\frac{\delta_{obs}}{\sigma_{obs}}\right)^2 + \left(\frac{\delta_{sm}}{\sigma_{sm}}\right)^2} \quad (10.3)$$

1597 where  $\delta$  refers to the uncertainty. Thus, we obtain a value of  $|V_{L,obs}| = 1.19^{+0.20}_{-0.18}$  for  
1598 the main, four channel combination. In this case we used 10% for the theoretical cross-  
1599 section uncertainty, as was done for the other single-top processes during the cross-section  
1600 determination. This result is consistent with the standard model value of 1.0 (and thus being  
1601 simply the standard model  $|V_{tb}|$ ) within two standard deviations.

1602 It is also possible to determine a lower 95% confidence level limit on the  $|V_{tb}|$  value,  
1603 assuming a standard model upper value of 1. We form a Gaussian with a mean of 1.42 and  
1604 use the uncertainty given for the combined result. We integrate from 1 towards 0, taking

<sub>1605</sub> the limit to be the point where 95% of the curve has been integrated. With this standard  
<sub>1606</sub> model assumption, we find  $|V_{tb}| > 0.67$  observed.

### <sub>1607</sub> 10.2.3 Comment on Significance

<sub>1608</sub> It is fairly straightforward to determine a significance using a frequentist tool like BILL.  
<sub>1609</sub> One simply determines the likelihood of a background-only hypothesis fluctuating to imitate  
<sub>1610</sub> the signal hypothesis by generating many, many pseudo-experiments and seeing how likely  
<sub>1611</sub> this is to happen. Pseudo-experiments are generated as described in Section 10.2.1. The  
<sub>1612</sub> calculation is done by determining the value  $-2\ln(Q)$ , the test statistic (also known as the  
<sub>1613</sub> log-likelihood ratio or LLR). A fit is done for a given ensemble to determine how likely it  
<sub>1614</sub> is that the ensemble satisfies the background only ( $H_B$ ) or signal plus background ( $H_{SB}$ )  
<sub>1615</sub> hypotheses. The ratio of the probabilities is the Q in the LLR value:

$$Q = \frac{p(H_{SB})}{p(H_B)} \quad (10.4)$$

<sub>1616</sub> The significance is determined by seeing how many background-only pseudo-experiments  
<sub>1617</sub> have a LLR value that is greater than the mean of the pseudo-experiments which assume  
<sub>1618</sub> a signal plus background (standard model) hypothesis. This is done by finding the mean  
<sub>1619</sub> of the signal plus background LLR distribution and finding how many background only  
<sub>1620</sub> ensembles have LLR values above this mean, compared to the total number of background  
<sub>1621</sub> only ensembles. In this way, the probability of the background fluctuating to look like the  
<sub>1622</sub> signal, and thus the significance, can be determined.

<sub>1623</sub> The difficulty with this method is that around and especially above the 5 sigma sig-  
<sub>1624</sub> nificance level (the level at which observation is typically claimed in high energy physics),

1625 the number of pseudo-experiments needed can become very, very large (10 million to 100  
1626 million or more). For this dissertation, the result has been shown to be above 5 sigma pre-  
1627 viously [8, 9] with less data and larger systematic uncertainties, so we do not repeat this for  
1628 the main result. We do demonstrate the individual expected results for two channels below  
1629 5 sigma, the 3 jet and negative charge channels. In high energy physics, discovery requires  
1630 a 5 sigma significance, or a p-value (probability) of the background fluctuating to look like  
1631 signal of 0.0000006. Evidence requires 3 sigma significance, or a p-value of 0.003.

1632 The LLR distributions for the three jet and negative charge channels are shown in Fig-  
1633 ure 10.2. About 800000 pseudo-data sets were created in each case. For the three jet channel,  
1634 the expected significance is 3.8 sigma with a p-value of background fluctuating to look like a  
1635 standard model signal of  $8 \times 10^{-5}$ . For the minus charge channel, the expected significance  
1636 is 4.1 sigma with a p-value of background fluctuating to look like a standard model signal of  
1637  $2 \times 10^{-5}$ .

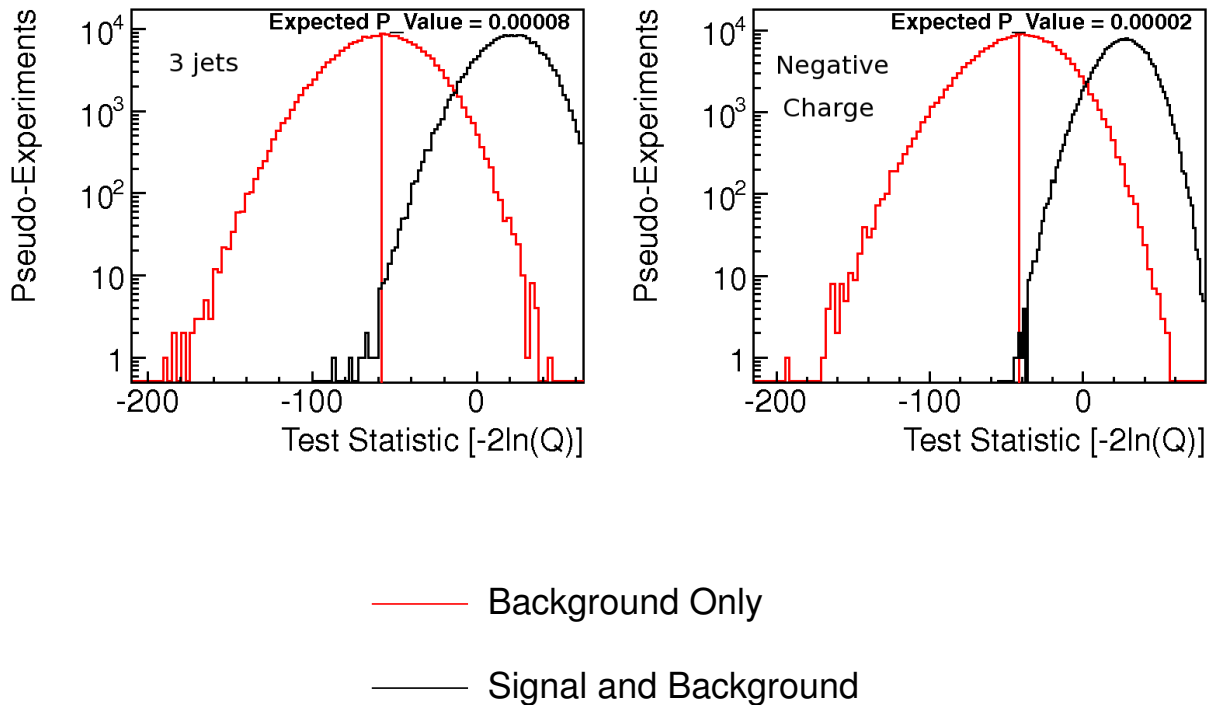


Figure 10.2: Distribution used to determine the expected significance for the 3 jet channel (all lepton charges are allowed) and negative charge channel (2 and 3 jets allowed). The two curves are ensembles with and without the assumption of a standard model signal. The vertical line shows the mean of the standard model signal and background distribution.

# <sup>1638</sup> Chapter 11

## <sup>1639</sup> Conclusions and Implications for

## <sup>1640</sup> Future Work

<sup>1641</sup> In this dissertation we have discussed the main details involved in the estimate of the t-

<sup>1642</sup> channel single-top cross-section using ATLAS data. The ATLAS detector is a multi-purpose

<sup>1643</sup> detector located at the LHC at CERN and  $1.04 \text{ fb}^{-1}$  of data from the 2011 data taking run

<sup>1644</sup> was used, with a 7 TeV center-of-mass energy. The data were processed to assign energy

<sup>1645</sup> and tracks to reconstructed particles like those in a Monte Carlo simulation. Selections

<sup>1646</sup> were applied to both the data and MC to reduce the signal and background ratio to a more

<sup>1647</sup> reasonable level of about 10%. At this point, a cut-based analysis was performed, where four

<sup>1648</sup> additional selections for four orthogonal channels based on jet number and lepton charge were

<sup>1649</sup> chosen and applied. A fit and frequentist technique was then used to determine the cross-

<sup>1650</sup> section and its uncertainty. Separate measurements of the top and anti-top cross-section

<sup>1651</sup> were performed, giving observed results of  $\sigma_{t+} = 59^{+18}_{-16} \text{ pb}$  for top (positive lepton charge)

<sup>1652</sup> and  $\sigma_{t-} = 33^{+13}_{-12} \text{ pb}$  for anti-top (minus lepton charge). The final result included all four

<sub>1653</sub> channels and was  $\sigma_t = 92^{+29}_{-26}$  pb, where  $\sigma_t = 65^{+22}_{-20}$  pb was expected.

<sub>1654</sub> Future studies will likely benefit from additional channels beyond the four used here  
<sub>1655</sub> and perhaps tighter selection thresholds, made possible by additional data. For instance  
<sub>1656</sub> one could examine the 4 jet bin. It is heavily contaminated with  $t\bar{t}$  events, but it may be  
<sub>1657</sub> possible to remove enough of these events to be worthwhile. Additionally, it is possible to  
<sub>1658</sub> have a 3 jet event with 2 jets b-tagged and this is another possible kinematic region, though  
<sub>1659</sub> again heavily contaminated with  $t\bar{t}$  background. In this study, the three jet bin was used,  
<sub>1660</sub> which also suffers from a large  $t\bar{t}$  background. The invariant mass of all three jets was a  
<sub>1661</sub> very effective selection for removing a large portion of this background while still retaining  
<sub>1662</sub> a reasonable amount of signal events. Future analyses may want to consider selections using  
<sub>1663</sub> the invariant mass of all jets except the jet that best reconstructs the top mass (using a  
<sub>1664</sub> lepton and neutrino) for the four jet bin. The remaining three jets used in the invariant  
<sub>1665</sub> mass are likely from the decay of the second top quark. Similarly, the 3 jet 2 btag selected  
<sub>1666</sub> channel could benefit from a selection based on the invariant mass of all three jets, or just  
<sub>1667</sub> the invariant mass of all jets except the jet that best reconstructs the top mass. The choice  
<sub>1668</sub> here is not as obvious, as some jets in  $t\bar{t}$  may have been missed or have a low  $p_T$ , but  
<sub>1669</sub> both options could be useful. With these invariant mass selections, in addition to selections  
<sub>1670</sub> related to the reconstructed top mass and untagged jet  $|\eta|$ , it may be possible to perform an  
<sub>1671</sub> analysis to measure single-top  $t$ -channel in these regions, with S/B ratios of 0.5 or more in  
<sub>1672</sub> these channels, with these types of selections, as demonstrated in Appendix C.

<sub>1673</sub> Although modern particle physics is more difficult than smashing stones together, it is  
<sub>1674</sub> nevertheless rewarding, as new information about the universe we live in is discerned from  
<sub>1675</sub> these studies. We know so much about the physical universe in this modern era and yet

<sub>1676</sub> there is still much to be done and to learn. In this case, we have made a new measurement  
<sub>1677</sub> of a standard model process only recently observed. Future studies will likely reduce these  
<sub>1678</sub> uncertainties and extract new information about properties of the top quark. It is a very  
<sub>1679</sub> exciting time to contribute to the understanding of single-top production, as we just start  
<sub>1680</sub> to scratch the surface of what can be done with studies of this process.

## BIBLIOGRAPHY

# BIBLIOGRAPHY

- 1682 [1] CDF Collaboration, F. Abe et al., *Observation of top quark production in  $p\bar{p}$  collisions*  
1683 *with the Collider Detector at Fermilab*, Phys. Rev. Lett. **74** (1995) 2626.
- 1684 [2] D0 Collaboration, S. Abachi et al., *Observation of the top quark*, Phys. Rev. Lett. **74**  
1685 (1995) 2632–2637, [arXiv:hep-ex/9503003](https://arxiv.org/abs/hep-ex/9503003).
- 1686 [3] CDF and D0 Collaboration, Tevatron Electroweak Working Group, *Combination of*  
1687 *CDF and D0 Measurements of the Single Top Production Cross Section*,  
1688 [arXiv:0908.2171 \[hep-ex\]](https://arxiv.org/abs/0908.2171).
- 1689 [4] D0 Collaboration, V. M. Abazov et al., *Observation of Single Top-Quark Production*,  
1690 Phys. Rev. Lett. **103** (2009) 092001, [arXiv:0903.0850 \[hep-ex\]](https://arxiv.org/abs/0903.0850).
- 1691 [5] CDF Collaboration, T. Aaltonen et al., *First Observation of Electroweak Single Top*  
1692 *Quark Production*, Phys. Rev. Lett. **103** (2009) 092002, [arXiv:0903.0885 \[hep-ex\]](https://arxiv.org/abs/0903.0885).
- 1693 [6] D0 Collaboration, V. M. Abazov et al., *Model-independent measurement of t-channel*  
1694 *single top quark production in  $p\bar{p}$  collisions at  $\sqrt{s} = 1.96$  TeV*, Physics Letters B **705**  
1695 (2011) no. 4, 313 – 319.
- 1696 [7] CMS Collaboration, S. Chatrchyan et al., *Measurement of the t-Channel Single Top*  
1697 *Quark Production Cross Section in pp Collisions at  $\sqrt{s} = 7$  TeV*, Phys. Rev. Lett. **107**  
1698 (2011) 091802.
- 1699 [8] ATLAS Collaboration, *Observation of t-Channel Single Top-Quark Production in pp*  
1700 *Collisions at  $\sqrt{s} = 7$  TeV with the ATLAS detector*, ATLAS-CONF-2011-088 (2011) .

- 1701 [9] ATLAS Collaboration, *Measurement of the  $t$ -channel Single Top-Quark Production*  
 1702 *Cross Section in 0.70  $\text{fb}^{-1}$  of  $pp$  Collisions at  $\sqrt{s} = 7 \text{ TeV}$  with the ATLAS detector*,  
 1703 ATLAS-CONF-2011-101 (2011) .
- 1704 [10] A. W. Hendry and D. B. Lichtenberg, *The quark model*, Reports on Progress in  
 1705 Physics **41** (1978) no. 11, 1707.
- 1706 [11] K. Nakamura et al., (*Particle Data Group*), J. Phys. G **37** (2010) 075021.
- 1707 [12] D. Griffiths, *Introduction to Elementary Particles*. Wiley-VCH Verlag GmbH & Co.  
 1708 KGaA, Weinheim, 2004.
- 1709 [13] F. Halzen and A. D. Martin, *Quarks and Leptons: An Introductory Course in Modern*  
 1710 *Particle Physics*. John Wiley & Sons, 1984.
- 1711 [14] L. H. Orr and J. L. Rosner, *Comparison of top quark hadronization and decay rates*,  
 1712 Physics Letters B **246** (1990) no. 1-2, 221 – 225.
- 1713 [15] N. Cabibbo, *Unitary Symmetry and Leptonic Decays*, Phys. Rev. Lett. **10** (1963) .
- 1714 [16] M. Kobayashi and T. Maskawa, *CP-Violation in the Renormalizable Theory of Weak*  
 1715 *Interaction*, Prog. Theor. Phys. **49** (1973) .
- 1716 [17] J. Aguilar-Saavedra, *A minimal set of top anomalous couplings*, Nuclear Physics B  
 1717 **812** (2009) no. 1-2, 181 – 204.
- 1718 [18] G. L. Kane, G. A. Ladinsky, and C. P. Yuan, *Using the top quark for testing*  
 1719 *standard-model polarization and CP predictions*, Phys. Rev. D **45** (1992) 124–141.
- 1720 [19] N. Kidonakis, *NNLL resummation for  $s$ -channel single top quark production*, Phys.  
 1721 Rev. **D81** (2010) 054028, arXiv:1001.5034 [hep-ph].
- 1722 [20] N. Kidonakis, *Two-loop soft anomalous dimensions for single top quark associated*  
 1723 *production with a  $W$ - or  $H$ -*, Phys. Rev. **D82** (2010) 054018, arXiv:1005.4451  
 1724 [hep-ph].
- 1725 [21] N. Kidonakis, *Next-to-next-to-leading-order collinear and soft gluon corrections for*  
 1726  *$t$ -channel single top quark production*, Phys. Rev. **D83** (2011) 091503,  
 1727 arXiv:1103.2792 [hep-ph].

- <sub>1728</sub> [22] G. Bertone, D. Hooper, and J. Silk, *Particle dark matter: evidence, candidates and constraints*, Physics Reports **405** (2005) no. 5-6, 279 – 390.
- <sub>1730</sub> [23] M. Kowalski et al., *Improved Cosmological Constraints from New, Old, and Combined Supernova Data Sets*, The Astrophysical Journal **686** (2008) no. 2, 749.
- <sub>1732</sub> [24] N. Jarosik et al., *Seven-year Wilkinson Microwave Anisotropy Probe (WMAP) Observations: Sky Maps, Systematic Errors, and Basic Results*, The Astrophysical Journal Supplement Series **192** (2011) no. 2, 14.
- <sub>1735</sub> [25] L. Evans and P. Bryant, *LHC Machine*, JINST **3** (2008) S08001.
- <sub>1736</sub> [26] ATLAS Collaboration, *Luminosity Determination in pp Collisions at  $\sqrt{s} = 7 \text{ TeV}$  using the ATLAS Detector in 2011*, <http://cdsweb.cern.ch/record/1376384>.
- <sub>1738</sub> [27] V. Kain, B. Goddard, B. Holzer, J. Jowett, M. Meddahi, T. Mertens, and F. Roncarolo, *Transverse emittance preservation through the LHC cycle*, Tech. Rep. CERN-ATS-2011-056, CERN, Geneva, Sep, 2011.
- <sub>1741</sub> [28] J.-P. Koutchouk and G. Sterbini, *An Early Beam Separation Scheme for the LHC Luminosity Upgrade*, Proceedings of EPAC, Edinburgh, Scotland (2006) .
- <sub>1743</sub> [29] ATLAS Collaboration,  
<https://twiki.cern.ch/twiki/bin/view/AtlasPublic/LuminosityPublicResults>, (2011) .
- <sub>1745</sub> [30] ATLAS Collaboration, *The ATLAS Experiment at the CERN Large Hadron Collider*, JINST **3** (2008) S08003.
- <sub>1747</sub> [31] ATLAS Collaboration, <http://atlas.ch/photos/detector-site-surface.html>, (2011) .
- <sub>1748</sub> [32] ATLAS Collaboration, G. Aad et al., *Electron performance measurements with the ATLAS detector using the 2010 LHC proton-proton collision data*, arXiv:1110.3174 [hep-ex]. submitted to Eur. Phys. J. C.
- <sub>1751</sub> [33] ATLAS Collaboration, G. Aad et al., *Performance of the ATLAS Trigger System in 2010*, The European Physical Journal C - Particles and Fields **72** (2012) 1–61. 10.1140/epjc/s10052-011-1849-1.
- <sub>1754</sub> [34] ATLAS Collaboration, *Muon reconstruction efficiency in reprocessed 2010 LHC proton-proton collision data recorded with the ATLAS detector*, Tech. Rep. ATLAS-CONF-2011-063, CERN, Geneva, Apr, 2011.

- 1757 [35] ATLAS Collaboration, G. Aad et al., *Measurement of the*  
 1758  *$W \rightarrow l\nu$  and  $Z/\gamma \rightarrow ll$  production cross sections in proton-proton collisions*  
 1759 *at  $\sqrt{s} = 7$  TeV with the ATLAS detector*, JHEP **1012** (2010) 060, arXiv:1010.2130  
 1760 [**hep-ex**].  
  
 1761 [36] M. Cacciari, G. P. Salam, and G. Soyez, *The anti-  $k_t$  jet clustering algorithm*, Journal  
 1762 of High Energy Physics **2008** (2008) no. 04, 063.  
  
 1763 [37] ATLAS Collaboration, *Jet energy measurement with the ATLAS detector in*  
 1764 *proton-proton collisions at  $\sqrt{s} = 7$  TeV*, arXiv:1112.6426 [**hep-ex**]. submitted  
 1765 to European Physical Journal C.  
  
 1766 [38] ATLAS Collaboration, *Jet energy scale and its systematic uncertainty in*  
 1767 *proton-proton collisions at  $\sqrt{s} = 7$  TeV in ATLAS 2010 data*, Tech. Rep.  
 1768 ATLAS-CONF-2011-032, CERN, Geneva, Mar, 2011.  
  
 1769 [39] ATLAS Collaboration, G. Aad et al., *Jet energy resolution and selection efficiency*  
 1770 *relative to track jets from in-situ techniques with the ATLAS Detector Using*  
 1771 *Proton-Proton Collisions at a Center of Mass Energy  $\sqrt{s} = 7$  TeV*, Tech. Rep.  
 1772 ATLAS-CONF-2010-054, CERN, Geneva, Jul, 2010.  
  
 1773 [40] W. Lampl et al., *Calorimeter Clustering Algorithms: Description and Performance*,  
 1774 Tech. Rep. ATL-LARG-PUB-2008-002. ATL-COM-LARG-2008-003, CERN, Geneva,  
 1775 Apr, 2008.  
  
 1776 [41] ATLAS Collaboration, *Event Display, b-jet*, Tech. Rep.  
 1777 <https://twiki.cern.ch/twiki/bin/view/AtlasPublic/EventDisplayPublicResults>, CERN,  
 1778 Geneva, 2011.  
  
 1779 [42] ATLAS Collaboration, *Commissioning of the ATLAS high-performance b-tagging*  
 1780 *algorithms in the 7 TeV collision data*, Tech. Rep. ATLAS-CONF-2011-102, CERN,  
 1781 Geneva, Jul, 2011.  
  
 1782 [43] R. E. Kalman, *A New Approach to Linear Filtering and Prediction Problems*,  
 1783 Transactions of the ASME–Journal of Basic Engineering **82** (1960) no. Series D, 35–45.  
  
 1784 [44] ATLAS Collaboration, G. Aad and others, *Performance of missing transverse*  
 1785 *momentum reconstruction in proton-proton collisions at  $\sqrt{s} = 7$  TeV with ATLAS*,  
 1786 *The European Physical Journal C - Particles and Fields* **72** (2012) 1–35.  
 1787 10.1140/epjc/s10052-011-1844-6.

- 1788 [45] T. Sjostrand, S. Mrenna, and P. Skands, *PYTHIA Generator version 6.418*, JHEP **05**  
 1789 (2006) 026.
- 1790 [46] G. Corcella et al., *HERWIG 6.5: an event generator for Hadron Emission Reactions*  
 1791 *With Interfering Gluons (including supersymmetric processes)*, JHEP **01** (2001) 010,  
 1792 arXiv:hep-ph/0011363.
- 1793 [47] J. M. Butterworth, J. R. Forshaw, and M. H. Seymour, *Multiparton interactions in*  
 1794 *photoproduction at HERA*, Z. Phys. C **72** (1996) 637–646, arXiv:hep-ph/9601371.
- 1795 [48] J. Pumplin et al, *New generation of parton distributions with uncertainties from global*  
 1796 *QCD analysis*, JHEP **07** (2002) 012, arXiv:hep-ph/0201195.
- 1797 [49] B. P. Kersevan and R. W. Elzbieta, *The Monte Carlo Event Generator AcerMC*  
 1798 *version 3.5 with interfaces to PYTHIA 6.4, HERWIG 6.5 and ARIADNE 4.1*,  
 1799 hep-ph/0405247 (2008) .
- 1800 [50] B. P. Kersevan and I. Hinchliffe, *A Consistent prescription for the production involving*  
 1801 *massive quarks in hadron collisions*, JHEP **0609** (2006) 033, arXiv:hep-ph/0603068  
 1802 [hep-ph].
- 1803 [51] S. Frixione, B. R. Webber, and P. Nason, *MC@NLO Generator version 3.4*,  
 1804 hep-ph/0204244 and hep-ph/0305252 (2002) .
- 1805 [52] M. L. Mangano, M. Moretti, F. Piccinini, R. Pittau, and A. D. Polosa, *ALPGEN, a*  
 1806 *generator for hard multiparton processes in hadronic collisions*, JHEP **07** (2003) 001,  
 1807 arXiv:hep-ph/0206293.
- 1808 [53] ATLAS Collaboration, G. Aad and others, *The ATLAS Simulation Infrastructure*,  
 1809 The European Physical Journal C - Particles and Fields **70** (2010) 823–874.  
 1810 10.1140/epjc/s10052-010-1429-9.
- 1811 [54] S. Agostinelli et al., *Geant4- a simulation toolkit*, Nuclear Instruments and Methods in  
 1812 Physics Research Section A: Accelerators, Spectrometers, Detectors and Associated  
 1813 Equipment **506** (2003) no. 3, 250 – 303.
- 1814 [55] ATLAS Collaboration, *A measurement of the ATLAS muon reconstruction and trigger*  
 1815 *efficiency using J/psi decays*, Tech. Rep. ATLAS-CONF-2011-021, CERN, Geneva,  
 1816 Mar, 2011.

- 1817 [56] ATLAS Collaboration, *Calibrating the b-Tag Efficiency and Mistag Rate in 35 pb<sup>-1</sup> of*  
 1818 *Data with the ATLAS Detector*, Tech. Rep. ATLAS-CONF-2011-089, CERN, Geneva,  
 1819 Jun, 2011.
- 1820 [57] ATLAS Collaboration, *Muon Momentum Resolution in First Pass Reconstruction of*  
 1821 *pp Collision Data Recorded by ATLAS in 2010*, Tech. Rep. ATLAS-CONF-2011-046,  
 1822 CERN, Geneva, Mar, 2011.
- 1823 [58] G. Romeo, A. Schwartzman, R. Piegai, T. Carli, and R. Teuscher, *Jet Energy*  
 1824 *Resolution from In-situ Techniques with the ATLAS Detector Using Proton-Proton*  
 1825 *Collisions at a Center of Mass Energy  $\sqrt{s} = 7 \text{ TeV}$* , Tech. Rep.  
 1826 ATL-COM-PHYS-2011-240, CERN, Geneva, Mar, 2011.
- 1827 [59] ATLAS Collaboration, *Data-Quality Requirements and Event Cleaning for Jets and*  
 1828 *Missing Transverse Energy Reconstruction with the ATLAS Detector in Proton-Proton*  
 1829 *Collisions at a Center-of-Mass Energy of  $\text{sqrt}s = 7 \text{ TeV}$* , Tech. Rep.  
 1830 ATLAS-CONF-2010-038, CERN, Geneva, Jul, 2010.
- 1831 [60] ATLAS Collaboration,  
 1832 <https://twiki.cern.ch/twiki/bin/view/AtlasProtected/HowToCleanJets2011>, (2011) .
- 1833 [61] ATLAS Collaboration, *Measurement of the top quark-pair production cross section*  
 1834 *with ATLAS in pp collisions at  $\sqrt{s} = 7 \text{ TeV}$* , The European Physical Journal C -  
 1835 Particles and Fields **71** (2011) 1–36. 10.1140/epjc/s10052-011-1577-6.
- 1836 [62] ATLAS Collaboration, *Searches for Single Top-Quark Production with the ATLAS*  
 1837 *Detector in pp Collisions at  $\text{sqrt}(s) = 7 \text{ TeV}$* , Tech. Rep. ATLAS-CONF-2011-027,  
 1838 CERN, Geneva, Mar, 2011.
- 1839 [63] R. D. Cousins, J. T. Linnemann, and J. Tucker, *Evaluation of three methods for*  
 1840 *calculating statistical significance when incorporating a systematic uncertainty into a*  
 1841 *test of the background-only hypothesis for a Poisson process*, Nucl. Instrum. Methods  
 1842 Phys. Res., A **595** (2008) 480.
- 1843 [64] W. Press et al., *Numerical Recipes in C, 2nd ed.* Cambridge, 1992.
- 1844 [65] U. Felzmann, <https://twiki.cern.ch/twiki/bin/view/Main/AlpgenFAQ>, (2008) .
- 1845 [66] R. D. Ball, L. Del Debbio, S. Forte, A. Guffanti, J. I. Latorre, et al., *A first unbiased*  
 1846 *global NLO determination of parton distributions and their uncertainties*, Nucl.Phys.  
 1847 B**838** (2010) 136–206, arXiv:1002.4407 [hep-ph].

- 1848 [67] F. Demartin, S. Forte, E. Mariani, J. Rojo, and A. Vicini, *The impact of PDF and  $\alpha_S$*   
 1849 *uncertainties on Higgs Production in gluon fusion at hadron colliders*, Phys.Rev. **D82**  
 1850 (2010) 014002, arXiv:1004.0962 [hep-ph].
- 1851 [68] A. Martin, W. Stirling, R. Thorne, and G. Watt, *Parton distributions for the LHC*,  
 1852 The European Physical Journal C - Particles and Fields **63** (2009) 189–285.  
 1853 10.1140/epjc/s10052-009-1072-5.
- 1854 [69] A. Martin, W. Stirling, R. Thorne, and G. Watt, *Uncertainties on  $\alpha_S$  in global PDF*  
 1855 *analyses and implications for predicted hadronic cross sections*, The European Physical  
 1856 Journal C - Particles and Fields **64** (2009) 653–680. 10.1140/epjc/s10052-009-1164-2.
- 1857 [70] J. M. Campbell and R. Ellis, *MCFM for the Tevatron and the LHC*, Nuclear Physics  
 1858 B - Proceedings Supplements **205-206** (2010) no. 0, 10 – 15. Loops and Legs in  
 1859 Quantum Field Theory, Proceedings of the 10th DESY Workshop on Elementary  
 1860 Particle Theory.
- 1861 [71] P. Nason, *A new method for combining NLO QCD computations with parton shower*  
 1862 *simulations*, JHEP 11(2004)-040, hep-ph/0409146 (2004) .
- 1863 [72] S. Frixione, P. Nason, et al., *Positive weight next-to-leading-order Monte Carlo*, JHEP  
 1864 11(2007)-126 and JHEP 09(2007)111, hep-ph/07092092 and hep-ph/07073088 (2007) .
- 1865 [73] W. Wagner. Private communication, 2011.
- 1866 [74] L. Lyons, *Statistics for nuclear and particle physicists*. Cambridge University Press,  
 1867 1986.
- 1868 [75] L. Lyons, D. Gibaut, and P. Clifford, *How to combine correlated estimates of a single*  
 1869 *physical quantity*, Nuclear Instruments and Methods in Physics Research Section A:  
 1870 Accelerators, Spectrometers, Detectors and Associated Equipment **270** (1988) no. 1,  
 1871 110 – 117.
- 1872 [76] B. P. Roe et al., *Boosted Decision Trees as an Alternative to Artificial Neural*  
 1873 *Networks for Particle Identification*, physics/0408124v2 (2004) .
- 1874 [77] I. Narsky, *StatPatternRecognition: A C++ Package for Statistical Analysis of High*  
 1875 *Energy Physics Data*, physics/0507143 (2005) .
- 1876 [78] F. J. Massey, *The Kolmogorov-Smirnov Test for Goodness of Fit*, Journal of the  
 1877 American Statistical Association **46** (1951) no. 253, 68–78.

# Appendices

<sub>1879</sub> **Appendix A**

<sub>1880</sub> **Data Based Cross-check of**

<sub>1881</sub>  **$t\bar{t}$  Background**

<sub>1882</sub> In the main text we have discussed the data-based estimation of the multijets and W+jets  
<sub>1883</sub> background processes. However, there is another large background,  $t\bar{t}$ , where the theoretical  
<sub>1884</sub> cross-section was used for the normalization. It is also possible to do a data-based estimate  
<sub>1885</sub> of this background. In this section, we review one straight-forward way to do this estimate.

<sub>1886</sub> The  $t\bar{t}$  estimate discussed here is not used in the analysis described in the main text, but  
<sub>1887</sub> instead is intended as a cross-check of the value used (1.0) and its uncertainty.

<sub>1888</sub> To determine the  $t\bar{t}$  background, we define orthogonal off-signal regions (as we did for the  
<sub>1889</sub> W+jets estimate). All preselection requirements except for the number of jets and b-tagged  
<sub>1890</sub> jets selections are applied. We also require the total t-channel yield to be < 6% of the total,  
<sub>1891</sub> and apply as few selections as possible beyond the preselection (with different numbers of  
<sub>1892</sub> jets and b-tagged jets). Two  $t\bar{t}$  dominated selections are defined as the number of jets equal  
<sub>1893</sub> to four or more with 1 b-tagged jet, and the 2 b-tagged jets selection with at least 2 jets.

1894 Both of these regions are also discussed as potential signal regions in Section C, so if this  
 1895 is done, the regions used for signal determination would need to be removed, just as the 2  
 1896 jet signal kinematic region was removed from the W+jets estimate. Additionally, the 3 jet  
 1897 region is considered but this region has a relatively large ( 8%) portion of t-channel single-  
 1898 top events (hence its use as a signal channel) relative to the other  $t\bar{t}$  determination regions.  
 1899 In this case, an additional selection must be introduced to control the amount of t-channel  
 1900 and to exclude the signal region. Here, we choose to require the reconstructed top mass to  
 1901 be  $> 210$  GeV. This removes single-top events, which are more likely to have the b-quark,  
 1902 lepton, and missing energy associated with a top quark all correctly identified and thus an  
 1903 invariant mass of these particles closer to the top quark mass value.

1904 We also select channels based on the event having a muon or electron as the selected  
 1905 lepton. Thus we have 6 different channels in total, which are each of the following selections  
 1906 with a muon selection or electron selection:

- 1907 \* 2 b-tagged jets, at least 2 jets
- 1908 \* 1 b-tagged jet, at least 4 jets
- 1909 \* 1 b-tagged jet, exactly 3 jets,  $M_{top}(l\nu b) > 210$  GeV

1910 These channels are all orthogonal to each other. We can consider each result from these  
 1911 six channels as a separate experiment and combine them. First, we calculate a scale factor.  
 1912 This is defined as:

$$SF_{t\bar{t}} = \frac{\text{Data} - \text{MC(not } t\bar{t})}{\text{MC}(t\bar{t})} \quad (\text{A.1})$$

1913 If the data and the Monte Carlo were to agree exactly, then the  $t\bar{t}$  SF woulst be 1.0. To  
 1914 find the combined statistical uncertainty for the channels, we follow the method discussed

by Lyons [74, 75]. The statistical uncertainty is written as  $\sigma$ , where the square of this value  
 is the variance ( $\sigma^2$ ). This  $\sigma$  should not be confused with the cross-section. The combination  
 is found as follows, using  $i$  for the different channels:

$$\frac{1}{\sigma_{\text{tot}}^2} = \sum \frac{1}{\sigma_i^2} \quad (\text{A.2})$$

The scale factors themselves are also combined for the different channels as discussed by  
 Lyons. We weight each channel by the inverse of the statistical uncertainty squared. The  
 combination of scale factors is done as follows, where SF is the scale factor. Notice the  
 denominator is just  $\frac{1}{\sigma_{\text{tot}}^2}$  from Equation A.2:

$$SF_{\text{tot}} = \frac{\sum \frac{SF_i}{\sigma_i^2}}{\sum \frac{1}{\sigma_i^2}} \quad (\text{A.3})$$

To determine the systematic uncertainties for each channel, the SF is estimated using  
 MC values shifted due to a given uncertainty. For a given systematic uncertainty scenario,  
 the systematic-shifted SF are combined for each of the channels as in the nominal sample,  
 again using the same statistical uncertainty as a weight as in Equation A.3. The devia-  
 tion between the combined nominal SF and the combined uncertainty-shifted SF is then the  
 uncertainty for the combination due to the systematic in question. By determining the com-  
 bined systematic uncertainties this way, correlations between the channels can be properly  
 included. Finally, all of the systematic uncertainties and the data statistical uncertainty are  
 added in quadrature to obtain the overall uncertainty. The systematic uncertainties which  
 are considered are the b-tagging scale factor, mis-tagging scale factor, and jet energy scale.

<sup>1932</sup> Other systematic uncertainties are neglected for the purposes of this cross-check.

<sup>1933</sup> The multijet estimate for these channels is done using the values from Section 7.1 and  
<sup>1934</sup> multiplying by the fraction of multijets in the 3 jet bin and the desired bin to get the  
<sup>1935</sup> multijet total for the desired bin. The multijet estimate from the 3 jet bin is thus propagated  
<sup>1936</sup> into the other regions considered for the  $t\bar{t}$  scale factor estimate by assuming the multijets  
<sup>1937</sup> number of jets distribution is correct. For the 3 jet  $t\bar{t}$  region, which makes a selection on the  
<sup>1938</sup> reconstructed top mass, this same selection is simply applied to the 3 jets multijet sample.  
<sup>1939</sup> No new fits to the  $E_T^{\text{miss}}$  distribution are performed for the  $t\bar{t}$  scale factor estimtae. These  
<sup>1940</sup> values are approximate and the uncertainty related to propagating the multijet yield into  
different bins is neglected for this cross-check. The values are given in Table A.1.

Selection	Tagged events	
	e channel	$\mu$ channel
2 b-tag jets, $\geq 2$ jets	36.6	18.7
1 b-tag jet, $\geq 4$ jets	302.6	144.3
1 b-tag jet, 3 jets, $M_{top}(l\nu b) > 210$ GeV	78.4	35.7

Table A.1: Estimate of multijet yields for different selections, separated by lepton type.

<sup>1941</sup>

<sup>1942</sup> The W+jets estimate for these channels uses the data-based 3 jet bin heavy flavor frac-  
<sup>1943</sup> tions from Section 7.2 for the 1 b-tagged jet, exactly 3 jets,  $M_{top}(l\nu b) > 210$  GeV channel.  
<sup>1944</sup> This is because there is a selection used for this channel which impacts processes differently.  
<sup>1945</sup> For the other two channels, we use the W+jets data based normalizations appropriate for  
<sup>1946</sup> the number of jets in question, including a normalization of 0.75 for the 4 jets channel. The  
<sup>1947</sup> heavy flavor fractions do not have an impact on the scale factor determination for these two  
<sup>1948</sup> channels, as there are no selections beyond preselection applied.

<sup>1949</sup> The scale factors and their uncertainties for each of the six channels plus the combination  
<sup>1950</sup> of channels by lepton type, and then all channels, can be seen in Figure A.1. The statistical

1951    uncertainties are quite small, and if they are not smaller than the marker size, they are given  
1952    by colored portions of the vertical uncertainty line. Again, only the b-tagging scale factor,  
1953    mis-tagging scale factor, jet energy scale and data statistical uncertainties are included in  
1954    this cross-check. The electron and muon channel combinations give very similar values,  
1955     $SF_e = 1.10 \pm 0.02(\text{stat})^{+0.23}_{-0.14}(\text{syst}) = 1.10^{+0.23}_{-0.14}$  and  $SF_\mu = 1.13 \pm 0.02(\text{stat})^{+0.23}_{-0.15}(\text{syst}) =$   
1956     $1.13^{+0.23}_{-0.15}$  respectively. The final result from the combination of all six channels is  $SF =$   
1957     $1.12 \pm 0.01(\text{stat})^{+0.23}_{-0.15}(\text{syst}) = 1.12^{+0.23}_{-0.15}$ . This is consistent with a scale factor of 1.0 and  
1958    the uncertainty on the result is larger than the  $t\bar{t}$  theoretical cross-section uncertainty used  
1959    in the main text (approximately 10%, see Section 10.1). From this cross-check, it is clear  
1960    that the  $t\bar{t}$  estimate used in the t-channel single-top analysis is consistent with the data.

1961       Future analyses will want to include additional uncertainties such as ISR/FSR, shower  
1962    and generator uncertainties, as well as others used in the single-top t-channel cross-section  
1963    estimate. However, including these uncertainties in the current study would not change the  
1964    conclusion. As more data is taken, the uncertainties will likely become better understood  
1965    and have lower values than in this study. The data statistical uncertainty is already quite  
1966    low in this study, but the b-tagging scale factor uncertainty in particular is 14% for the  
1967    six channel combination, the dominant systematic uncertainty. If this uncertainty could be  
1968    reduced, it would have a significant impact on the precision of this scale factor estimate.

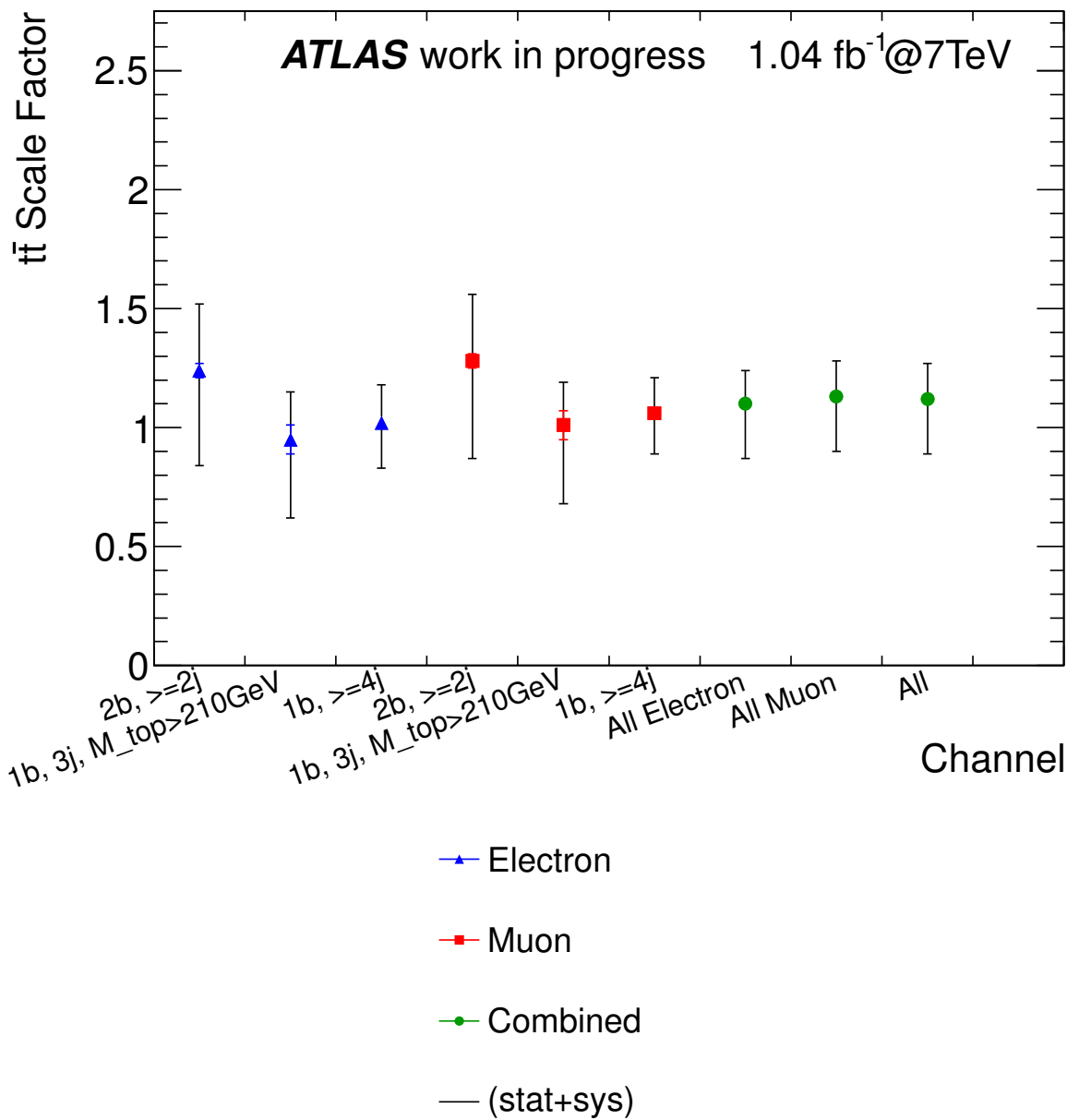


Figure A.1: Scale factors for  $t\bar{t}$  production using six separate channels, the combination of electron channels, the combination of muon channels, and the combination of all six channels. Statistical uncertainties are given by colored portions of the black lines unless the statistical uncertainties are so small as to be covered by the marker itself. The black line shows the data statistical, b-tagging scale factor, mis-tagging scale factor, and jet energy scale uncertainties combined. Other uncertainties are neglected in this cross-check.

# <sup>1969</sup> Appendix B

## <sup>1970</sup> Multivariate Analysis

<sup>1971</sup> Although this document has focused on a simple, cut-based analysis approach, there are more  
<sup>1972</sup> complicated analysis options. These include multivariate techniques such as boosted decision  
<sup>1973</sup> trees. Multivariate techniques use computer algorithms to determine several dimensions of  
<sup>1974</sup> selection sequences, making use of events which both pass and fail individual selections. The  
<sup>1975</sup> result is in an output related to the probability of an event being signal or background. In  
<sup>1976</sup> this chapter we review the boosted decision tree technique and then suggest options for future  
<sup>1977</sup> analyses using the variables from the main document and an additional set of variables. As  
<sup>1978</sup> this section is intended as suggestions for future work and another view point of the t-channel  
<sup>1979</sup> single-top analysis, only the large uncertainties from the cut-based analysis are considered.

### <sup>1980</sup> B.1 Boosted Decision Tree Overview

<sup>1981</sup> The boosted decision tree (BDT) [76] method has traditionally been used in single-top anal-  
<sup>1982</sup> yses [4, 5, 7] and this method is used here, as provided in a statistical package called Stat-  
<sup>1983</sup> PatternRecognition [77]. A boosted decision tree is based on a collection of decision trees,

1984 and an example of one is pictured in Figure B.1. A decision tree is a cut-flow diagram, where  
 1985 selections are applied that eventually result in sets of mostly signal or mostly background  
 1986 events. These final sets of events are the leaves or terminal nodes of the tree (each selection  
 1987 has an associated node that is not necessarily terminal). When a decision tree is applied  
 1988 to a new event, if this event passes background-like selections it is probably background,  
 1989 whereas if it passes signal-like selections it is probably signal. The ultimate output of the  
 1990 multivariate classifier indicates how likely it is that an event is background or signal. One  
 1991 can then take a simple cut on the classifier output, to select for high signal probability, or  
 1992 do a fitting technique to determine how much signal is present in the data.

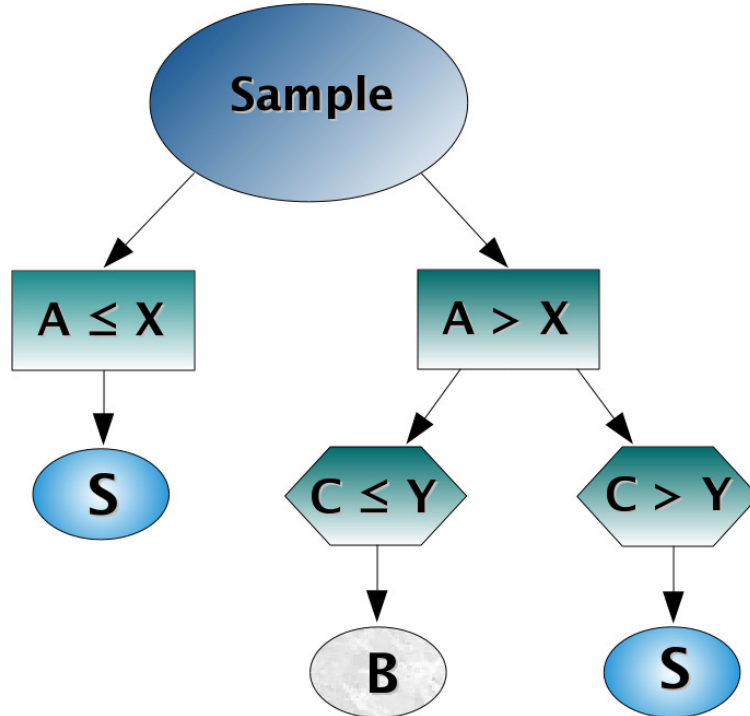


Figure B.1: A pictorial representation of a single decision tree, where A and C are variables values, X and Y are selection thresholds. The node is designated as S for signal and B for background. The S and B circles are the final nodes, or leaves, in the tree.

1993 The tree itself is formed using an optimization criterion to determine which variable  
 1994 to use for each selection (or node split) and what threshold to take. The goal of such a

1995 criterion is to optimize the signal and background separation. For this study we use the  
1996 default optimization criterion, which is the Gini index. This is the purity times 1 minus  
1997 the purity,  $p(1-p)$ . The purity is the signal events divided by all of the events considered in  
1998 that node, so if a node would have only signal events, the purity would be 1, giving a Gini  
1999 index of 0. If there are only background events, the purity is 0, and the Gini index is again  
2000 0. The goal of the splitting is to obtain nodes that are background or signal dominated,  
2001 so nodes are optimized to obtain a Gini index of 0 (or close to 0). Unlike the cut-based  
2002 analysis in Section 9.2.1, systematic uncertainties cannot be considered when determining  
2003 each individual selection of a tree.

2004 The “boosted” portion of the name boosted decision tree refers to an algorithm which  
2005 reweights events based on whether or not they were mis-classified as signal and background in  
2006 the previous tree. These weights then affect how the performance is evaluated in the training  
2007 of the next tree. The boosting algorithm used in this study is called  $\epsilon$ -boost [77, 76]. This  
2008 particular algorithm increases the weights of incorrectly classified events by a factor of  $e^{2\epsilon}$ .  
2009 The  $\epsilon$  value may be set to different values, but here we use the default value of 0.01. In  
2010 the end, the various trees are all averaged to give a final boosted tree. The classifiers for  
2011 each tree, the functions which are averaged, are formed by minimizing what is called a  
2012 quadratic loss criterion. This is the average of the square of the difference between the true  
2013 and predicted classifications for all events.

### 2014 **B.1.1 Classifier Formation and Parameter Optimization**

2015 When forming a classifier, there are three different MC samples considered. These are formed  
2016 by taking the modulus of the event number and are called training, validation, and yield.

2017 The yield sample is only used for the final analysis evaluation to ensure an unbiased result.  
2018 The training sample is used to form various classifiers and the validation sample is used to  
2019 evaluate if some particular classifier is the one we desire. The one exception to this sample  
2020 division in this study is the multijets process. The statistics are quite low for this sample, so  
2021 it is divided in half to form a training and yield sample, again using the modulus of the event  
2022 number. Additionally, because of limitations in the statistical package, negatively weighted  
2023 events cannot be used during the training phase when the classifier is generated. There are  
2024 such events in most of the MC samples for the various top-quark processes. However, the  
2025 proportion of negatively weighted events is low (about 7% in the training sample for the  
2026 signal). Even if this did have some effect, it would simply result in a less than optimally  
2027 trained classifier, not a biased result, because the sample used for the result includes both  
2028 negative and positively weighted events.

2029 It is possible to train different combinations of channels: each channel separately, the  
2030 number of jet channels separately (but with both lepton charges allowed), and all four  
2031 channels combined. For this study we use two BDT's for the final result, each with a  
2032 different number of jets (2 or 3). When samples are split in this way, the classifiers can  
2033 take advantage of the different kinematics in each number of jets channel. However, the  
2034 MC statistics will be lower after splitting the sample, potentially causing the kinematics and  
2035 events to be unevenly distributed. A multivariate classifier can be particularly sensitive to  
2036 this, especially if a tight cut on the classifier is taken, as we do here. This is one reason why  
2037 we do not further divide this sample in additional kinematic regions and combine several  
2038 classifiers for the final result.

2039 There are several different classifier settings to choose from when forming a BDT. In this

study, we vary the number of decision trees the BDT uses and the minimum number of events in the leaves for each tree. We use the default settings for other parameters, including the type of boost ( $\epsilon$ -boost with  $\epsilon$  of 0.01), the per event loss (quadratic), and the optimization criterion (Gini index), discussed at the beginning of Section B.1. The number of variables considered is another parameter of the BDT and we consider several different combinations of variables.

Many different trees are generated using the training sample with a variety of classifier settings. We choose the trained BDT classifier and cut threshold for that classifier by using a criteria that includes systematic uncertainties, as we do in the main text in Section 9.2.1. In this case, we found a few classifiers that had consistent distributions in the training and validation samples and were continuous. We then determine which of these would give the best expected result, based on the significance calculated using validation sample information. Multijets are not considered during the significance calculation.

It is possible to overtrain a BDT during the generation of the classifier, which means it is too tuned to the particular MC sample's kinematics subtleties, like being trained on noise. Overtraining results in a BDT that is sub-optimal, which we would like to avoid, but doesn't invalidate the analysis. The  $\chi^2$  [74] and Kolmogorov-Smirnov (KS) [78] tests are used to check the training and validation sample agreements. Classifiers are chosen which have good agreement ( $> 5\%$ ). Additionally, because the validation sample is used to determine the BDT settings and threshold, it is also possible to be sensitive to this sample's particular distributions. We save a yield sample for the cross-section calculation to ensure that such a sensitivity won't impact the final result.

2062    **B.1.2 Cut-based Analysis Variables**

2063    Because this dissertation focuses on a cut-based analysis, it is interesting to consider what  
2064    would happen if we train BDTs using only the variables from the cut based analysis. For this,  
2065    we use all four variables considered in Section 9.3 for each number of jet channel, as well as  
2066    lepton charge for a total of five variables in each channel. The variables used for both channels  
2067    are: sum of the transverse momenta of all jets, lepton, and  $E_T^{\text{miss}}$ ; leading untagged jet  $\eta$ ;  
2068    top quark mass reconstructed using the b-tagged jet, lepton, and reconstructed neutrino;  
2069    and lepton charge. Additionally,  $\Delta\eta$  between the b-tagged jet and leading untagged jet is  
2070    used for the 2 jet selection and the invariant mass of all jets is used for the 3 jet selection.

2071       For the 2 jet selection, the classifier parameters and cut threshold are: 250 trees, 1500  
2072    events minimum per leaf, and 0.74 cut threshold. For the 3 jet selection, these are: 150 trees,  
2073    1250 events minimum per leaf, and 0.41 cut threshold. The BDT classifier distribution before  
2074    and after the selection for each channel is shown in Figure B.2, normalized to the observed  
2075    t-channel cross-section. The variable distributions after this cut threshold for each channel  
2076    are given in Figures B.3 and B.4 for the 2 and 3 jet selections respectively, also normalized to  
2077    the observed t-channel cross-section. Notice that after the selections, the kinematic regions  
2078    chosen for the distributions look similar to those in Figures 9.4 and 9.5, particularly the  
2079    reconstructed top mass, leading untagged jet  $\eta$  and the invariant mass of all of the jets.  
2080       Overall the agreement is fairly good between data and MC in these plots, keeping in mind  
2081    the lower MC statistics from splitting the MC into thirds and also the somewhat large  
2082    systematic uncertainties.

2083       The yields after the selections on the BDT thresholds are given in Table B.1. Overall the  
2084    yields a little lower than the cut-based analysis (see Section 9.3). The signal to background

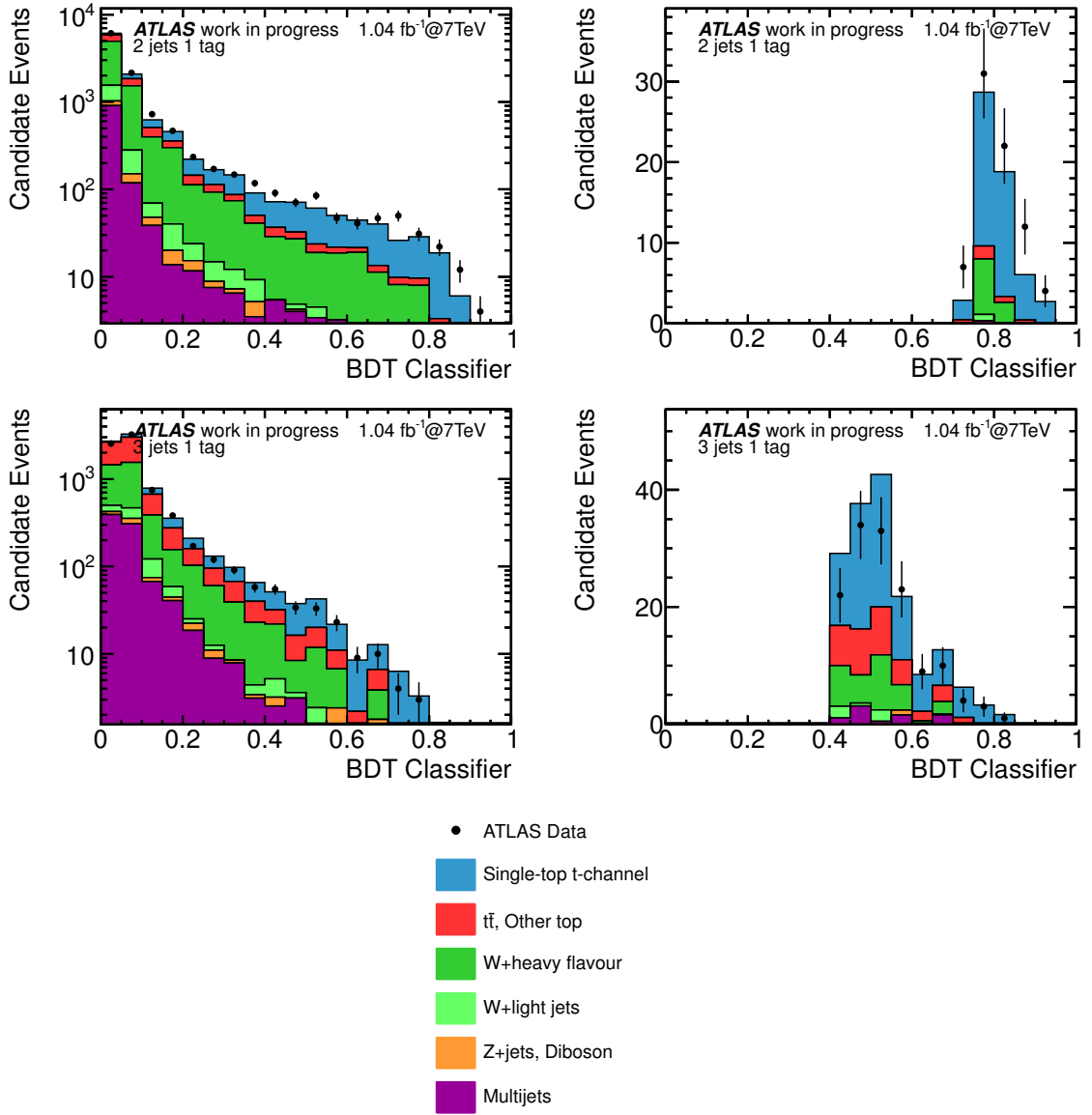


Figure B.2: BDT classifier distributions for the 2 jet (top) and 3 jet (bottom) selections, formed using cut-based analysis variables. The left column is before the selection on the BDT classifier in a log scale, and the right column is after. The  $t$ -channel single-top contribution is normalized to the observed cross-section determined using all four channels. Other top refers to the  $s$ -channel and  $Wt$  single-top contributions.

2085 ratios are much higher in the 2 jet channel but a little lower or the same in the 3 jet channel.  
 2086 This indicates that the BDT for the 2 jet selection in particular has better separating power  
 between signal and background than the cut-based analysis cuts.

	BDT 5 Variables 2 Jets		BDT 5 Variables 3 Jets	
	Lepton +	Lepton -	Lepton +	Lepton -
$t$ -channel	27.7	7.6	56.9	12.8
$t\bar{t}$ , Other top	2.2	1.0	25.9	6.9
$W$ +light jets	0.8	< 0.1	4.4	< 0.1
$W$ +heavy flavour jets	7.5	2.0	23.6	4.5
$Z$ +jets, Diboson	< 0.1	< 0.1	1.1	< 0.1
Multijets	0.3	< 0.1	7.8	< 0.1
TOTAL Exp	38.5	10.7	119.7	24.2
S/B	2.6	2.4	0.9	1.1
DATA	60	16	115	24

Table B.1: Event yield for the two-jets and three-jets tag positive and negative lepton-charge channels after the selection on the BDT formed using the cut-based analysis variables. The multijets and  $W$ +jets backgrounds are normalized to the data; all other samples are normalized to theory cross-sections. The  $t$ -channel single-top contribution is normalized to the observed cross-section determined using all four channels. Other top refers to the  $s$ -channel and  $Wt$  single-top contributions.

2087  
 2088 The expected cross-section was also calculated for the BDT distributions. The 2 and  
 2089 3 jet channels were split into negative and positive lepton charge channels, after selecting  
 2090 the desired region of the BDT classifier, and the combination was calculated using all four  
 2091 channels. The expected cross-section calculation used the systematic shifts and statistical  
 2092 methods from the cut-based analysis (Section 10.1) except in the cases of the largest system-  
 2093 atic uncertainties, which were estimated using the shifts in the yields of the BDT classifier  
 2094 distributions after the selection on it. These systematic uncertainties that were re-estimated  
 2095 are the statistical, b-tagging scale factor, mis-tagging scale factor, jet energy scale, generator,  
 2096 parton shower, and ISR/FSR uncertainties. The MC statistical uncertainty is not changed  
 2097 here, but we might expect it to be about 1.7 times as large as in the cut-based analysis, if

2098 the proportion of events from the different processes is relatively unchanged. This is because  
2099 the MC event weights increase by a factor of 3 and there are 1/3 as many events, giving  
2100 a factor of  $\sqrt{3}$  multiplied with the square root of the sum of the squares of the weights of  
2101 the events (the MC statistical uncertainty). The uncertainties which are re-estimated and  
2102 the total uncertainties using both re-estimated and cut-based analysis values are given in  
2103 Table B.2.

2104 The uncertainties are generally comparable with the cut-based analysis except for the  
2105 ISR/FSR uncertainty, which is much larger. This may be due to the ISR/FSR uncertainty  
2106 not being considered during the optimization of the classifier with the validation sample,  
2107 leading to the selection of events that happen to have a larger uncertainty. This is something  
2108 that could be added to the classifier optimization in a future study. Additionally, the jet  
2109 energy scale uncertainty is higher and the b-tagging scale factor uncertainty is lower versus  
2110 the cut-based analysis, reflecting some differences in the selected events in the BDT versus the  
2111 cut-based analysis. If we use the cut-based ISR/FSR uncertainty value, assuming the BDT  
2112 analysis could be improved to reduce this uncertainty, the expected cross-section uncertainty  
2113 would be  $\sigma_t = 65^{+21}_{-19}$  pb, compared to  $\sigma_t = 65^{+22}_{-20}$  pb from the cut-based analysis in  
2114 Section 10.2.1.3. The expected cross-section uncertainty with the re-estimated ISR/FSR is  
2115  $\sigma_t = 65^{+34}_{-26}$  pb. The observed cross-section value is  $\sigma_t = 82.9^{+36}_{-28}$  pb, which is consistent  
2116 with the cut-based analysis result within uncertainties.

### 2117 **B.1.3 Additional Variables**

2118 Of course, there is no reason to choose only the variables used for the cut based analysis when  
2119 generating the BDTs. Starting from these variables, we considered many additional variable

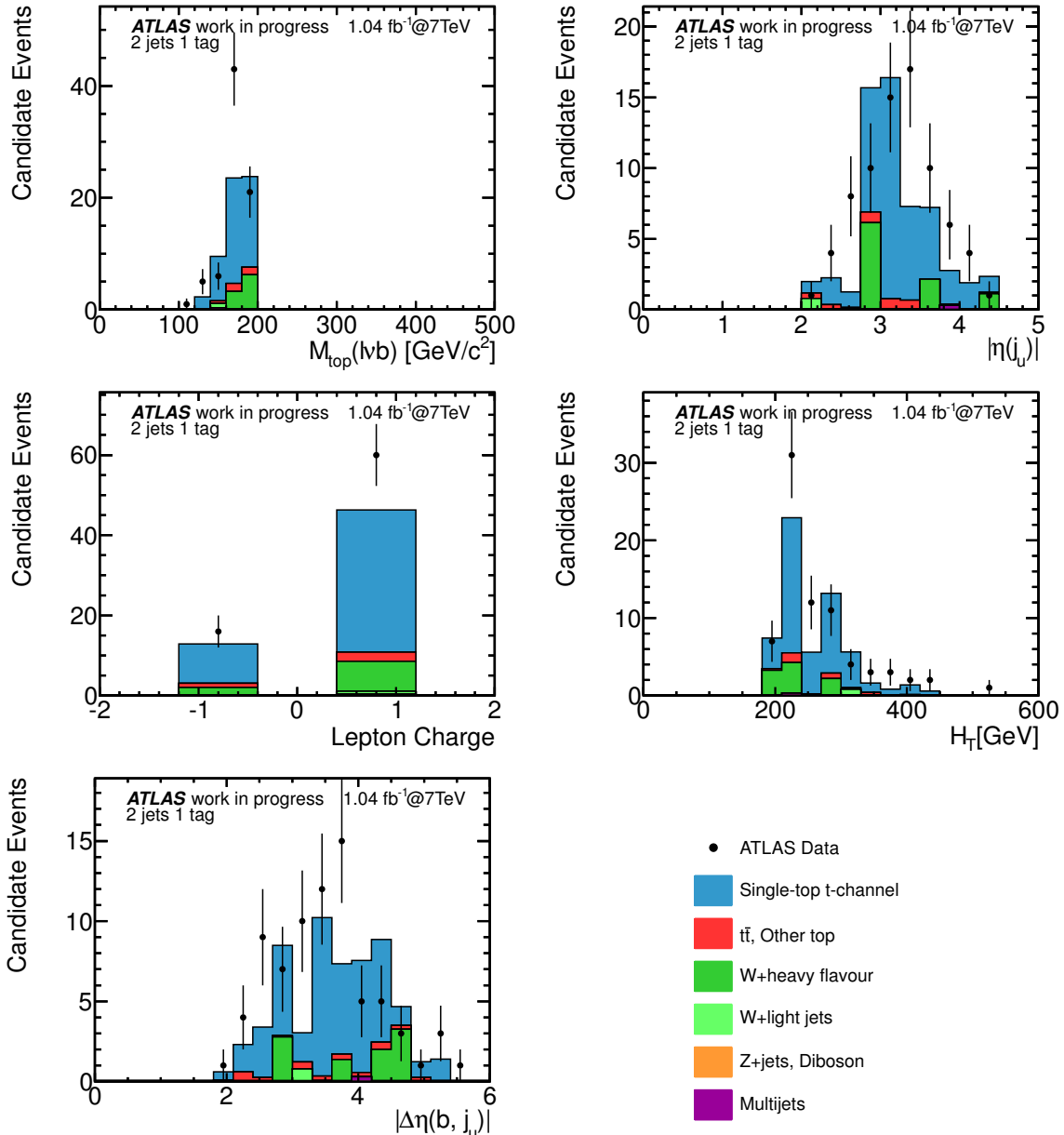


Figure B.3: Discriminating variables for the 2 jets selection after a selection on the BDT classifier formed using cut-based analysis variables. The last bin contains the sum of the events in that bin or higher. The  $t$ -channel single-top contribution is normalized to the observed cross-section determined using all four channels. Other top refers to the  $s$ -channel and  $Wt$  single-top contributions.

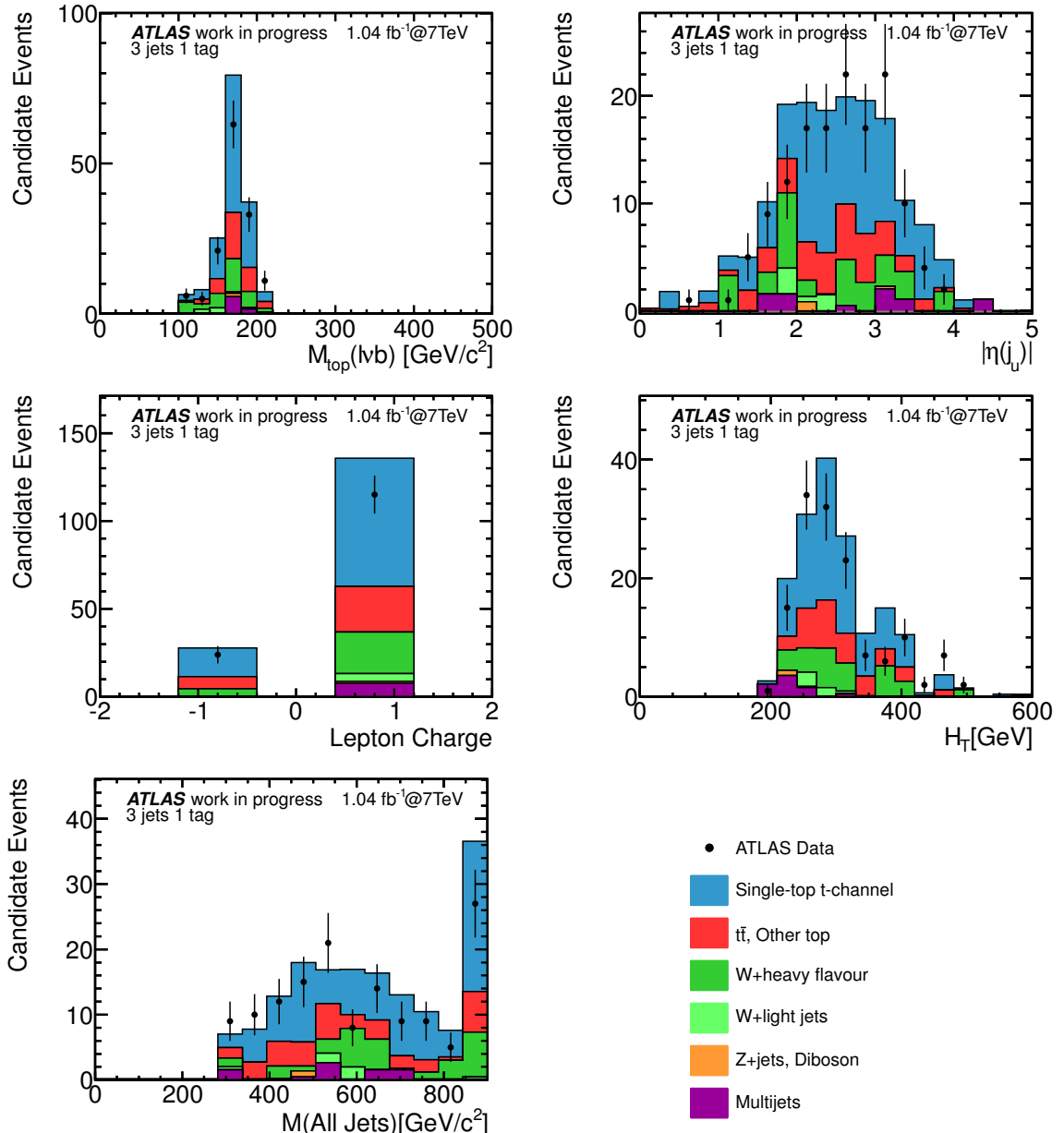


Figure B.4: Discriminating variables for the 3 jets selection after a selection on the BDT classifier formed using cut-based analysis variables. The last bin contains the sum of the events in that bin or higher. The  $t$ -channel single-top contribution is normalized to the observed cross-section determined using all four channels. Other top refers to the  $s$ -channel and  $Wt$  single-top contributions.

Source	$\Delta\sigma/\sigma (\%)$
Expected statistics	+13/-13
$b$ tagging scale factor	+6/-6
Mistag scale factor	+1/-1
Jet energy scale	+7/-8
Generator	+7/-7
Shower	+14/-14
ISR/FSR	+40/-29
Total Systematics	+50/-38
Total	+52/-40

Table B.2: Systematic uncertainties for the expected  $t$ -channel cross-section measurement for the BDT formed using cut-based analysis variables, where the final line includes all systematic uncertainties and the statistical uncertainty of the data. Uncertainties that were re-estimated versus the cut-based analysis (Section 10.2.1) are listed individually. Others are not listed but are included in the totals.

combinations, using variables that were considered for the cut-based analysis but not used (see Section 8). After many options were considered, BDT classifiers were chosen for the 2 jet and 3 jet selections which happen to use the same variables. These BDT classifiers were chosen to have a large significance in the validation sample, a relatively low number of variables, and good agreement between the training and validation BDT distributions.

The best classifiers had 10 variables, including the lepton charge variable. In addition to the 6 variables considered in this analysis (listed in Section B.1.2), the following were used for both jet number selection channels:  $\eta$  of the lepton; cosine of the angle between the lepton and the untagged jet, both in the rest frame of the top quark reconstructed using the leading b-tagged jet; W transverse mass; and  $\Delta\eta$  between the b-tagged jet and the lepton. Note that the  $\Delta\eta$  between the b-tagged jet and leading untagged jet and the invariant mass of all jets are now used for both the 2 and 3 jet selections, unlike in Section B.1.2. The distributions of the additional variables with the preselection applied for the full MC set are shown in Figure B.5 for the 2 jet selection and Figure B.6 for the 3 jet selection, showing

<sup>2134</sup> good agreement between the data and the MC.

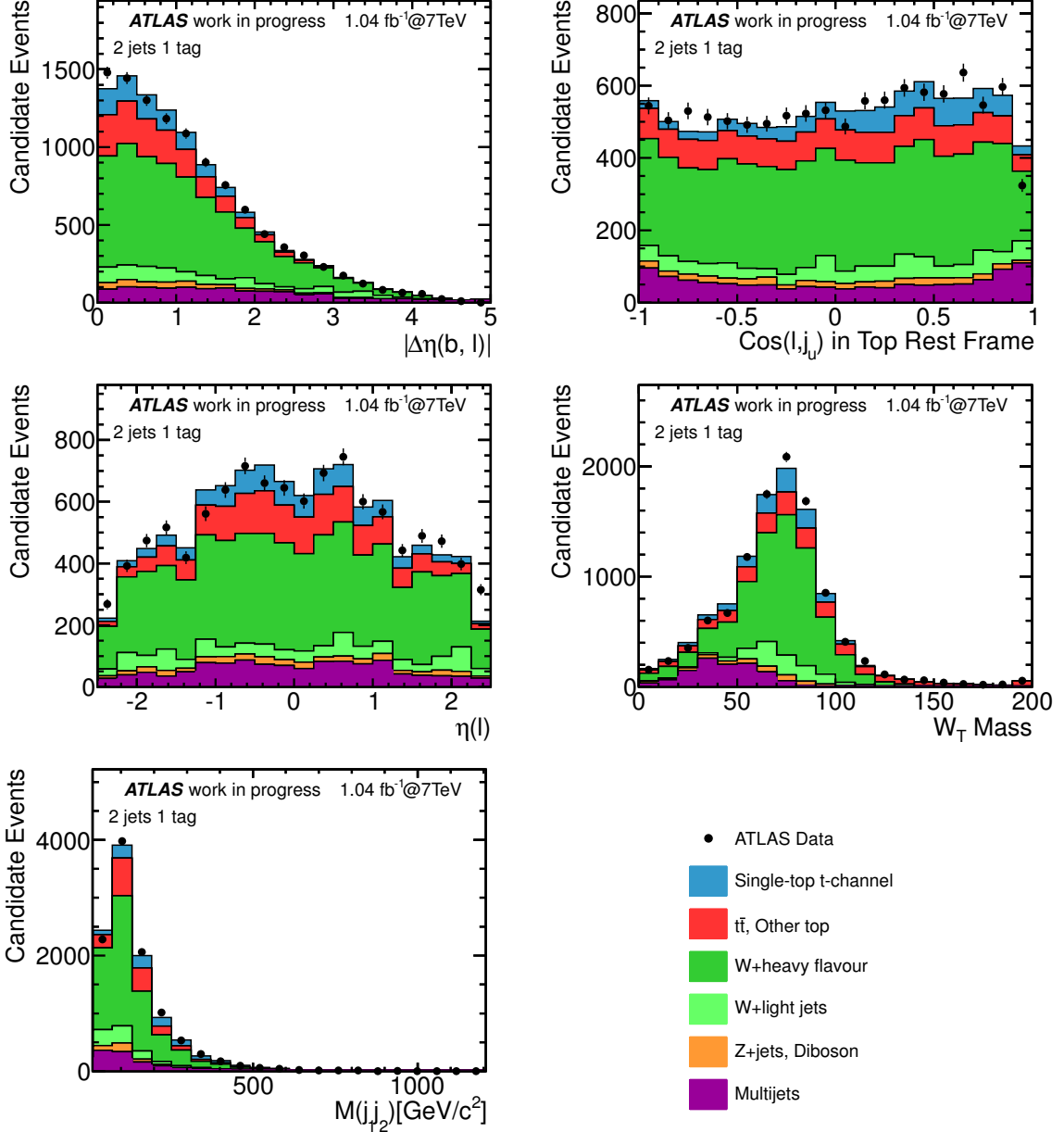


Figure B.5: Discriminating variables for the 2 jets selection before any BDT classifier selection. The last bin contains the sum of the events in that bin or higher. Other top refers to the  $s$ -channel and  $Wt$  single-top contributions.

<sup>2135</sup> For the 2 jet selection, the classifier parameters and cut threshold are: 150 trees, 2500 events minimum per leaf, and 0.64 cut threshold. For the 3 jet selection, these are: 150 trees, 1500 events minimum per leaf, and 0.42 cut threshold. The BDT classifier distributions

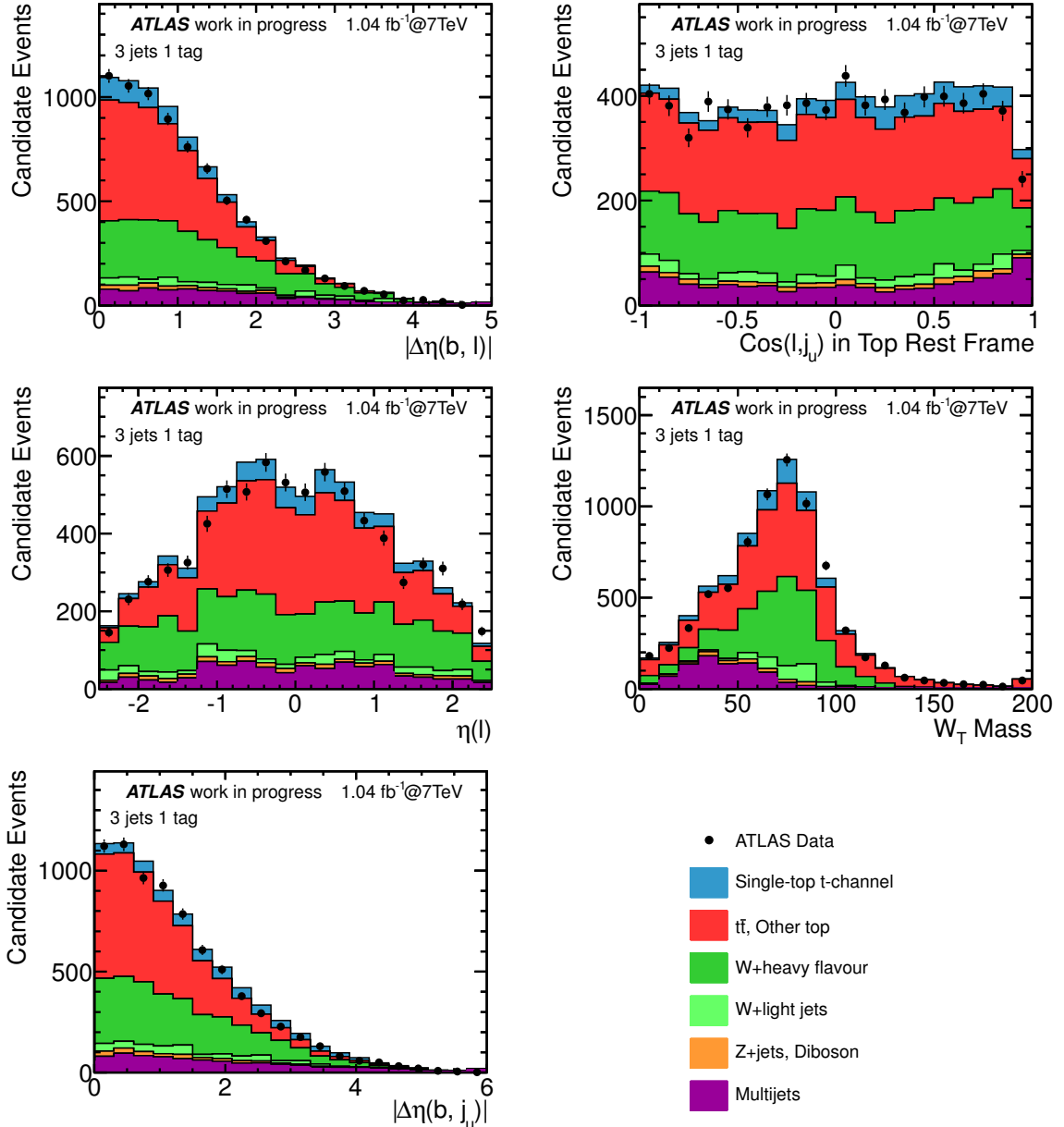


Figure B.6: Discriminating variables for the 3 jets selection before any BDT classifier selection. The last bin contains the sum of the events in that bin or higher. Other top refers to the  $s$ -channel and  $Wt$  single-top contributions.

before and after the selection for each channel are shown in Figure B.7, normalized to the  
 observed t-channel cross-section. The variable distributions after this cut threshold for each  
 channel are given in Figures B.8 and B.9 for the 2 jet selection, and Figures B.10 and B.11 for  
 the 3 jet selection, with all normalized to the observed t-channel cross-section. Again, notice  
 that after the selections, the kinematic regions selected in the distributions look similar to  
 those in Figures 9.4 and Figures 9.5, particularly the reconstructed top mass, invariant mass  
 and leading untagged jet  $\eta$  distributions.

The yields after the selections on the BDT thresholds are given in Table B.3. The signal  
 to background ratios here are about the same as those from Section B.1.2 for the 3 jet bin  
 but are much improved for the 2 jet selection. This indicates that the extra variables have  
 particularly helped the signal versus background discrimination in the 2 jet bin.

	BDT 10 Variables 2 Jets		BDT 10 Variables 3 Jets	
	Lepton +	Lepton -	Lepton +	Lepton -
<i>t</i> -channel	45.9	19.7	46.0	16.7
$t\bar{t}$ , Other top	2.2	2.1	16.6	7.5
$W$ +light jets	0.8	< 0.1	2.4	< 0.1
$W$ +heavy flavour jets	9.7	6.5	25.4	8.3
$Z$ +jets, Diboson	< 0.1	< 0.1	0.3	0.6
Multijets	1.9	1.6	3.6	< 0.1
TOTAL Exp	60.5	29.9	94.3	33.1
S/B	3.1	1.9	0.9	1.0
DATA	94	33	82	38

Table B.3: Event yield for the two-jets and three-jets tag positive and negative lepton-charge  
 channels after the selection on the BDT formed using 10 analysis variables. The multijets and  
 $W$ +jets backgrounds are normalized to the data; all other samples are normalized to  
 theory cross-sections. The *t*-channel single-top contribution is normalized to the observed  
 cross-section determined using all four channels. Other top refers to the *s*-channel and  $Wt$   
 single-top contributions.

2148

The additional variables are used to try to improve the uncertainty on the cross-section  
 measurement versus the BDT formed with cut-based variables only. The extra informa-

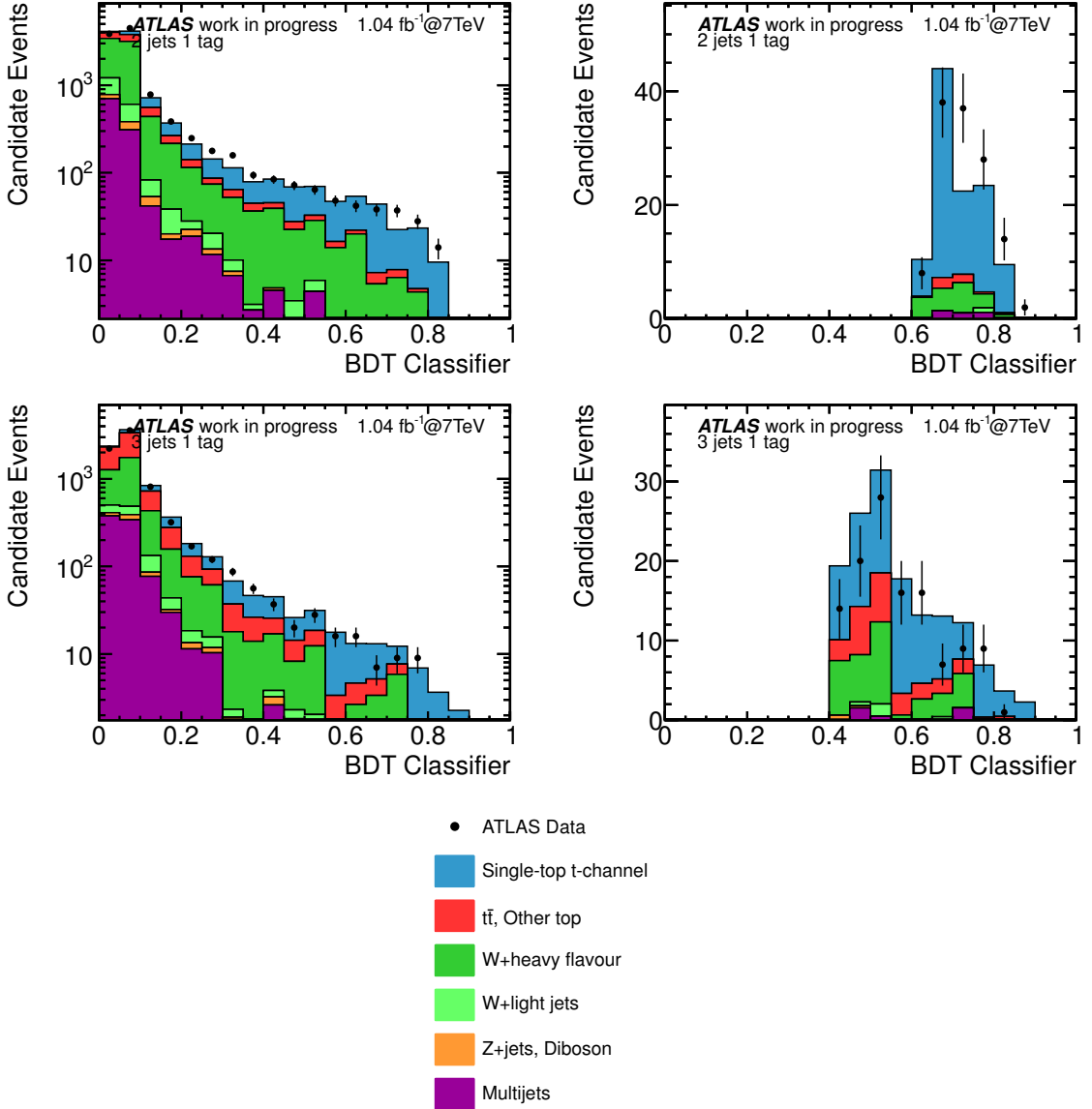


Figure B.7: BDT classifier distributions for the 2 jet selection on the top line and the 3 jet selection on the next line, for the BDT formed using 10 analysis variables. The left figures are before the selection on the BDT classifier, the right figures are after. Note that the BDT distributions before selections are in a log scale. The  $t$ -channel single-top contribution is normalized to the observed cross-section determined using all four channels. Other top refers to the  $s$ -channel and  $Wt$  single-top contributions.

tion should improve the signal and background separation, and may also help to improve the selection of low uncertainty kinematic regions. As in Section B.1.2, the 2 and 3 jet channels were split into negative and positive lepton charge channels, after selecting the desired region of the BDT classifier, and the combination was calculated using all four channels. The expected cross-section uncertainties for the combination is given in Table B.4. Also, as in Section B.1.2, only the statistical, b-tagging scale factor, mis-tagging scale factor, jet energy scale, generator, parton shower, and ISR/FSR uncertainties are re-estimated. Again, the ISR/FSR uncertainty is very high here, and including this uncertainty in the BDT optimization might improve the result in future studies. The other uncertainties are generally similar to the cut-based result, although we again see that the b-tagging scale factor uncertainty is lower than it was in the cut-based analysis from Section 10.2.1. The overall uncertainty is lower than the BDT cross-section expectation using only cut-based analysis variables, indicating the usefulness of the additional variables. The expected cross-section is  $\sigma_t = 65^{+30}_{-21}$  pb, while combined result from the BDTs using only cut-based variables had an expected cross-section of  $\sigma_t = 65^{+34}_{-26}$  pb. The observed cross-section value is  $\sigma_t = 83.8^{+34}_{-25}$  pb, which has a lower uncertainty than, and is consistent with, the value found from the BDTs using only cut-based analysis variables. In particular the central value is very similar. This cross-section is also consistent with the cut-based analysis value.

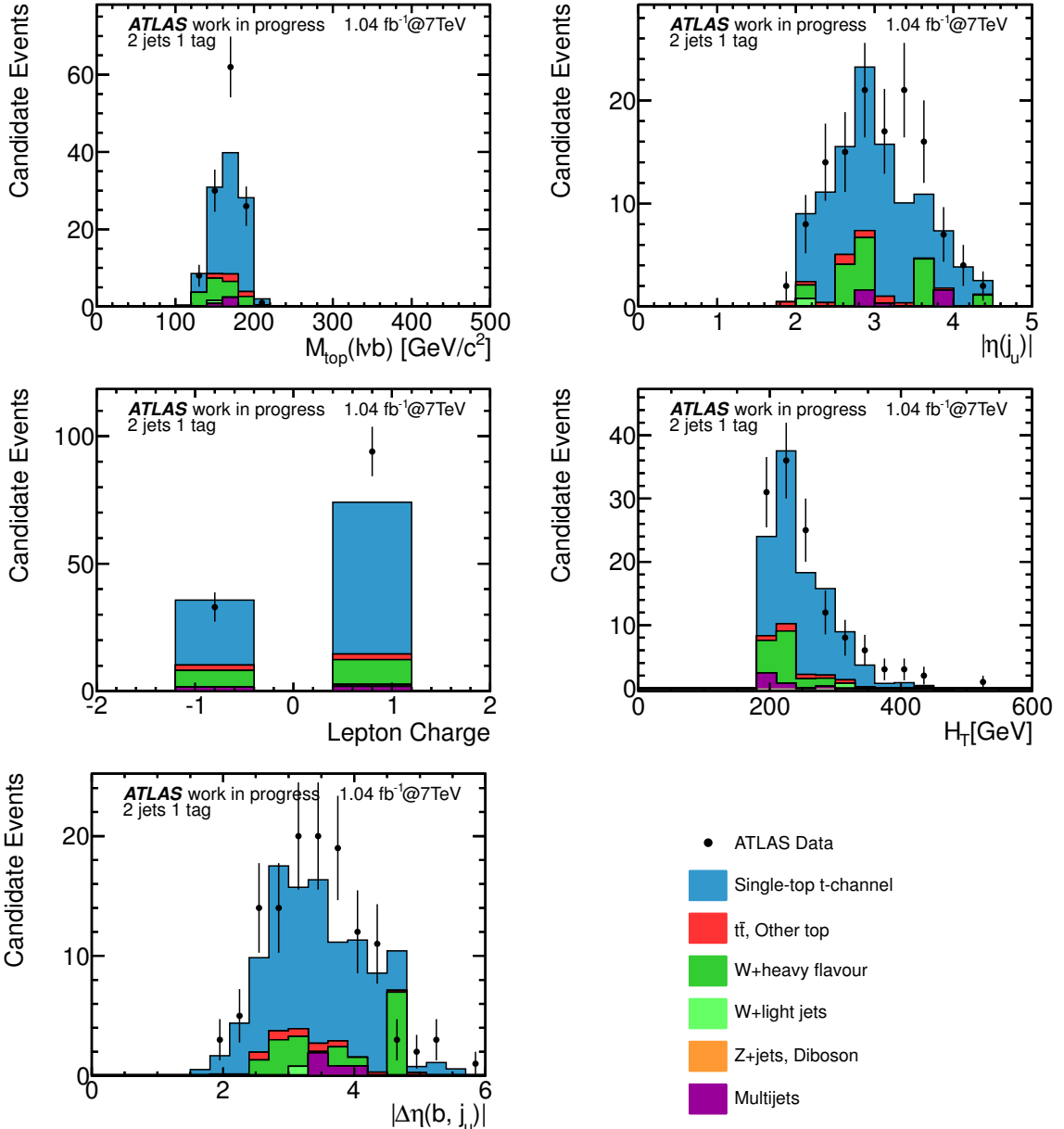


Figure B.8: Discriminating variables for the 2 jets selection. The figures are after the selection on the BDT classifier formed using 10 analysis variables. The last bin contains the sum of the events in that bin or higher. The  $t$ -channel single-top contribution is normalized to the observed cross-section determined using all four channels. Other top refers to the  $s$ -channel and  $Wt$  single-top contributions.

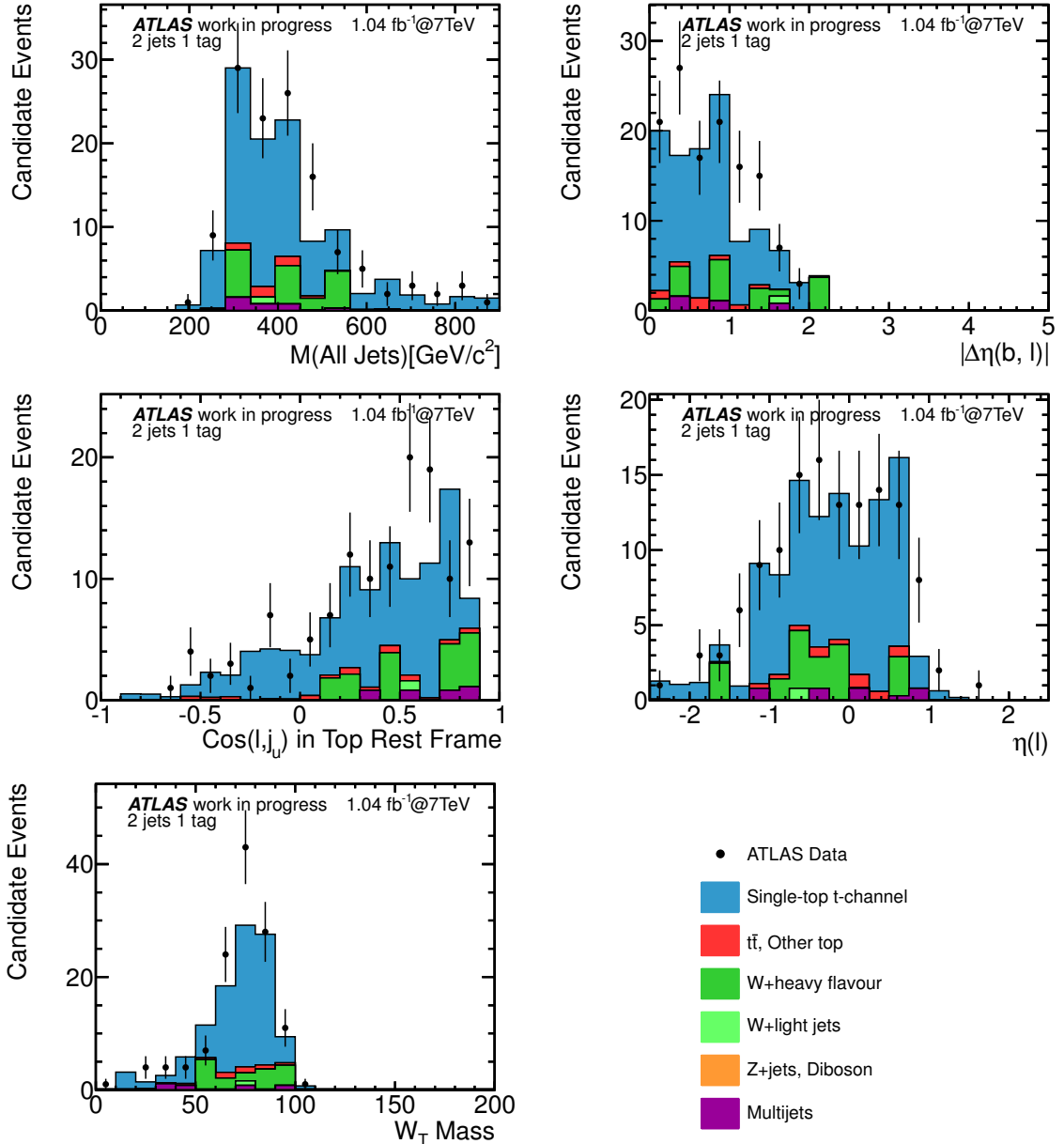


Figure B.9: Discriminating variables for the 2 jets selection. The figures are after the selection on the BDT classifier formed using 10 analysis variables. The last bin contains the sum of the events in that bin or higher. The  $t$ -channel single-top contribution is normalized to the observed cross-section determined using all four channels. Other top refers to the  $s$ -channel and  $Wt$  single-top contributions.

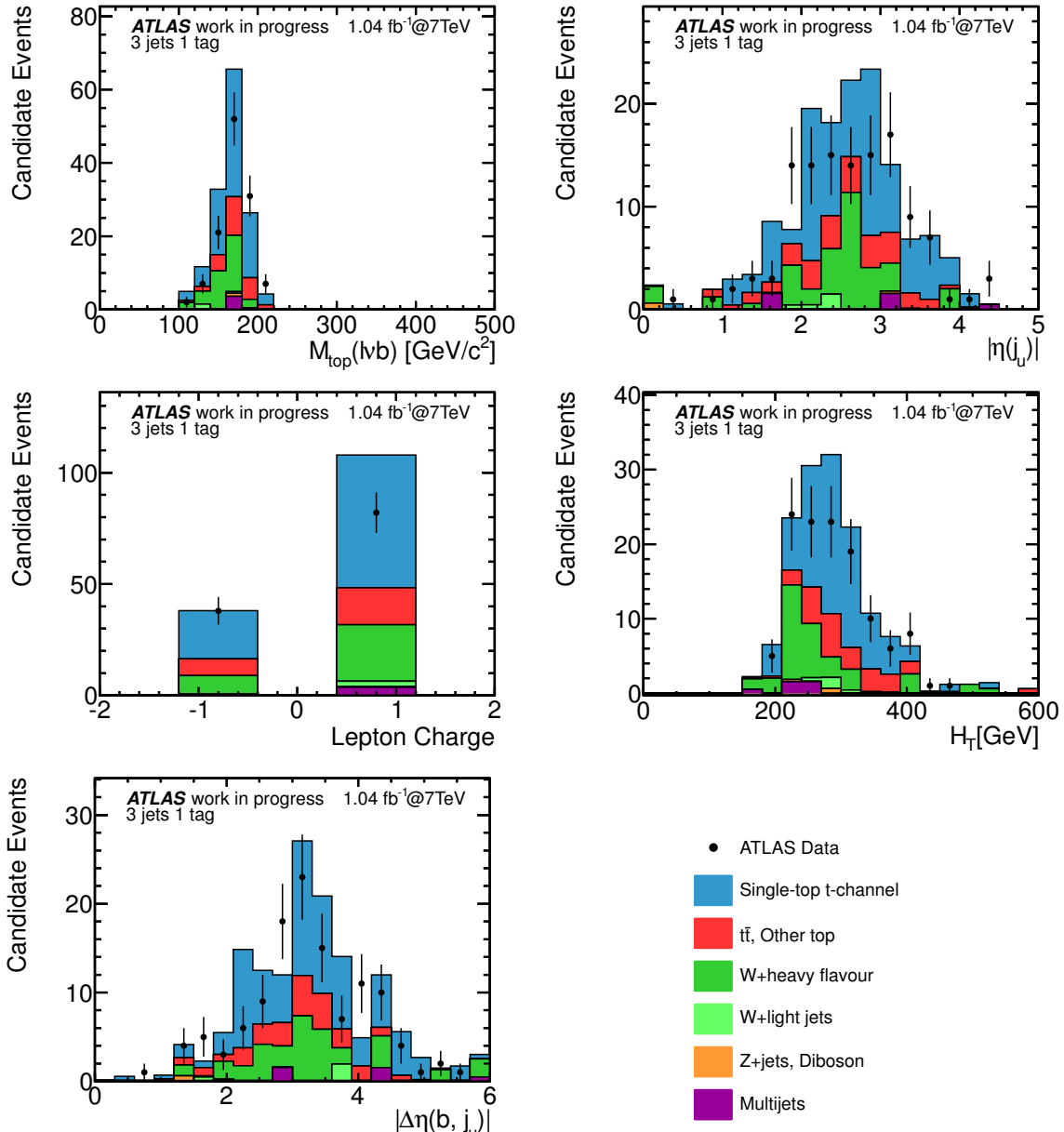


Figure B.10: Discriminating variables for the 3 jets selection. The figures are after the selection on the BDT classifier formed using 10 analysis variables. The last bin contains the sum of the events in that bin or higher. The  $t$ -channel single-top contribution is normalized to the observed cross-section determined using all four channels. Other top refers to the  $s$ -channel and  $Wt$  single-top contributions.

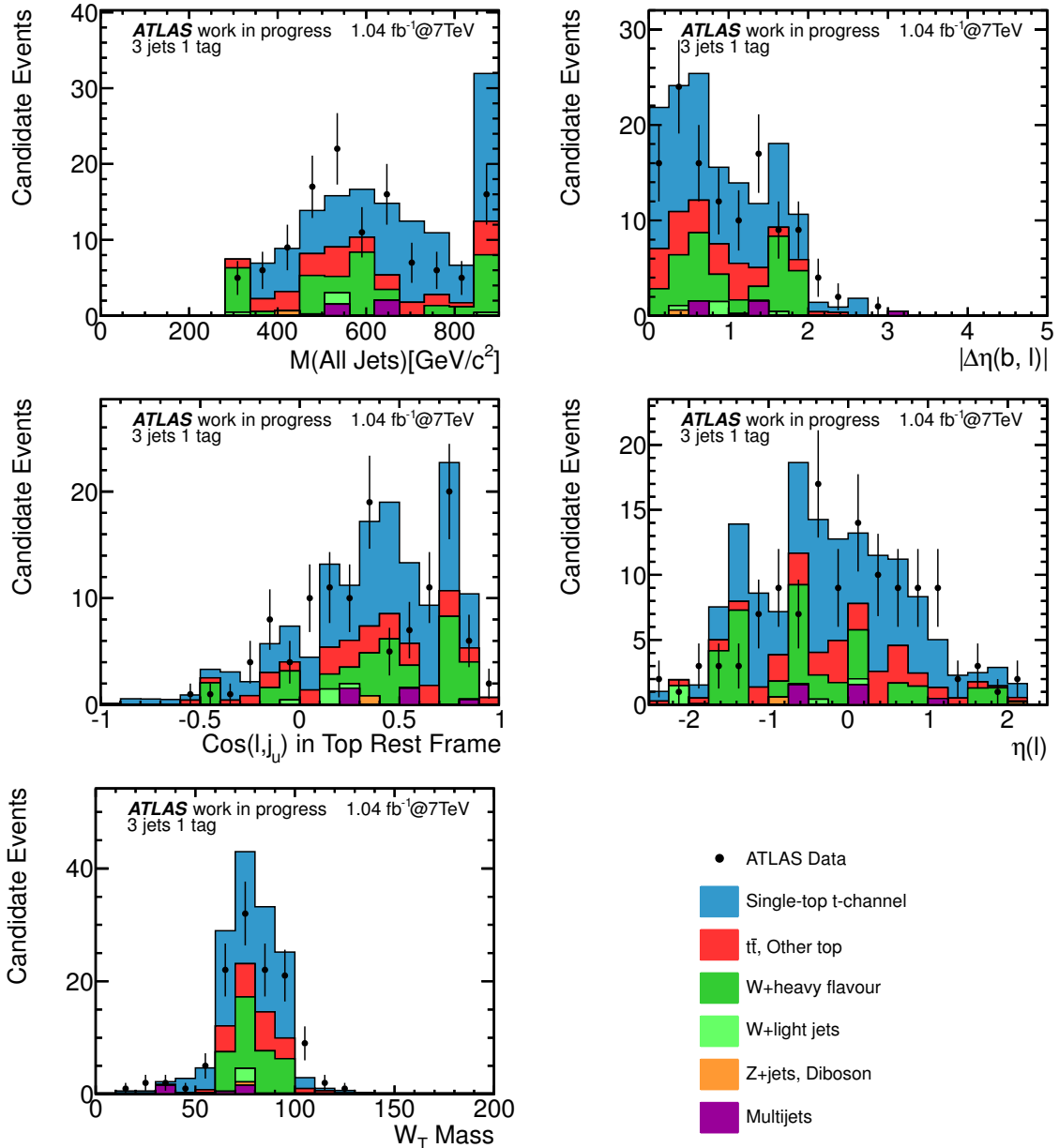


Figure B.11: Discriminating variables for the 3 jets selection. The figures are after the selection on the BDT classifier formed using 10 analysis variables. The last bin contains the sum of the events in that bin or higher. The  $t$ -channel single-top contribution is normalized to the observed cross-section determined using all four channels. Other top refers to the  $s$ -channel and  $Wt$  single-top contributions.

Source	$\Delta\sigma/\sigma (\%)$
Expected statistics	+11/-11
<i>b</i> tagging scale factor	+5/-5
Mistag scale factor	+2/-2
Jet energy scale	+4/-4
Generator	+8/-8
Shower	+11/-10
ISR/FSR	+34/-24
Total Systematics	+45/-30
Total	+46/-32

Table B.4: Systematic uncertainties for the expected  $t$ -channel cross-section measurement determined using the BDT created with 10 analysis variables, where the final line includes all systematic uncertainties and the statistical uncertainty of the data. Uncertainties that were re-estimated versus the cut-based analysis (Section 10.2.1) are listed individually. Others are not listed but are included in the totals.

<sub>2169</sub> **Appendix C**

<sub>2170</sub> **Alternative Analysis Channels**

<sub>2171</sub> The main analysis in this document made use of the 2 and 3 jet channels, split into positive or  
<sub>2172</sub> negative lepton charge (see Section 9.1). However, there are other possibilities. For instance,  
<sub>2173</sub> the four jet bin, although the “natural” bin for  $t\bar{t}$  production, could still be a useful channel if  
<sub>2174</sub> the  $t\bar{t}$  can be successfully removed. Similarly the 3 jet bin, where 2 jets are b-tagged (unlike  
<sub>2175</sub> 1 b-tagged jet in the main analysis) is also dominated by  $t\bar{t}$  production. If  $t\bar{t}$  can be removed  
<sub>2176</sub> from this bin, we may be able to see our single-top signal. The event yields for these two  
<sub>2177</sub> bins (split into lepton charge) after all preselection cuts including either 1 or 2 b-tagged jets,  
<sub>2178</sub> are shown in Table C.1. The signal divided by background (S/B) value is also shown. No  
<sub>2179</sub> W+jets normalization scale factors or multijet estimates are included in any of the tables in  
<sub>2180</sub> this discussion. However, as the yields are dominated by top processes, neither exclusion is  
<sub>2181</sub> expected to have a large effect on the conclusions of this study.

<sub>2182</sub> The first two selections in the main analysis (Section 9.3) make use of differences between  
<sub>2183</sub> the t-channel single-top production and its backgrounds, and we apply both of these selec-  
<sub>2184</sub> tions here with a slight variation on the reconstructed top mass selection. The reasoning

	4 Jets, 1 b-tagged		3 Jets, 2 b-tagged	
	Lepton +	Lepton -	Lepton +	Lepton -
$t$ -channel	200	100	72	46
$t\bar{t}$ , Other top	1800	1800	560	550
$W$ +light jets	99	43	0.2	0.2
$W$ +heavy flavour jets	400	310	73	45
$Z$ +jets, Diboson	50	43	4.9	2.7
S/B	0.08	0.05	0.11	0.08

Table C.1: Event yields for the four jets, one b-tag and three jets, two b-tags with positive and negative lepton-charge channels after the preselection. The multijets are neglected and  $W$ +jets backgrounds are normalized to the MC expectation, all other samples are also normalized to theory cross-sections.

is the same as before. The t-channel single-top production often has an energetic forward non-b jet, whereas  $t\bar{t}$  tends to have more central jets. Also, the signal only has one top quark whereas  $t\bar{t}$  has two. Due to reconstruction difficulties, the b associated with the top decaying to leptons is not always correctly assigned when determining the reconstructed top mass for  $t\bar{t}$  production, so a selection requiring a top mass near the expected value is useful. Similarly, requiring the highest  $p_T$  untagged jet to be forward is also helpful, just as in the main analysis. The yields after requiring  $|\eta(j_u)| > 2.0$  and then after also requiring  $M_{top}(l\nu b) < 190$  GeV are shown in Tables C.2 and C.3 respectively. We use only the upper top mass selection from the main analysis here because of the low multijet expectation (which is ignored for this discussion) in these bins.

Finally, we can also make use of the invariant mass of the jets. In the main analysis (Section 9.3), the 3 jet bin had a large  $t\bar{t}$  component, and we used a selection involving the invariant mass of the jets to remove  $t\bar{t}$  events. For the 4 jet bin, we propose requiring the invariant mass of all jets except the best jet to be greater than 450 GeV. The best jet is the jet which, plus the lepton and  $E_T^{\text{miss}}$ , best produces the expected standard model top mass.

	4 Jets, 1 b-tagged		3 Jets, 2 b-tagged	
	Lepton +	Lepton -	Lepton +	Lepton -
<i>t</i> -channel	74	33	38	21
$t\bar{t}$ , Other top	240	230	82	81
$W$ +light jets	24	5.4	0.2	<0.1
$W$ +heavy flavour jets	65	56	14	6.3
$Z$ +jets, Diboson	7.1	7.6	0.5	0.5
S/B	0.22	0.11	0.40	0.24

Table C.2: Event yields for the four jets, one b-tag and three jets, two b-tags with positive and negative lepton-charge channels after the preselection and  $|\eta(j_u)| > 2.0$ . The multijets are neglected and  $W$ +jets backgrounds are normalized to the MC expectation, all other samples are also normalized to theory cross-sections.

	4 Jets, 1 b-tagged		3 Jets, 2 b-tagged	
	Lepton +	Lepton -	Lepton +	Lepton -
<i>t</i> -channel	50	22	19	12
$t\bar{t}$ , Other top	120	120	23.0	23.0
$W$ +light jets	16	2.4	0.2	<0.1
$W$ +heavy flavour jets	32	27	6.6	3.2
$Z$ +jets, Diboson	3.9	3.6	0.4	<0.1
S/B	0.29	0.14	0.64	0.45

Table C.3: Event yields for the four jets, one b-tag and three jets, two b-tags with positive and negative lepton-charge channels after the preselection,  $|\eta(j_u)| > 2.0$ , and  $M_{top}(l\nu b) < 190$  GeV. The multijets are neglected and  $W$ +jets backgrounds are normalized to the MC expectation, all other samples are also normalized to theory cross-sections.

2200 Thus, we are looking at the invariant mass of what should be the other top quark in the case  
2201 of  $t\bar{t}$  production, and the invariant mass should be close to that value. Single-top t-channel  
2202 can have a very energetic jet separated from the top quark decay products, leading to a  
2203 potentially very high invariant mass. These two effects give some separation, and we remove  
2204 events where the invariant mass is lower. Similarly for the 3 jet, 2-btagged jet selection, we  
2205 can look at this same invariant mass of all jets minus the best jet greater than 250 GeV. This  
2206 should give us the invariant mass of most of the jets from the other top quark in the case  
2207 of  $t\bar{t}$  production and so we again remove events where this invariant mass is lower to reduce  
2208  $t\bar{t}$  contamination. Specifically we require  $M(\text{AllJetsMinusBestJet}) > 450$  GeV for the four  
2209 jet channel and  $M(\text{AllJetsMinusBestJet}) > 250$  GeV for the three jet channel.

2210 The yields after these two invariant mass selections are given in Table C.4. This table  
2211 shows that the  $t\bar{t}$  events are removed at a larger rate than the signal, improving the S/B value  
2212 from the previous tables. Most S/B values are over 0.5 and one is over 1.5. Of course, the  
2213 yields themselves are low, leading to larger statistical uncertainties. However, these tables  
2214 are normalized to the integrated luminosity used in the main analysis,  $1.04 \text{ fb}^{-1}$ . Future  
2215 analysis will use data sets of 5, 10, or more times this value, making these sorts of tight  
2216 selections more useful for those analyses.

	4 Jets, 1 b-tagged		3 Jets, 2 b-tagged	
	Lepton +	Lepton -	Lepton +	Lepton -
$t$ -channel	27	12	10	4.0
$t\bar{t}$ , Other top	29	31	4.5	4.3
$W$ +light jets	1.8	0.6	<0.1	<0.1
$W$ +heavy flavour jets	6.2	5.9	0.7	1.2
$Z$ +jets, Diboson	1.2	2.0	0.2	<0.1
S/B	0.71	0.30	1.89	0.74

Table C.4: Event yields for the four jets, one b-tag and three jets, two b-tags with positive and negative lepton-charge channels after the preselection,  $|\eta(j_u)| > 2.0$ ,  $M_{top}(l\nu b) < 190$  GeV, and either  $M(\text{AllJetsMinusBestJet}) > 450$  GeV for the four jet channel or  $M(\text{AllJetsMinusBestJet}) > 250$  GeV for the three jet channel. The multijets are neglected and  $W$ +jets backgrounds are normalized to the MC expectation, all other samples are also normalized to theory cross-sections.